ASTON UNIVERSITY

School of Engineering & Applied Science

Ph. D. Thesis

to obtain the title of

Doctor of Philosophy

Computational modelling of the fast pyrolysis of biomass in bubbling fluidised bed reactors

Author: KONSTANTINOS PAPADIKIS

May, 2009

Aston University

Computational modelling of the fast pyrolysis of biomass in bubbling fluidised bed reactors

Konstantinos Papadikis
Doctor of Philosophy

May 2009

Thesis Summary

The aim of the current thesis is to model the various fluid-particle interactions in an $150g/h$ bubbling fluidised bed reactor. Mass, momentum and heat transfer from the bubbling bed of the reactor to the discrete biomass particles are modelled and analysed. The Eulerian-Eulerian approach is used to model the bubbling behaviour of the sand, which is treated as a continuum. The biomass particle motion inside the reactor is computed by integrating the equations of motion using drag laws, dependent on the local volume fraction of each phase. Reaction kinetics are also incorporated in the computational code according to the literature, using a two-stage global model which takes into account the intra-particle secondary reactions due to the catalytic effect of char, resulting on secondary vapour cracking. The model associates the reaction kinetics mechanism with the discrete biomass particle injected in the fluidised bed. The properties of the particle change according to the reaction mechanism due to the phase transition phenomena.

The model results provide significant information about the fast pyrolysis of biomass in bubbling fluidised beds, since it is able to predict the complicated fluid-particle interactions with simultaneous evolution of pyrolysis vapours. The vapour residence time can be determined as well as the char entrainment efficiency of the reactor. The effect of biomass shrinkage during pyrolysis and char particle size and shape is considered as an application of the developed model in the design and optimisation of fluidised bed reactors. Also, the impact of different biomass particle sizes on bed-to-surface heat transfer coefficient is modelled in order to provide a better understanding of the optimum operating conditions of the studied fluidised bed reactor. Furthermore, the results showed that the model was correctly implemented since they were highly agreeable with theoretical expectations as well as they were comparable with data in the literature whenever comparison was possible. The model indicated the advantages and drawbacks of the reactor regarding momentum and heat transfer as well as biomass degradation rates and vapour residence time.

Keywords: CFD, Fluidised bed, Fast pyrolysis, Granular flow, Heat transfer, Momentum transfer, Particle modelling

Acknowledgements

I would like to take this opportunity to express my gratitude and sincere thanks to Prof. A. V. Bridgwater and Dr. S. Gu, my supervisors, for their guidance, encouragement, financial support and understanding as well as providing me with first class computational resources for the implementation of this project.

I would also like to thank my collaborators and good friends Spyros Kamnis and Nicola Zeoli for their comments and suggestions throughout the three years period of the Ph.D.

I would also like to extend my acknowledgement to Christina, my parents Nikos and Efthymia, as well as my sister Smaragda (a.k.a "kommati") for their interest and support through the years of my student life.

Last but not least, I am very much indebted to Engineering and Physical Sciences Research Council (EPSRC) and Aston University for the complete funding of my studies as a research student.

Contents

List of Figures

List of Tables

Nomenclature

Latin letters

Symbol	**Description**	**Unit**
A	Area	m^2
$A_{1...5}$	Pre-exponential factor	s^{-1}
Ar	Archimedes number	dimensionless
$\mathbf{b}$	Body force per unit mass	N/kg
Bi	Biot number	dimensionless
C_d	Drag coefficient	dimensionless
C_p	Specific heat capacity	J/kgK
d	Diameter	m
e	Internal energy per unit mass	J/kg
e_{ss}	Restitution coefficient	dimensionless
E	Volumetric source of energy due to phase interaction	J/m^3
$\mathbf{E}$	Electric field intensity	N/C
$E_{1...5}$	Activation energy	J/mol
f	Drag factor	dimensionless
F	Force	N
$\mathscr{F}_i^b$	Body source of momentum	N
$\mathscr{F}_i^s$	Surface source of momentum	N
g	Gravitational acceleration	m/s^2
$g_{0,ss}$	Radial distribution coefficient	dimensionless
h_{dist}	Height above distributor	m
h	Heat transfer coefficient	W/m^2K
$\bar{\bar{I}}$	Stress tensor identity matrix	dimensionless
I_{2D}	Second invariant of the deviatoric stress tensor	dimensionless

k	Thermal conductivity	W/mK
$k_{\Theta s}$	Diffusion coefficient for granular energy	kg/sm
K	Momentum exchange coefficient	dimensionless
$K_{1...5}$	Kinetic constants	s^{-1}
Kn	Knudsen number	dimensionless
L	Bed height	m
m	Mass	kg
M	Reacting mass	kg
$\mathbf{M}$	Force per unit volume due to interaction with other phases	N/m^3
Nu	Nusselt number	Dimensionless
p	Pressure	N/m^2
ΔP_{bed}	Bed pressure drop	N/m^2
ΔP_{fr}	Frictional pressure drop	N/m^2
Pr	Prandtl Number	dimensionless
q	Electric charge	C
$\mathbf{q}$	Source of energy per unit total area	J/m^2
Q	Source of energy per unit total area	J/m^2
r	Radial position	m
R	Universal gas constant	$J/molK$
$\mathrm{Re_{p,mf}}$	Particle Reynolds number at minimum fluidisation	dimensionless
$\mathrm{Re_s}$	Reynolds number of solid phase	dimensionless
$\mathrm{Re_d}$	Droplet or particle Reynolds number	dimensionless
S	Surface area	m^2
t	Time	s
T	Temperature	K
$\mathbf{T}$	Stress tensor	N/m^2
U_b	Bubble rise velocity	m/s
U_{br}	Single bubble rise velocity	m/s
U_{mf}	Minimum fluidising velocity	m/s

U_0	Superficial gas velocity	m/s
v	Velocity field	m/s
V	Volume	kg/m^3
w	Free settling velocity	m/s
$\mathscr{W}_i^b$	Body source of energy	J
$\mathscr{W}_i^s$	Surface source of energy	J

Greek letters

α	Deviation factor	dimensionless
α_{sh}	Shrinking factor	dimensionless
β	Saffman lift force factor	dimensionless
β_{sh}	Shrinking factor	dimensionless
γ_{sh}	Shrinking factor	dimensionless
γ_{Θ_s}	Collision dissipation of energy	kg/s^3m
Γ	Rate of production of mass per unit volume due to phase change	kg/m^3s
δ_{ij}	Kronecker delta	dimensionless
ε_i	Volume fraction	dimensionless
ζ	Arbitrary property per unit volume	m^{-3}
Θ_s	Granular temperature	m^2/s^2
λ	Second coefficient of viscosity	kg/ms
μ	Dynamic viscosity	kg/ms
ρ	Density	kg/m^3
τ	Particulate relaxation time	s
$\bar{\bar{\tau}}$	Tensor of viscous stresses	N/m^2
ϕ	Sphericity factor	dimensionless
ϕ_{gs}	Transfer rate of kinetic energy	kg/s^3m
ψ	Mass fraction	dimensionless
Ψ	Sphericity factor	dimensionless
ψ_b	Fraction of visible bubbles	dimensionless
ω	Angular velocity	rad/s

Subscripts

Symbol	Description
av	average
b	Bubble
bed	Bed of solids
br	Single bubble rise
$Basset$	Basset force
c	Continuous phase
C	Char
$C1$	Primary char
$C2$	Secondary char
col	Collision
Cou	Coulomb
d	Droplet
$dist$	Distributor plate
dm	Dispersed phase maximum packing
D	Drag
eff	Effective
f	Final
fr	Frictional
g	Gas
G	Gas
$G1$	Primary gas
$G2$	Secondary gas
i	General phase, coordinate index
j	General phase, coordinate index
k	Radial position index
kin	Kinetic
L	Lift
mf	Minimum fluidisation
p	Particle
pen	Penetration theory
s	Solids

sph	Sphere
$Saff$	Saffman force
t	Tube
$Ther$	Thermophoretic force
T	Tar
W	Wood
x	x cartesian coordinate
y	y cartesian coordinate
z	z cartesian coordinate
0	Initial

Superscripts

Symbol	**Description**
b	Body
s	Surface
T	Transpose
$*$	modified

Abbreviations

CFD	Computational Fluid Dynamics
DAEM	Distributed Activation Energy Model
DPM	Discrete Particle Model
FCC	Fluid Catalytic Cracker
GFM	Granular Flow Model
PEPT	Positron Emission Particle Tracking
TFM	Two-fluid model
TGA	Thermogravimetric Analyser
UDF	User Defined Function

Chapter 1

Introduction

The chapter includes a brief introduction on the history of the initial development of the fluidised bed technology, as well as a brief introduction of the fast pyrolysis process and its main characteristics. Also, it describes the the main subject of the thesis and explains the main elements of novelty to the reader. Finally, the progress of the research is described as well as the outline of the thesis pointing out the main elements of each chapter.

1.1 Historical notes

1.1.1 Fluidised bed technology

The initial development of fluidised bed technology on an industrial scale, occurred in the 1920s in Germany by Fritz Winkler and was directed at coal gasification to provide feedstocks for the chemical industry. The most important application of fluidised beds to date, which is the fluid bed catalytic cracking of crude oil, was developed during the Second World War in the United States [1].

During the 1939-1945 war, there was a great demand for high octane aviation spirit as a fuel for the piston driven aircraft of the time. In the process by which oil is cracked over a catalyst to produce it, carbon was deposited on the catalyst which soon becomes fouled and has to be regenerated. Thus, the conventional fixed bed reactors could not be developed to cope with the very high throughputs required [2].

It was well known that a high-velocity gas flow blows powdered solids up (or down) a pipe, but Warren K. Lewis and Edwin R. Gilliland of the Massachusetts

Institute of Technology, while working with Standard Oil Company of New Jersey, suggested that a low velocity gas flow through a powder might "lift" it enough to cause it to flow in a manner similar to a liquid. This was quickly found to be true, and the M. W. Kellogg Company constructed a large pilot plant in Standard's Baton Rouge refinery. The pilot plant began operation in May of 1940. Based on its success, the construction of the first commercial plant began in September in the tense months just before World War II. The first Model I Fluid Catalytic Cracker (FCC) was completed on May 1, 1942 and began operating on May 25 in Baton Rouge at the Standard Oil Company refinery. Called PCLA-1 (Powdered Catalyst Louisiana), it was the first commercial fine powder circulating fluid bed reactor [3].

Today many chemical reactors use fluidised beds. For example, the commercial synthesis of acrylonitrile, phthalic anhydride, aniline, maleic anhydride, and a portion of the polymerisation of ethylene (to polyethylene) and propylene (to polypropylene) are all done in fluid bed reactors. There are noncatalytic processes, such as ore roasting, coking, combustion of coal and other solid fuels, as well as purely physical processes such as drying and conveying of fine particle products like flour, rice, and cement, which use the principles developed for the fine-particle fluidised bed [3].

1.1.2 Fast pyrolysis

Pyrolysis can be defined as *"the thermal degradation of organic materials in absence of oxygen"*. The primary pyrolysis products of biomass particles are usually referred to as condensable (vapours) and noncondensable volatiles and char. The condensable volatiles (vapours) are also often classified as liquids, and the noncondensable volatiles as gases mainly CO, CO_2, H_2 and $C_1 - C_2$ hydrocarbons. The liquids are frequently subdivided into water and organics.

Slow pyrolysis has been used since ancient times for the production of charcoal, while the liquid by-product tar, was used for ship building since Roman times. Since the oil crisis in the mid 1970s, considerable effort has been directed toward development of processes for producing liquid fuels from ligno-cellulosic biomass. Fast pyrolysis of biomass is one of the most recent renewable energy processes to have been introduced and it offers high yields of liquid product (bio-oil) that can be readily stored and transported. This led to the development of several fast pyrolysis technologies.

Fast pyrolysis is a thermal decomposition process that occurs at moderate temperatures with a high heat transfer rate to the biomass particles and a short hot vapour residence time in the reaction zone [4]. According to Bridgwater [5] maximum liquid yields are obtained with high heating rates, at reaction temperatures around 500^oC and with short vapour residence times to minimise secondary reactions. Liquids for use as fuels can be produced with longer vapour residence times [up to $\approx 6s$] and over a wider temperature range although yields might be affected in two ways: secondary volatiles decomposition at temperatures above 500^oC and condensation reactions at gas/vapour product temperatures below 400^oC.

Fast pyrolysis is nowadays accepted as a process for producing high yields of liquids that can be used as direct substitutes for conventional fuels or as source of chemicals. These reasons have led to the extensive research on the modifications of fast pyrolysis technology, as well as the upgrading of the liquids and the adaptation of the applications to accept the various and unusual characteristics of the liquid product [6].

1.2 Thesis subject

The subject of the current thesis is to develop a numerical model that will be able to simulate the complex fluid-particle interactions, as well as phase transition phenomena of biomass pyrolysis in bubbling fluidised bed reactors. The model will take into account the gas-solid nature of the flow according to the multiphase flow governing equations, incorporating the simultaneous evolution of volatiles from the pyrolysis of discrete biomass particles.

Multiphase flows occur in all sorts of operations in chemical plants, such as combustion, gasification, pyrolysis, pneumatic transport of solid grains in industry etc. The understanding of the physical laws that govern such processes, as well as their incorporation into mathematical models can be extremely useful and valuable in the efficient design and optimisation of chemical plants.

The scope of the study is the numerical investigation of the characteristics of the bubble three-phase flow (i.e solid particles in bubbly flow) occurring in a fluidised bed, where the dense particulate phase (i.e sand) is treated as a continuum (*two-fluid* approach). The solid phase immersed in the bubbling mixture is the biomass particles that undergo pyrolysis and evolution of vapours occur.

The computational method developed is applied to an $150g/h$ bubbling fluidised bed reactor located at the Chemical Engineering department laboratory of Aston

University. The commercial finite volume code FLUENT 6.2 [7] is used as the basic simulation platform of the bed hydrodynamics, with an extended C-subroutine in the form of User Defined Function (UDF) to account for the heat, mass, and momentum transport phenomena that occur in a complex process such as fast pyrolysis. Specifically, the thesis is focused on the development of the computational code that extends FLUENT, as well as the numerical modelling and analysis of the following aspects.

- The operation of a lab-scale bubbling fluidised bed reactor, using sand particles as the bed material and is fluidised by Nitrogen. The reactor is heated by a furnace to maintain the sand temperature at approximately 500^oC.
- The injection of biomass particles inside the sand bed.
- The momentum transferred from the bubbling bed to the biomass particles and their motion inside the reactor.
- The rapid heating of biomass to the appropriate temperature for fast pyrolysis
- The incorporation of reaction kinetics of biomass and their association with the discrete particles.
- The evolution of vapours from the solid biomass particles and their interaction with the continuous phases (Eulerian sand, Nitrogen).
- The entrainment of char from the fluidising gases. Studies on the effect of particle size and sphericity.
- The impact of biomass shrinkage on heat and momentum transport as well as product yields.
- The impact of particle size on bed-to-surface heat transfer coefficient.

The physical phenomena that govern the problem of the fast pyrolysis of biomass in bubbling fluidised beds are:

- Multiphase flow of gas/liquid (Eulerian sand)/solid mixture.
- Fast pyrolysis of solid biomass particles (Reaction kinetics).
- Momentum transport from the bubbling sand to the discrete biomass particles.

- Heat transfer to the surface of biomass particles via gas and particle convection.
- Intra-particle heat transfer via conduction.
- Shrinkage of biomass.

The computational approach of each one of the physical phenomena is implemented according to the following procedure.

1. Description of the computational models and methods used from the scientific community.
2. Presentation of the physical laws that govern the process.
3. Implementation of the physical laws in a computational model as an extension to the commercial finite volume code FLUENT.
4. Application of the sub-model in problems characterising fluidised beds, and the effects of specific parameters in the operation of fluidised bed reactors for fast pyrolysis.

1.3 Elements of novelty

Several numerical models have been presented in the literature, simulating the hydrodynamics of fluidised beds using different numerical approaches and methodology, most of them in 2-Dimensional representations. Numerical models have also been presented in the literature modelling the pyrolysis of single biomass particles, targeting on the determination of the product yields and trying to quantify the various parameters that affect the process.

The novelty of the current study is that it combines the major phenomena that occur in fast pyrolysis in bubbling fluidised beds in a unified Computational (CFD) model. The study investigates the complex physical phenomena that govern the fast pyrolysis process. Specifically, a novel simulation model has been developed, which takes into account the simultaneous tracking of the particles inside the reactor and the heat, mass and momentum exchanges among the phases.

The model provides information about the instantaneous position of the biomass particles inside the reactor, with simultaneous evolution of vapours that occur during pyrolysis. The physical properties of the particles change according to the product formation as well as the transport phenomena that occur among the phases. In this way the necessary modifications that optimise the process can be made, regarding geometrical, heat, mass and momentum transport, feedstock particle size and particle shape considerations. The model can be applied to lab-scale and industrial size fluidised bed reactors as well as different processes such as gasification and combustion with minor changes in the computational code structure.

1.4 Progress of the research

The research started with the reviewing of the literature on numerical modelling of fluidised bed reactors, as well as the different stages of the fast pyrolysis process, involving the technology used, the basic chemistry of biomass pyrolysis and the various numerical models developed in the scientific community to simulate the degradation of biomass. Also, simple simulations were executed using FLUENT 6.2 to simulate the hydrodynamics of fluidised beds and to develop a basic idea of what was necessary to be done for a complete fast pyrolysis model. Extensive effort was put into the understanding of the structure of the code of FLUENT and the limitations of the multiphase models, in order to be able to develop a C-subroutine (User Defined Function) for simulating the fast pyrolysis of the discrete biomass particles immersed into a fluidised bed.

Since the basic idea of the project was formed, the code development started with simple simulations of discrete particles, moving freely inside the computational domain of the reactor, subjected to heat and momentum transport only by the fluidising gas (nitrogen). The incorporation of reaction kinetics in this simple configuration followed, including the mass sources of the produced condensable volatiles and their evolution inside the domain.

The basic target of the project started to being achieved, when the code was developed for the Eulerian computation of momentum transport inside the bubbling bed. A single discrete biomass particle was injected into a cold flow bubbling bed, without taking into account the pyrolysis reactions and its motion was examined for 2 and 3-Dimensional cases. Further extending the already momentum transport model, the bed-to-surface heat transfer and reaction kinetics of biomass had to be incorporated into the code. FLUENT does not provide to the user, the solution of the heat diffusion equation for discrete spherical particle, therefore, the code was developed in a way to account for the radial temperature and pyrolysis products distribution as well as the enthalpy of reaction effect due to phase change phenomena. The mass source of the produced volatiles was computed and loaded on the model and their evolution inside the reactor was modelled.

The developed code was applied to model various phenomena inside the fluidised bed reactor, such as the impact of the size and shape of the particles on char entrainment, the effect of shrinkage of the particles during pyrolysis for the specific kind of reactor as well as the effect of biomass particle size on bed-to-surface heat transfer coefficient.

The details of the research progress are thoroughly analysed in the following chapters of the thesis.

1.5 Thesis structure

The thesis is organised in six main chapters.

The current chapter gives a brief introduction on the history of development of the fluidised bed technology, together with brief historical notes about fast pyrolysis and its main characteristics as a process. The main research subject and scope is analysed, explaining the different processes and physical phenomena that occur in the fast pyrolysis in fluidised beds. The elements of novelty and the significance of the model are also described. The chapter finishes with the discussion of the progress of the research during the three years and the description of the outline of the thesis.

The second chapter reviews the various modelling approaches used by the scientific community for the hydrodynamics of the bubbling beds (Eulerian-Eulerian, Eulerian-Lagrangian), as well as the various numerical models developed for the fast pyrolysis of biomass. The review continues, discussing the reaction kinetics mechanisms of biomass developed, depending on the feedstock, and how they were applied to the different numerical models in the literature. Finally, the chapter reviews the previous studies on heat and momentum transfer on immersed surfaces in bubbling fluidised beds.

The third chapter provides the underlying theory of the model on the different physical phenomena that govern the fluidised bed operation and fast pyrolysis process. It starts with the basic principles of fluidisation, and the derivation of the general multiphase flow equations of motion, followed by their application to granular systems. It continues with the approach adopted for the momentum transported to a discrete particle inside a "Eulerian" sand bed together with the analysis of the forces acting on the particles. The chapter concludes with the interphase and intra-particle heat transfer correlations and equations together with the description of the mass balance equations for the pyrolysis products.

The fourth chapter starts with the exact description of the process that is modelled and continues with the presentation of the results for the computation of the momentum transport from the bubbling bed to the discrete biomass particle, analysing and quantifying the forces that act on the particle. The geometrical approach of the problem is also described by comparing a 2-D and a 3-D case. Further description of the findings is given regarding the bed-to-surface heat transfer and the association of the reaction mechanism of biomass with the discrete particle inside the reactor. The vapours produced are released in the domain and their interaction with the bubbling sand and the fluidising gas is modelled. The chapter concludes with the discussion of the advantages, drawbacks and conclusions of the developed computational model and how further modifications could improve its versatility.

The fifth chapter gives an insight on the applicability of the developed model and the significant information that it can provide regarding that fast pyrolysis process in bubbling fluidised beds. Four different applications have been performed and each one is analysed separately. First, the impact of the particle size on char entrainment from the fluidised beds is examined. The second application concerns the impact of the different particle shapes on the entrainment of char from the fluidised beds. The third application models the impact of the shrinkage of biomass on the different physical phenomena such as, heat and momentum transport, product yields, particle properties and char residence time. Finally, the fourth application focuses on the impact of the different particle sizes on the bed-to-surface heat transfer coefficient and how in turn, this affects the fast pyrolysis of the particles. The chapter ends with the conclusions made from the applications of the model.

The sixth and final chapter of the thesis discusses the conclusions derived from the research and describes significant observations for the optimum operation of the specific fluidised bed reactor. Also, recommendations for future work are given at the very end of the report.

The six main chapters of the thesis are followed by three appendices.

Appendix A provides a basic description of the characteristics of the computational grid used for modelling the geometry of the reactor.

Appendix B focuses on the basic CFD principles by simply describing the different discretisation schemes and pointing out the multiphase flow model limitations of FLUENT. The appendix continues with the analytical description of the development of the User Defined Function for fast pyrolysis. Finally, the simulation sequence is presented with the use of a simulation flow chart to make the understanding of the modelling procedure more convenient to the reader.

Appendix C simply presents the Reynolds transport theorem to ease the reader in the understanding of the derivation of the general transport equations derived in section 3.2.

Chapter 2

Literature review

The chapter provides the review of the previous studies in the fields of the numerical approaches for simulating the hydrodynamic behaviour, as well as the ways of heat and momentum transport in fluidised beds. Also, the numerical models developed from the scientific community for the pyrolysis of biomass are presented, together with the various reaction mechanisms of biomass. The discussion is presented on a theoretical basis as much as possible, since the development of the mathematical equations that govern the phenomena of multiphase flow, momentum transport, heat transfer and biomass reactivity are analytically presented in Chapter 3. The author will try to point out the main scientific developments of each section as briefly as possible, since the information and international scientific bibliography on these subjects are vast.

2.1 Gas-solid flow in fluidised beds

Different flow regimes occur, resulting in different hydrodynamic characteristics, when a gas is forced through a bed of particles. The flow regime depends on the operating conditions, solids flow rate, gas flow rate, and reactor configuration affecting the quality of fluidisation and the overall performance of the system. An important factor that significantly affects the quality of fluidisation is the properties of the solid particles (size distribution, shape, density, and restitution coefficient). Fig. 2.1 illustrates the different types of engineering reactors that can be found in industry.

Geldart [9] came up with four different kinds of particle behaviours. The classification from the smallest to the largest particle is as follows:

Figure 2.1: Types of fluidised bed reactors [8].

- **Group C**: This class of solids includes very fine and cohesive powders, e.g. cement, flour, starch etc. With this class, normal fluidisation is extremely difficult because the interparticle forces are greater than those resulting from the action of gas. Channelling takes place when fluidised.

- **Group A**: Solid particles having a small mean particle size or low particle density ($<\sim 1400 kg/m^3$). Typical examples of this class are catalysts used

Figure 2.2: The Geldart classification of particles for air at ambient conditions. Region A': Range of properties for well-behaved FCC catalyst [1].

for fluid catalytic cracking (FCC) processes. These solids fluidise easily, with smooth fluidisation at low gas velocity and bubbling/turbulent fluidisation at higher velocity.

- Group B: Solids having particle size $40\mu m < d_p < 500\mu m$ and density in the range $1400 < \rho_s < 4000 kg/m^3$. These solids fluidise vigorously with formation of bubbles, which grow in size; e.g. sand particles.
- Group D: These solid particles are large and/or dense and are spoutable. Deep beds of these solids are difficult to fluidise. Large exploding bubbles or severe channelling may occur in fluidisation of group D solids. Drying grains and peas, roasting coffee beans, gasifying coals, and some roasting metal ores are such solids, and they are usually processed in shallow beds or in the spouting mode.

Fig. 2.2 shows the classification of Geldart for air fluidisation at ambient conditions and superficial velocity U_0 less than approximately $10U_{mf}$. However, density and particle size are not the only factors affecting the quality of fluidisation as used in

Geldart's classification. Several other solid properties, including angularity, surface roughness and composition play also an important role [10].

Ranade [11] describes the different fluidisation regimes of these particles. A fixed bed regime is defined when the velocity of the fluidising gas is low and the solids rest on the gas distributor. However, when superficial gas velocity is increased beyond a critical point, the bed is fluidised. This is the point at which all the particles are suspended by the upward flowing gas. The frictional force between particle and gas just counterbalances the weight of the particles. The gas velocity at which fluidisation begins is known as "*minimum fluidisation velocity*" (U_{mf}). When the velocity of gas is increased beyond the minimum fluidisation velocity, homogeneous (or smooth) fluidisation may exist for the case of fine solids up to a certain velocity limit. Beyond this limit (U_{mb}: minimum bubbling velocity), the bubbling behaviour of the bed starts. This is not the case though for large solid particles. In that case, the bubbling regime starts immediately at the point where the gas velocity is higher than minimum fluidisation velocity ($U_{mb} = U_{mf}$). By increasing gas velocity, the movement of solids becomes more vigorous. Such a bed is called a bubbling bed or heterogeneous fluidised bed. Depending on the diameter and height of the bed, different behaviours have been observed. Deep beds of small diameter, appear slugging behaviour. The bubbles become large enough to spread across the diameter of the vessel. This is called a slugging bed regime. In large diameter vessels, turbulent motion of solid clusters and voids of gas of various size and shape are observed instead of slugs. In this case the entrainment of solids becomes significant. This regime is called a turbulent fluidised bed regime. By further increasing gas velocity, the entrainment of solids becomes even more intense and gas-solid separators (cyclones) become necessary. This regime is called a fast fluidisation regime. For a pneumatic transport regime, even higher gas velocity is needed and consequently all the solids are carried out of the bed. The most widely used regime map that can be found in literature is the one of Grace [12]. Several correlations that predict the minimum fluidisation velocity can be found on the literature [13–18], as well as correlations that estimate bubble sizes [19–21] and bubble rise velocities [22, 23].

By briefly introducing gas-solid flows in fluidised beds, the computational approaches for the modelling of such systems are described in the following section.

2.2 Computational modelling of fluidised beds

Gas-solid flows can be found on many different chemical processes, and fluidised beds are an essential part on many of these processes. To optimise the design and operation of such systems, the thourough understanding of the gas-solid flow patterns is necessary. The achievement of this target requires the development of both experimental techniques, and tools that will aid the numerical simulation of these systems. Due to the extreme increase in computational power the last decades, the simulation of fluidised bed hydrodynamics has become a reality. Researchers have developed computational models to deal with the complex nature of the gas-solid flow in fluidised beds. The two computational approaches that can be distinguished for modelling the gas-solid flow in a fluidised bed are the *non-continuum* (Eulerian-Lagrangian) and the *continuum* (Eulerian-Eulerian, two-fluid, multifluid) approaches. The two approaches mostly differ in the way that they treat the particulate phase. In the non-continuum approach, the particulate phase is treated as discrete particles that are tracked inside the domain, while in the continuum approach the particulate phase is treated as a continuum with an effective viscosity. Sections 2.2.1, 2.2.2 review the previous scientific work on these computational approaches.

2.2.1 Eulerian-Lagrangian modelling of fluidised beds

The use of discrete particle models (DPM) to simulate fluidised bed hydrodynamics offers a number of advantages, since several properties such as, gas and particle velocities, bed voidage etc., can be predicted, without disturbing the general flow field. In other words, provides information which would be impossible to gather only by experimentation.

Discrete element models or DPMs have been used for a wide range of applications from the time that were first proposed by Cundall and Strack [24]. However, the coupling of DPM with a finite volume description of the gas phase based on Navier-Stokes equations, was first reported by Tsuji et al. [25] for the soft-sphere model and Hoomans et al., [26] for the hard-sphere model.

- *Hard-sphere approach* - In a hard sphere system the motion of the particles is determined by momentum-conserving binary collisions. The interactions between the particles are pair-wise, additive and instantaneous [27].

- *Soft-sphere approach* - The soft sphere model uses a fixed time step and consequently the particles are allowed to overlap slightly. The contact forces are subsequently calculated from the deformation history of the contact using a contact force scheme [27].

The applicability of DPMs in gas fluidisation has been verified by comparison with experimental observations by several researchers [28–37], under different experimental conditions. Fig. 2.3 shows a comparison of discrete particle simulations with physical experiments for size segregation in gas fluidisation of binary mixtures of particles [37].

Hoomans et al., [38] have also shown the quantitative agreement between experiments and numerical simulations, by comparing the velocity maps obtained from Positron Emission Particle Tracking (PEPT) with the velocity field obtained from DPM simulations. The model assumed fully elastic, perfectly smooth collisions. Xu and Yu [30] showed that the trajectory of a specifically selected discrete particle located at the jet region of the fluidised bed moved everywhere on the bed. Thus, despite the dominance of the vertical motion on a fluidised bed, the particles can also move horizontally from left to right and vice versa. The results qualitatively agree with the PEPT findings of Seville et al., [39].

Clusters and bubbles are the two most common features that affect the performance and operation of the fluidised beds DPM simulations have also shown that they can predict the mechanisms of the various bubble dynamics (bubble formation, coalescence, disruption) in fluidised beds [40–44], something which has been traditionally studied using continuum methods. From the studies of Yuu et al. [40, 42], it was suggested that the high air fluctuating kinetic energy that occurs in fluidised beds is produced by the pressure gradient velocity correlations and dissipated by the air-particle interactions. Therefore, a continuum model must incorporate a suitable expression for the pressure term to correctly describe the particulate phase in a fluidised bed.

Several applications of the DPMs can be found on the literature, describing the advantages and limitations of these models. An analytical review of the DPMs can be found on Deen et al. [27] and Zhu et al. [45]. The equations that describe the DPMs are not presented in the current thesis, since the DPM approach is not adopted by the author in this study.

Figure 2.3: Snapshots for size segregation in gas fluidisation of binary mixtures of particles: (a) the simulated, and (b) the experimental snapshots when gas superficial velocity is $1.3m/s$, and initial state is well mixed; (c) the simulated and (d) the experimental snapshots when gas superficial velocity is $1.8m/s$, and initial state is fully segregated [37].

2.2.2 Eulerian-Eulerian modelling of fluidised beds

Eulerian-Eulerian models or granular flow models (GFM) are based on the interpenetrating continuum assumption. That means that the properties of the particle cloud are analogous to those of a fluid. For example, the bulk density or the mass of particles per unit volume is treated as a continuous property, and the velocity of the particle is the average velocity over an averaging control volume.

The first published work on the mathematical equations that describe the phenomenon of fluidisation, appeared on the literature in the mid-1960s [46–48]. The increase of the industrial applications involving gas-solid flows made the modelling of such systems a necessity for design and process optimisation. Bubbling fluidised beds are characterised by excellent solids mixing and gas-solid contact and distinct gas voids and bubbles exist. The Eulerian-Eulerian approach is considered particularly suitable for simulating the hydrodynamic behaviour of large industrial reactors which may contain billions of particles, making the DPMs to be extremely computationally intensive if not impossible.

Early work on the simulation of fluidised beds was restricted on the simulation of a single or a few bubbles for a short time in a two-dimensional fluidised bed [49], while the application of the model of Rivard and Torrey [50] by Tsuo and Gidaspow [51] showed the formation of the bubbles and propagation through the bed. In 1993 Clift [52], based on the state of the art results at the time, recommended that two-fluid models of dense bubbling beds should be used only as "learning models". However, significant improvements have been made since then to simulate the hydrodynamics of bubbling beds having a large number of bubbles. Gidaspow [53] incorporated the kinetic theory of granular flow in the Rivard and Torrey code and applied it to fluidised beds and risers. The idea was the introduction of granular temperature which is the kinetic energy associated with particle oscillation. The two-fluid model along with the kinetic theory of granular flow contains several modeled terms (stress tensor, solid phase bulk and shear viscosity, radial distribution function etc.). Models with different versions of each of these have been used [54], while Enwald et al. [55] used two different stress tensor models which resulted in similar results. The existence of bubbles is independent of which stress tensor model is used, since bubble formation occurs from the original two-fluid model formulation [56]. Fig. 2.4 shows the comparison of experimental data with DPM and two-fluid model of a bubble injection into the centre of a mono-disperse fluidised bed [57]. Balzer et al. [58] have also reported the results of a two-fluid model applied to a dense fluidised bed utilising results from the kinetic theory of granular media. The model showed that the results were sensitive to the value for the coefficient of restitution. The granular temperature decayed for values less than 0.9.

Numerical investigations have also been performed, testing the influence of the numerical scheme as well as mesh refinement on the solutions. There are several studies showing the effect of the discretisation scheme on the bubble shape and fluidised bed characteristics [55, 59–61]. The impact of mesh refinement on bed hydrodynamics was also studied [60, 62] and the results showed a strong influence on the bubble sizes as well as fluidisation velocities. Very recently, Junwu Wang et al. [63] showed why the two-fluid models fails to accurately describe the hydrodynamics of Geldart A particles inside bubbling gas-fluidised beds. Their answer was that

Figure 2.4: Injection of a single bubble into the centre of a mono-disperse fluidised bed (bed width: 0.30 m), consisting of spherical glass beads of 2.5mm diameter at incipient fluidisation conditions. Comparison of experimental data (top) with DPM (centre) and TFM (bottom) simulation results for 0.1, 0.2, and 0.4s after bubble injection [57].

sufficiently fine grid size and small time step must be used. Also, the impact of the correlations for the momentum exchange coefficients for gas-solid systems developed by Gidaspow [53], Syamlal and O'Brien [64] and Wen and Yu [65] was studied by Taghipour et al. [66] and compared with experimental data. The results showed reasonable agreement for most of the operating conditions.

Extensive reviews of the applications of two-fluid models can be found in [11, 67], as well as comparisons of simulations from DPMs and two-fluid models can be found in [68]. Further discussion on modelling the formation of bubbles can be found in [69–71].

2.3 Heat transfer in fluidised beds

Heat transfer in fluidised beds has been the subject of research for many researchers and one of the most important issues of gas fluidised beds. One of the greatest advantages of fluidised beds is the uniform temperature of the bulk of the bed due to the mixing generated by the rising bubbles, as well as their capability to exchange heat very effectively with the fluidising gas, due to the large surface area exposed by the particles [72]. The relationship between heat transfer coefficient and fluidising velocity is fairly well established [2, 73]. If the superficial velocity is increased above the minimum value for fluidisation, the heat transfer coefficient initially shows a sharp increase to a maximum, and then gradually decreases for higher fluidising velocities [74].

For fast pyrolysis in fluidised beds, the most significant parameter that needs to be defined is the heat transfer coefficient between the bulk of the bed and fixed or freely moving surfaces immersed into the bulk of the bed [1, 75]. There are several studies that employed different methods to measure the heat transfer coefficient between a moving sphere inside a bubbling bed for particles of greater as well as smaller diameter than those of the particles of the bed. Boterill [2] and Yates [76] studied the heat transfer between a bubbling fluidised bed of smaller particles to a fixed cooling tube or a stationary wall. Agarwal [77] studied the heat transfer to a large freely moving particle in gas fluidised bed of smaller particles and Parmar and Hayhurst [74] tried to measure the heat transfer coefficient for freely moving phosphor bronze spheres (diam. $2-8mm$) around a bed of hot sand fluidised by air. Mickley and Fairbanks [78] first pointed out that bed-to-surface heat transfer is an unsteady process in which "packets" of the emulsion phase carry heat to or from the surface residing there for a short period of time, before moving back to the bulk of the bed and being replaced by new material. Emulsion packet models have also been reported to the literature by Baskakov et al. [79] and Yoshida et al. [80]. Also, studies on the influence of bed particle size to the heat transfer coefficient have been performed by Collier et al., [81] and a Nusselt number based on the thermal conductivity of the gas was derived for ($U \leqslant U_{mf}$), while for ($U > U_{mf}$) the Nusselt number appeared to have a constant value. Fig. 2.5 shows the measured values of the heat transfer coefficient against U/U_{mf} for different size spheres inside a fluidised bed from the experiments of Collier et al. [81]. Scott et al. [82], measured the coefficient of heat transfer to a mobile sphere in a fluidised bed of relatively large particles. Also, they studied the case where $U_0 < U_{mf}$ and the solids were stationary at the bed. The basic feature of their experiments is that the heat-transfer sphere

Figure 2.5: Plot of measured h against U/U_{mf} for: ▲, $d_s = 5.56mm$; □ $d_s = 3.0mm$; ○, $d_s = 2.0mm$, with d_b as shown; (a) is for measurements with silica spheres in the fluidised bed; (b) is for hollow spheres of polypropylene [81].

was of a size comparable to that of the bed particles. According to their findings, at high Reynolds numbers ($100 < Re_{mfs} < 830$) and with small spheres in a bed of large particles ($0.2 < d_s/d_p < 2.75$), the dominant mechanism of heat transfer is found to be the flowing gas. Di Natale et al. [83] developed a semi empirical single particle model for the description of heat transfer coefficient between a submerged surface and a fluidised bed. It was found that the model could be successfully applied to fluidised beds of particles with Archimedes number higher than about, $Ar > 200$, while for finer particles the cluster based approach [84] was found to be more reliable. The same authors have also studied the effect of the surface shape on heat transfer coefficient [85]. Their work was focused on the influence of bed material properties and surface geometry on heat transfer coefficient.

Numerical investigations have also been performed using the Eulerian approach [86–88] and the results showed a strong coupling between the local solid volume distribution and the heat transfer coefficients. They also showed a good agreement with the penetration theory [78, 86] as well as the influence of the rising bubbles. Wang et al. [89] modelled the heat transfer between a high-temperature fluidised bed with magnesite and hollow-corundum sphere particles of diameter $0.35 - 1.21mm$ as bed materials and an immersed surface is simulated using the surface-particle-emulsion heat transfer model developed by the same authors [90]. The results showed that the temperature distribution in the emulsion phase within one particle diameter is inhomogeneous, as well as that the instantaneous heat transfer coefficient increases with increasing surface temperature. Also, the heat transfer coefficient has a maximum value at certain U/U_{mf}, and that with increasing bulk density and decreasing particle diameter, the heat transfer coefficient increases.

Numerous heat transfer correlations have been reported in the literature. Further discussions about the validity and reliability of the models as well as comparisons with experimental data can be found on [1, 2, 91, 92].

2.4 Numerical modelling of biomass pyrolysis

Several numerical models have been developed and applied to biomass pyrolysis [93–108]. Most of the models apply numerical analysis to determine heat, mass and momentum transport effects in a single biomass particle varying the pyrolysis conditions. Usually, the influence of parameters such as, size, shape, moisture, reaction mechanisms, heat transfer rates and particle shrinkage is the main objective of study. Sub-models for CFD applications have also been developed [112, 113] to make simulations of biomass pyrolysis possible and less computationally intensive.

The numerical investigations of di Blasi [93–96] are typical examples of single particle models, that study the heat, mass and momentum transport through biomass particles by varying the pyrolysis conditions, feedstock properties (implementing different chemical kinetics mechanisms), particle sizes, effect of shrinkage etc. The models provide very useful information about different conditions of pyrolysis and product yields and an be an excellent guide for every researcher on the field. The models of Babu and Chaurasia [101–106] treat the pyrolysis process in a similar way as the one of di Blasi, and focus more on the heat transfer effects and estimation of optimum parameters for biomass pyrolysis. They also study the effect of the enthalpy of reaction on product yields and vary the shrinkage parameters of biomass close to the complete degradation of the particles. They found that their approach gave better validation with experimental data compared to those of di Blasi. Fig. 2.6 shows the temperature profile as a function of time at different radial positions, for a large ($20mm$ diameter) particle with and without shrinkage from the work of Babu and Chaurasia [106]. Saastamoinen and Richard [99] studied the effect of drying to devolatilisation stating that the surface temperature of the particles after drying can exceed those of the initiation of devolatilisation, meaning that drying and pyrolysis may overlap. Peters and Bruch [109] tried to develop a flexible and stable numerical method to predict the thermal decomposition of large wood particles due to drying and pyrolysis. The model was applied to the drying process of wood particles and the process of pyrolysis was predicted for spruce, fir and beech wood. Larfeldt et al. [110] studied the influence from structural changes, heat transfer properties of dry wood and pyrolysis mechanism on the pyrolysis of large wood particles, and and Bryden et al. [111] modeled the pyrolysis of a wood slab on the thermally thick regime.

CFD sub-models for biomass pyrolysis have also been reported. Saastamoinen [112] has developed a mathematical sub-model for the devolatilisation of large particles for CFD applications. The model is based on solving two differential equations for the locations of two temperature isotherms, which are the drying and the devolatilisation isotherm. The model is also able to predict effects of particle size, shape, moisture, density and reactivity. Rostami et al. [113] have developed a CFD sub-model for biomass pyrolysis based on the Distributed Activation Energy Model (DAEM). In their work,the integrals that are present in DAEM and express

Figure 2.6: Temperature profile as a function of time with cylindrical pellet for different radial positions ($R = 0.02m$; $T_0 = 303K$; $T_f = 900K$) [106].

the complex reactions of biomass pyrolysis and the evolution of different volatile species, have been mathematically expressed in closed forms so that DAEM can be incorporated more efficiently in a CFD code. Their predictions was generally in good agreement with the experimental data and the accuracy can be improved by slight changes in the kinetic parameters. Computer codes based on Distributed Activation Energy Model (DAEM) for biomass devolatilisation currently are: bio-FG-DVC [114] and bio-FLASHCHAIN [115].

All the models previously described, model the pyrolysis of single biomass particles, mainly analysing heat transfer and chemical kinetics of biomass as well as the flow of volatiles through the pores of the particle. In some cases, the high heating rates of a fluidised bed reactor are incorporated, however, none of the models actually investigate the complex hydrodynamic phenomena of a fluidised bed with the simultaneous incorporation of a biomass pyrolysis sub-model into it. The current study extends even further the modelling of biomass pyrolysis in fluidised beds by incorporating a sub-model for biomass pyrolysis into the commercial finite volume code FLUENT taking into account the local heat transfer conditions as well as the motion of the biomass particles inside the reactor. Thus, the pyrolysis conditions are variable according to the state of fluidisation and the instantaneous particle positions, depending on the volume fraction of each phase. The evolution of volatiles inside the reactor is also modeled.

Reviews on the numerical models for biomass pyrolysis can be easily found in the literature. An extensive review of many of the numerical models available can be found in [116].

2.5 Chemical kinetics of biomass pyrolysis

Advanced computational models can be produced with the incorporation of the kinetic mechanisms of pyrolysis combined with heat, mass and momentum transport phenomena, which can be of great importance in the design and optimisation of chemical reactors.

Primary degradation of biomass starts at about $500K$, fast rates are attained at about $573K$ and the process is practically terminated at $700-750K$ [116–119]. Thermogravimetric curves, measured for dynamic or isothermal conditions have been used to formulate a) one-step global, b) one-step multi-reaction and c) multi-step semi-global reaction mechanisms, which include the effects of reaction parameters and feedstock properties. Studies [120–123] have suggested that primary decomposition of biomass can be modeled taking into account the degradation rates of its main components (hemicellulose, cellulose, lignin) and their thermal behaviour. Indeed, hemicellulose decomposes at $498-598K$, cellulose at $598-648K$ and lignin at $523-773K$ [116]. If the heating rates and temperatures are higher, then simultaneous degradation is observed by all components. The main products of biomass pyrolysis are classified as condensable volatiles also referred as liquids (vapours), non-condensable volatiles (gases) and char. Given that holocellulose (hemicellulose+cellulose) is mainly responsible for the production of liquids, lignin is the major component responsible for the production of gases and char. At low temperatures, a competition between liquid and char formation exists with the former being successively more favoured. At high temperatures, gas formation rates tend to increase due to the predominance of devolatilisation (versus charring) of lignin decomposition [116]. Secondary reactions of vapours effectively become active at high temperatures and long residence times [124–127]. Secondary reactions can take place at the pores of the particle while undergoing primary pyrolysis as well as over the char surfaces and extra-particle surfaces, which crack the vapour product into light molecular weight volatiles.

As it was mentioned earlier, the reaction mechanisms for biomass pyrolysis can be distinguished in three major categories: a) one-step global, b) one-step multi-reaction and c) multi-step semi-global reaction mechanisms.

One-step global scheme: The one-step global scheme [129–133] uses a very simple mechanism to describe the decomposition of the virgin fuel into volatiles, gases and char (eq. 2.1).

$$Virgin\,Fuel \xrightarrow{K} Tar + Gas + Char \tag{2.1}$$

The scheme utilises the Arrhenius equation (eq. 2.2) for the rate of reaction which is considered to be proportional either to the weight residue or to the weight loss of the fuel. The kinetic parameters are obtained through experiments using thermogravimetric analysers (TGA), tube furnaces, fluidised bed reactors and in *situ* measurement techniques.

$$K = Aexp(-E/RT) \tag{2.2}$$

The major limitation of one-step global schemes is that they are neither able to predict the composition of volatiles nor to account for various components of the virgin fuel, which can be very important in some applications. For fuels such as wood which is composed of constituents, such as cellulose, hemicellulose and lignin each with a different chemical kinetic behaviour, it is often erroneous to lump all the constituents together and to treat the virgin fuel as a homogeneous solid [128].

One-step multi-reaction scheme: The one-step multi-reaction schemes [110, 113, 134–137] have been developed to overcome these limitations. For inhomogeneous fuels such as biomass etc., one-step reactions are written for each constituent (eq. 2.3). The overall rate of pyrolysis is then considered to be the sum of the rates of the individual constituents in a fashion consistent with their percentage in the virgin fuel [128].

$$Virgin\,Fuel\,Component_{(i)} \xrightarrow{K_i} Volatiles + Char \tag{2.3}$$

The major limitation of the one-step multi-reaction scheme is that they do not take into account the secondary reactions.

Multi-step semi-global scheme: Multi-step semi-global schemes [103–105, 108, 138, 139] describe reaction paths for both primary and secondary reactions. In these schemes usually the fuel is assumed to first decompose to so called "active" intermediates with lower degrees of polymerisation. These intermediates are then decomposed to other products. The most widely used kinetic schemes of this kind are shown in figs. 2.7 and 2.8 for cellulose and wood pyrolysis respectively.

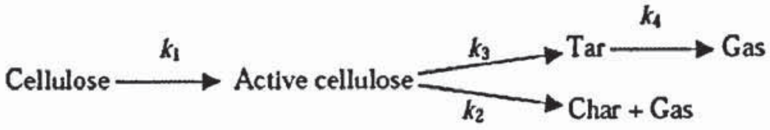

Figure 2.7: The mechanism for cellulose pyrolysis [140].

Figure 2.8: Two-stage semi-global mechanism for wood pyrolysis [141].

In both schemes the virgin fuel is decomposed to form three lumped product groups: char, heavy molecular weight tar vapours, and low molecular weight gases. All reactions are assumed to be first order, irreversible and follow Arrhenius law (eq. 2.2) [128]. The reaction kinetics scheme for biomass of Koufopanos et al. [142] (fig. 2.9) has also been widely used, where the reactions are assumed to be different than first order and biomass is decomposed to volatiles, gases and char. Fig. 2.10 shows

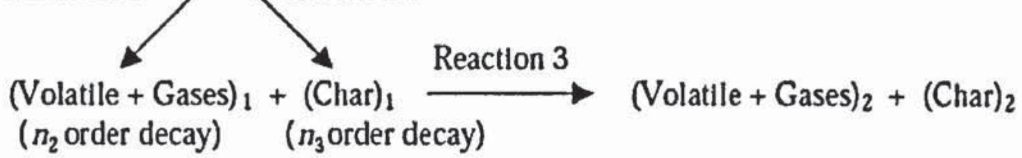

Figure 2.9: Reaction mechanism of Koufopanos et al. [142].

Figure 2.10: (a) Char yield from biomass pyrolysis as a function of final temperature for a heating rate of $50K/s$. (b) Tar and gas yield from biomass pyrolysis as a function of final temperature for a heating rate of $50K/s$ [138].

the primary pyrolysis products (char, tar, gas yields) from biomass pyrolysis using a semi-global model (fig. 2.8) without taking into account the secondary reactions of tar. Three different model samples were used (TM, C and F) to account for the different feedstock properties by applying different kinetic parameters. The TM model used oak wood ($0.615 - 1mm$ particles), the C model wood with kinetic parameters estimated from the literature, while F model used almond shells ($0.297-0.5mm$ particles). The kinetic parameters of these models can be found in [138].

The current study is mainly focused on the pyrolysis of wood. Therefore, the two-stage semi-global mechanism shown in fig. 2.8 is extensively used throughout the thesis. Also, the term "vapours" is used to refer to condensable volatiles from biomass pyrolysis instead of the term "tar" as shown in fig. 2.8. The term "tar" though, is used in the chemical kinetics equations throughout the thesis to correspond to the reaction kinetics scheme shown in fig. 2.8. At the initial stages of the research, numerical investigation had also been performed for cellulose pyrolysis making use of the mechanism shown in fig. 2.7.

Chapter 3

Mathematical theory

The chapter discusses the basic theory of fluidised bed operation and analyses the major physical phenomena that occur in a fluidised bed reactor such as, fluidisation, conservation of mass, momentum and energy for the gas and solid phases, interphase heat transfer, heat diffusion inside spherical particles and forces on discrete particles in gas/liquid/solid mixtures. The chapter presents the main body of the theory used for the development of the computational model discussed in appendix B while the theoretical extensions on the completed computational code (biomass shrinking conditions, sphericity effects, impact of particle size on heat transfer) are described separately on each corresponding section of chapter 5.

3.1 Fluidisation

Gas-solid flows were briefly introduced in section 2.1 by describing the different classification of particles and fluidisation regimes. In this section the dynamics of fluidisation are analysed in more detail and the basic phenomena and equations that govern fluidisation are introduced.

3.1.1 Bed pressure drop

If particles such as sand are poured into a tube with a porous plate distributor, and a gas or liquid is forced upward through the bed, then the flow causes a pressure drop across the bed. When this pressure drop is sufficient to support the weight of the particles (eq. 3.1), then the bed is considered at "minimum fluidisation". For good quality fluidisation the pressure drop at the distributor must be 10 to 20 % of the weight of bed [53]. Therefore, the onset of fluidisation occurs when,

$$\begin{pmatrix}\text{pressure drop}\\ \text{across bed}\end{pmatrix}\begin{pmatrix}\text{cross-sectional}\\ \text{area of tube}\end{pmatrix}=\begin{pmatrix}\text{volume}\\ \text{of bed}\end{pmatrix}\begin{pmatrix}\text{fraction}\\ \text{consisting}\\ \text{of solids}\end{pmatrix}\begin{pmatrix}\text{specific}\\ \text{weight}\\ \text{of solids}\end{pmatrix}, \tag{3.1}$$

or,

$$\Delta P_{bed} A_t = A_t L_{mf}(1-\varepsilon_{mf})(\rho_s-\rho_g)g. \tag{3.2}$$

The frictional pressure loss, over the whole operating range normally encountered for packed beds, has been corellated by Ergun [143] (eq. 3.3). It is simply the addition of the unrecoverable pressure loss due to viscous effects (low velocity, viscous flow) and inertial effects (high velocity, inertia dominated flow) [144].

$$\Delta P_{fr} = \underbrace{150\cdot\frac{\mu_g L U_0}{(\phi_s d_p)^2}\cdot\frac{(1-\varepsilon)^2}{\varepsilon^3}}_{\text{Viscous term}}+\underbrace{1.75\cdot\frac{\rho_g L U_0^2}{\phi_s d_p}\cdot\frac{(1-\varepsilon)}{\varepsilon^3}}_{\text{Inertial term}}. \tag{3.3}$$

Thus, at incipient fluidisation the minimum fluidising velocity can be calculated by combining equations 3.2 and 3.3

$$\frac{1.75}{\phi_s\varepsilon_{mf}^3}\left(\frac{d_p U_{mf}\rho_g}{\mu_g}\right)^2+\frac{150(1-\varepsilon_{mf})}{\phi_s^2\varepsilon_{mf}^3}\left(\frac{d_p U_{mf}\rho_g}{\mu_g}\right)=\frac{d_p^3\rho_g(\rho_s-\rho_g)g}{\mu^2}, \tag{3.4}$$

or in terms of the particle Reynolds number and Archimedes number,

$$\frac{1.75}{\phi_s\varepsilon_{mf}^3}\mathrm{Re_{p,mf}}^2+\frac{150(1-\varepsilon_{mf})}{\phi_s^2\varepsilon_{mf}^3}\mathrm{Re_{p,mf}}=\mathrm{Ar}, \tag{3.5}$$

since the particle Reynolds number and Archimedes number are defined as

$$\mathrm{Re_{p,mf}}=\left(\frac{d_p U_{mf}\rho_g}{\mu_g}\right), \tag{3.6}$$

and

$$\mathrm{Ar}=\frac{d_p^3\rho_g(\rho_s-\rho_g)g}{\mu^2} \tag{3.7}$$

respectively. In the special case of very small particles eq. 3.4 simplifies to

$$U_{mf} = \frac{d_p^2(\rho_s - \rho_g)g}{150\mu} \cdot \frac{\phi_s^2 \varepsilon_{mf}^3}{1 - \varepsilon_{mf}}, \quad \mathrm{Re_{p,mf}} < 20. \tag{3.8}$$

Fig. 3.1 shows the pressure drop vs gas superficial velocity diagram, which is very useful as an indicator of the quality of fluidisation. The straight line region OA is the "packed bed" region, where the solid particles have a constant separation and their relative motion is zero. The pressure drop at this region is described in general by the Ergun equation (eq. 3.3). The region BC is the region where the bed is fluidised and bubbling occurs, where eq. 3.2 applies.

Figure 3.1: Pressure drop versus fluid velocity for packed and fluidised beds [145].

3.1.2 Bubble flow

Bubble size and rise velocity

Several studies [20, 146, 147] have shown that the fluidising gas passes through the bed in the form of "observable" bubbles as well as gas through the emulsion of the solids. This is contrary to the simple two-phase model which assumes that all the excess gas of U_{mf} (i.e $U_0 - U_{mf}$), passes through the bed in the form of bubbles, while the emulsion of solids remain at minimum fluidising conditions, stationary except when moving aside to let bubbles through [148].

Bubbles in fluidised beds can appear in irregular shapes and different sizes. For application reasons, the mean volumetric size has been defined as a spherical bubble of diameter d_b. Overall, bubbles reach a small limiting size in fine particle systems, large in larger particle systems and unlimited size in very large particle systems. There are many correlations in the literature that try to estimate the growth of bubbles in fluidised beds [19, 20, 149, 150]. For reference purposes, the correlation of Hilligardt and Werther [149] for Geldart A,B and D particles is given by

$$d_b = d_0(1 + 27(U_0 - U_{mf}))^{1/3}(1 + 6.4h_{dist})^{1.2}, \tag{3.9}$$

where h is the height above the distributor. The values of the initial bubble size at the distributor d_0 for different class of Geldart particles and bed geometry, are given in table 3.1.

Value of d_0	Geldart particle	Bed geometry
0.0061	A	3D
0.0085	B	3D
0.0123	D	3D
0.01955	D	2D

Table 3.1: Values of initial bubble size at the distributor (d_0).

The rise velocity of the bubble for the whole range of particles can be estimated from the equation of Werther [21].

$$U_b = \psi_b(U_0 - U_{mf}) + \alpha U_{br}, \tag{3.10}$$

where ψ is the fraction of visible bubbles given by

$$\psi_b = \frac{U_b}{(U_O - U_{mf})A_t} \tag{3.11}$$

and α is a factor that accounts for the deviation of bed bubbles from single rising bubbles (Table 3.2).

Geldart particle	A	B	D
α	$3.2d_t^{1/3}$	$2.0d_t^{1/2}$	0.87
d_t (m)	$0.05 - 1.0$	$0.1 - 1.0$	$0.1 - 1.0$

Table 3.2: Values of α as a function of bed diameter for different Geldart type solids.

The single bubble rise velocity (U_{br}) is given by

$$U_{br} = 0.711\sqrt{gd_b}. \tag{3.12}$$

The reason for the estimation of parameters such as bubble sizes and bubble rise velocities in bubbling fluidised beds, is to be able to predict the performance of such systems in physical and chemical operations. These parameters can be very important in the scale-up or scale down of reactors since the volume fraction of phases, velocities of gases and solids etc. can be reasonably estimated.

3.2 Transport equations for multiphase systems

3.2.1 Basic concepts

The basic approach for the derivation of balances in multiphase systems is the assumption that the system consists of a sufficient number of particles so that discontinuities can be smoothed out. That means that the derivatives of the various properties of the system exist and are continuous. The Reynolds transport theorem (Appendix C) is therefore used for an arbitrary property ζ per unit volume. Thus, for a volume (V) in space, that may change in time (t) and bounded by a closed surface, the following identity exists [53, 151].

$$\frac{d}{dt_i}\iiint\limits_{V(t)} \zeta dV = \iiint\limits_{V(t)} \left(\frac{\partial \zeta}{\partial t} + \nabla \cdot \zeta v_i\right) dV. \tag{3.13}$$

The system of eq. 3.13 moves with velocity v_i. The differentiation with respect to time carries the subscript i to emphasise this fact. In the derivation of multicomponent mass balances for single phase flow, ζ is the partial density of the component i, and the volume V is the same for all species. In multiphase flow, the volume occupied by phase i cannot be occupied by another phase at the same time and at the same position in space. This introduced the concept of volume fraction (ε_i) of phase i. Therefore, in a multiphase system

$$V_i = \iiint\limits_{V(t)} \varepsilon_i dV, \quad \text{where} \quad \sum_{i=1}^{n} \varepsilon_i = 1, \tag{3.14}$$

where $i = 1, 2, ..., n$ is the number of phases in the multiphase system. When the fluid is incompressible and no phase changes occur, then V_i is a constant and its derivative in time will be zero. Applying Reynolds transport theorem to eq. 3.14

we get

$$\frac{d}{dt_i}\iiint\limits_{V(t)} \varepsilon_i dV = \iiint\limits_{V(t)} \left(\frac{\partial \varepsilon_i}{\partial t} + \nabla \cdot \varepsilon_i v_i\right) dV = 0, \tag{3.15}$$

resulting to

$$\frac{\partial \varepsilon_i}{\partial t} + \nabla \cdot \varepsilon_i v_i = 0. \tag{3.16}$$

Eq. 3.16 is known as the incompressibility equation in multiphase flow.

3.2.2 Balance of mass

In multiphase systems the mass of phase i can be given in terms of its volume fraction (ε_i) and density (ρ_i). Therefore,

$$m_i = \iiint\limits_{V(t)} \varepsilon_i \rho_i dV \tag{3.17}$$

The postulate of mass balance of phase i is

$$\frac{dm_i}{dt_i} = \frac{d}{dt_i}\iiint\limits_{V(t)} \varepsilon_i \rho_i dV = \iiint\limits_{V(t)} \Gamma_i dV, \tag{3.18}$$

where Γ_i is the rate of production of mass o phase i per unit volume, due to phase change or chemical reaction. It is obvious that with no phase change or chemical reaction, the right hand side of eq. 3.18 would be equal to zero. Applying eq. 3.13 to eq. 3.18 we get the final form of the differential equation of mass balance

$$\frac{\partial(\varepsilon_i \rho_i)}{\partial t} + \nabla \cdot (\varepsilon_i \rho_i v_i) = \Gamma_i. \tag{3.19}$$

The conservation of mass requires that the sum of Γ_i over all phases be zero, that is

$$\sum_{i=1}^{n} \Gamma_i = 0. \tag{3.20}$$

3.2.3 Balance of momentum

The momentum of phase i in a multiphase system is defined as $\iiint_{V(t)} \varepsilon_i \rho_i v_i dV$. Newton's second law states that the rate of change of momentum of a system is equal to the sum of forces acting on the system. The forces acting on a multiphase system are surface forces, gravitational forces, forces due to interaction of phase

i with other phases as well as forces due to the addition of mass to a phase i. Mathematically this statement can be expressed as

$$\frac{d}{dt_i}\iiint\limits_{V(t)} \varepsilon_i \rho_i v_i dV = \mathscr{F}_i^b + \mathscr{F}_i^s, \tag{3.21}$$

where $\mathscr{F}_i^b$ is the body source of momentum to phase i, and $\mathscr{F}_i^s$ is the surface source. The body source can be defined as

$$\mathscr{F}_i^b = \iiint\limits_{V(t)} (\underbrace{\varepsilon_i \rho_i \mathbf{b}_i}_{\substack{\text{external}\\ \text{forces}}} + \underbrace{\mathbf{M}_{ij}}_{\substack{\text{interaction forces}\\ \text{between faces}}} + \underbrace{\Gamma_i v_{ij})}_{\substack{\text{momentum change}\\ \text{due to phase changes}}} dV. \tag{3.22}$$

The term $\mathbf{b}_i$ is the body force per unit mass and is attributed to external forces (e.g gravitational force). The quantity $\mathbf{M}_{ij}$ is the force on phase i due to the interaction with the other phases j of the system. The source term $\Gamma_i v_{ij}$ is the source of momentum due to phase changes. The surface term $\mathscr{F}_i^s$ is defined as

$$\mathscr{F}_i^s = \oiint\limits_{S(t)} \mathbf{T}_i da, \tag{3.23}$$

where $\mathbf{T}_i$ is the *traction* (stress tensor), which is the source of per unit area of momentum of phase i. The vector surface element $da = \mathbf{n}dS$ where $\mathbf{n}$ is the unit exterior normal to surface S. In the 3-Dimensional space (x, y, z) the stress tensor $\mathbf{T}_i$ for phase i is given by

$$\mathbf{T}_i = \begin{pmatrix} T_{ixx} & T_{ixy} & T_{ixz} \\ T_{iyx} & T_{iyy} & T_{iyz} \\ T_{izx} & T_{izy} & T_{izz} \end{pmatrix}, \tag{3.24}$$

where its typical element T_{iyx} is the ith force in the x direction per unit area of the yth face (fig. 3.2)

$$T_{iyx} = \frac{\partial F_{ix}}{\partial A_y}. \tag{3.25}$$

The momentum balance then becomes

$$\frac{d}{dt_i}\iiint\limits_{V(t)} \varepsilon_i \rho_i v_i dV = \iiint\limits_{V(t)} (\varepsilon_i \rho_i \mathbf{b}_i + \mathbf{M}_{ij} + \Gamma_i v_{ij}) dV + \oiint\limits_{S(t)} \mathbf{T}_i da. \tag{3.26}$$

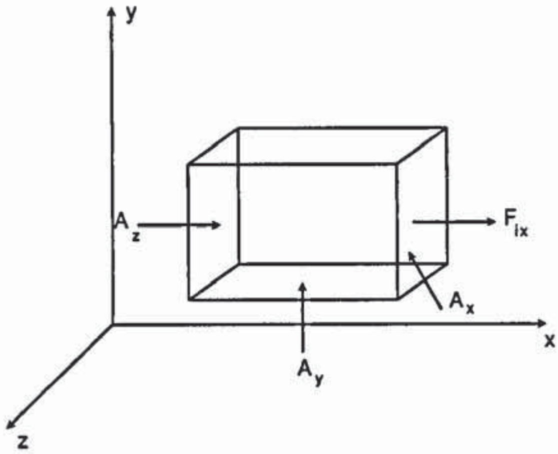

Figure 3.2: Stresses in multiphase balances. $T_{ixx} = \frac{\partial F_{ix}}{\partial A_x}$, $T_{iyx} = \frac{\partial F_{ix}}{\partial A_y}$, $T_{izx} = \frac{\partial F_{ix}}{\partial A_z}$

Applying the divergence theorem of Gauss in the surface integral of the stress tensor $\oiint_{S(t)} \mathbf{T}_i da = \iiint_{V(t)} \nabla \cdot \mathbf{T}_i dV$ we have

$$\frac{d}{dt_i}\iiint\limits_{V(t)} \varepsilon_i \rho_i v_i dV = \iiint\limits_{V(t)} (\varepsilon_i \rho_i \mathbf{b}_i + \mathbf{M}_{ij} + \Gamma_i v_{ij} + \nabla \cdot \mathbf{T}_i) dV. \tag{3.27}$$

Applying Reynolds transport theorem (eq. 3.13) to eq. 3.27 we get the differential form of the momentum balance equation for phase *i*.

$$\frac{\partial(\varepsilon_i \rho_i v_i)}{\partial t} + \nabla \cdot (\varepsilon_i \rho_i v_i \otimes v_i) = \varepsilon_i \rho_i \mathbf{b}_i + \mathbf{M}_{ij} + \Gamma_i v_{ij} + \nabla \cdot \mathbf{T}_i. \tag{3.28}$$

The next step is to define the constitutive equations for the stress tensor $\mathbf{T}_i$ and the forces of interaction between the phases $\mathbf{M}_{ij}$. The interaction forces consist of drag between the phases, added mass forces dependent on velocity gradients and of other interaction forces such as collisional forces etc. In its simplest form $\mathbf{M}_{ij}$ can be defined as

$$\sum_{i=1}^{n} \sum_{j=1}^{n} \mathbf{M}_{ij} = \sum_{i=1}^{n} \sum_{j=1}^{n} K_{ij}(v_i - v_j), \tag{3.29}$$

where K_{ij} is the interphase momentum exchange coefficient defined as

$$K_{ij} = \frac{\varepsilon_i \varepsilon_j \rho_i f}{\tau_i}. \tag{3.30}$$

The factor f is called the drag factor and τ_i is the particulate relaxation time. These terms are further analysed in section 3.4.

The stress tensor is expressed through the definition of phase pressure p_i and viscous stresses $\bar{\bar{\tau}}_i$ via the identity matrix $\mathbf{I}$

$$\mathbf{T}_i = -p_i\mathbf{I} + \bar{\bar{\tau}}_i. \tag{3.31}$$

The viscous stresses tensor $\bar{\bar{\tau}}_i$ for phase i is given in tensor notation by

$$\bar{\bar{\tau}}_{ij} = \varepsilon_i\mu_i(\frac{\partial v_i}{\partial x_j} + \frac{\partial v_j}{\partial x_i}) + \varepsilon_i\lambda_i\delta_{ij}\nabla\cdot v_i, \tag{3.32}$$

or in vector form

$$\bar{\bar{\tau}}_{ij} = \varepsilon_i\mu_i(\nabla v_i + \nabla {v_i}^T) + \varepsilon_i\lambda_i\nabla\cdot v_i. \tag{3.33}$$

The term μ_i is the "dynamic viscosity" of phase i and λ_i is called the "second coefficient of viscosity" of phase i. In order to close the equations for the normal stresses Stokes [152] made the hypothesis that

$$\lambda_i + \frac{2}{3}\mu_i = 0. \tag{3.34}$$

Eq. 3.34 is referred to as the "bulk viscosity". The symbol δ_{ij} is the Kronecker delta ($\delta_{ij} = 1$ if $i = j$ and $\delta_{ij} = 0$ if $i \neq j$). The superscript T indicates the transpose of the velocity gradient tensor.

3.2.4 Balance of energy

The basic principle that is applied in the derivation of the energy equation is the first law of Thermodynamics. It states that any changes in time of the total energy inside the volume are caused by the rate of work of forces acting on the volume and by the net heat flux into it [153]. The energy of phase i can be defined as

$$\iiint\limits_{V(t)} \varepsilon_i\rho_i\Big(e_i + \frac{1}{2}v_i^2\Big)dV, \tag{3.35}$$

where e_i is the internal energy per unit mass and the term $\frac{1}{2}u_i^2$ represents the kinetic energy of the mean motion. Therefore, the balance of energy is

$$\frac{d}{dt_i}\iiint\limits_{V(t)} \varepsilon_i\rho_i\Big(e_i+\frac{1}{2}v_i^2\Big)dV = \mathscr{W}_i^b + \mathscr{W}_i^s, \tag{3.36}$$

where $\mathscr{W}_i^b$ is the body source of energy to phase i, and $\mathscr{W}_i^s$ is the surface source. The body source is given by

$$\mathscr{W}_i^b = \iiint\limits_{V(t)} \underbrace{\varepsilon_i\rho_i(r_i+v_i\mathbf{b}_i)}_{\substack{\text{external sources}\\ \text{of energy}}} + \underbrace{(E_i+v_i\mathbf{M}_i)}_{\substack{\text{source due to interaction}\\ \text{with other phases}}} + \underbrace{\Gamma_i e_{ij}}_{\substack{\text{source of energy}\\ \text{due to source of mass}}} \; dV, \tag{3.37}$$

where r_i is the body force per unit mass attributed to external forces, E_i is the source to phase i due to interaction with other phases and $\Gamma_i e_{ij}$ is the source of energy due to the source of mass. The surface source is given by

$$\mathscr{W}_i^s = \oint\!\!\oint\limits_{S(t)} \varepsilon_i(\underbrace{\mathbf{T}_i v_i}_{\substack{\text{pressure and viscous}\\ \text{dissipation}}} - \underbrace{Q_i}_{\substack{\text{source of energy}\\ \text{to phase } i\\ \text{per unit total area}}})da, \tag{3.38}$$

where the first term on the right hand side $\mathbf{T}_i v_i$ represents the pressure and viscous dissipation and the second term Q_i the source of energy per unit total area [154]. An argument similar to that used previously shows the existence of a vector field

$$Q_i = \mathbf{n}\cdot\mathbf{q}_i \tag{3.39}$$

By doing similar manipulations as was done for the momentum balance equation (section 3.2.3), the energy of balance can be written as

$$\begin{aligned}\frac{\partial(\varepsilon_i\rho_i e_i)}{\partial t} + \nabla\cdot(\varepsilon_i\rho_i v_i e_i) &= \varepsilon_i\mathbf{T}_i : \nabla v_i - \\ &- \nabla\cdot\varepsilon_i\mathbf{q}_i + \varepsilon_i\rho_i r_i + E_i + \Gamma(e_{ij} - e_i - \frac{1}{2}v_i^2 + v_{ij}v_i).\end{aligned} \tag{3.40}$$

3.3 Eulerian dispersed multiphase flows

In the current study, the simulations of the bubbling behaviour of the fluidised bed were performed by solving the equations of motion of a multifluid system. The general multiphase flow equations were derived in section 3.2 and in the same manner the conservation equations for dispersed multiphase flows are presented in the current section. An Eulerian model for the mass and momentum for the gas (nitrogen) and solids-fluid phases, was applied, while the kinetic theory of granular flow, was applied for the conservation of the solids fluctuation energy. The governing equations are expressed in the following form.

Mass conservation

Eulerian-Eulerian continuum modelling is the most commonly used approach for fluidised bed simulations. The accumulation of mass in each phase is balanced by the convective mass fluxes. The phases are able to interpenetrate and the sum of all volume fractions in each computational cell is unity.
gas phase:

$$\frac{\partial(\varepsilon_g \rho_g)}{\partial t} + \nabla \cdot (\varepsilon_g \rho_g v_g) = 0, \tag{3.41}$$

solid phase:

$$\frac{\partial(\varepsilon_s \rho_s)}{\partial t} + \nabla \cdot (\varepsilon_s \rho_s v_s) = 0. \tag{3.42}$$

Momentum conservation

Newton's second law of motion states that the change in momentum equals the sum of forces on the domain. In gas-solid fluidised beds the sum of forces consists of the viscous force $\nabla \cdot \bar{\bar{\tau}}_s$, the solids pressure force ∇p_s, the body force $\varepsilon_s \rho_s g$, the static pressure force $\varepsilon_s \cdot \nabla p$ and the interphase force $K_{gs}(v_g - v_s)$ for the coupling of gas and solid momentum equations by drag forces. Other forces such as added mass, lift, Basset force are assumed to be negligible [155, 156].
gas phase:

$$\begin{aligned} &\frac{\partial(\varepsilon_g \rho_g v_g)}{\partial t} + \nabla \cdot (\varepsilon_g \rho_g v_g \otimes v_g) = \\ &\quad = -\varepsilon_g \cdot \nabla p + \nabla \cdot \bar{\bar{\tau}}_g + \varepsilon_g \rho_g g + K_{gs}(v_g - v_s), \end{aligned} \tag{3.43}$$

solid phase:

$$\begin{aligned} &\frac{\partial(\varepsilon_s \rho_s v_s)}{\partial t} + \nabla \cdot (\varepsilon_s \rho_s v_s \otimes v_s) = \\ &\quad = -\varepsilon_s \cdot \nabla p - \nabla p_s + \nabla \cdot \bar{\bar{\tau}}_s + \varepsilon_s \rho_s g + K_{gs}(v_g - v_s), \end{aligned} \tag{3.44}$$

where the solid-phase stress tensor is given by,

$$\bar{\bar{\tau}}_s = \varepsilon_s \mu_s \left(\nabla v_s + \nabla v_s^T\right) + \varepsilon_s \left(\lambda_s - \frac{2}{3}\mu_s\right) \nabla \cdot v_s \bar{\bar{I}}_s, \tag{3.45}$$

and the Gidaspow interphase exchange coefficient,

$$K_{gs} = \frac{3}{4} C_d \frac{\varepsilon_s \varepsilon_g \rho_g |v_s - v_g|}{d_s} \varepsilon_g^{-2.65} \qquad for \quad \varepsilon_g > 0.8, \tag{3.46}$$

$$K_{gs} = 150 \frac{\varepsilon_s^2 \mu_g}{\varepsilon_g d_s^2} + 1.75 \frac{\varepsilon_s \rho_g |v_s - v_g|}{d_s} \qquad for \quad \varepsilon_g \leqslant 0.8, \tag{3.47}$$

where the drag coefficient is given by

$$C_d = \frac{24}{\varepsilon_g Re_s} [1 + 0.15 (\varepsilon_g Re_s)^{0.687}], \tag{3.48}$$

and

$$Re_s = \frac{d_s \rho_g |v_s - v_g|}{\mu_g}. \tag{3.49}$$

Several other interphase exchange coefficients have also been reported in the literature [14, 64, 157–161]. The bulk viscosity λ_s is a measure of the resistance of a fluid to compression which is described with the help of the kinetic theory of granular flows [162]

$$\lambda_s = \frac{4}{3} \varepsilon_s \rho_s d_s g_{0,ss} (1 + e_{ss}) \sqrt{\frac{\Theta_s}{\pi}}. \tag{3.50}$$

The tangential forces due to particle interactions are summarised in the term called solids shear viscosity, and it is defined by Gidaspow et al. [163] as

$$\mu_s = \mu_{s,col} + \mu_{s,kin} + \mu_{s,fr}, \tag{3.51}$$

where the collision viscosity of the solids $\mu_{s,col}$ is

$$\mu_{s,col} = \frac{4}{5} \varepsilon_s \rho_s d_s g_{0,ss} (1 + e_{ss}) \sqrt{\frac{\Theta_s}{\pi}}, \tag{3.52}$$

the frictional viscosity

$$\mu_{s,fr} = \frac{p_s sin(\phi_{gs})}{2\sqrt{I_{2D}}} \tag{3.53}$$

and the Gidaspow [163] kinetic viscosity

$$\mu_{s,kin} = \frac{10\rho_s d_s\sqrt{\Theta_s\pi}}{96\varepsilon_s g_{0,ss}(1+e_{ss})} \times \left[1+\frac{4}{5}\varepsilon_s g_{0,ss}(1+e_{ss})\right]^2. \tag{3.54}$$

Other correlations for the solids shear viscosity have been reported by Gidaspow et al. [164], Syamlal et al., [157] and Chapman and Cowling [165]. The solids pressure p_s, which represents the normal force due to particle interactions [162], and the transfer of kinetic energy ϕ_{gs} are given by

$$p_s = \varepsilon_s\rho_s\Theta_s + 2\rho_s(1+e_{ss})\varepsilon_s^2 g_{0,ss}\Theta_s \tag{3.55}$$

and

$$\phi_{gs} = -3K_{gs}\Theta_s. \tag{3.56}$$

Fluctuation energy conservation of solid particles

The solid phase models discussed above are based on two crucial properties, namely the radial distribution function $g_{0,ss}$ and granular temperature Θ_s. The radial distribution function is a measure for the probability of interparticle contact. The granular temperature represents the energy associated with the fluctuating velocity of particles.

$$\begin{aligned}\frac{3}{2}\left[\frac{\partial}{\partial t}(\varepsilon_s\rho_s\Theta_s) + \nabla\cdot(\varepsilon_s\rho_s v_s\Theta_s)\right] &= \\ &= \left(-p_s\bar{\bar{I}}_s + \bar{\bar{\tau}}_s\right) : \nabla\cdot v_s + \nabla\cdot(k_{\Theta s}\cdot\nabla\cdot\Theta_s) - \gamma_{\Theta s}.\end{aligned} \tag{3.57}$$

where $\bar{\bar{\tau}}_s$ is defined in eq. 3.45. The diffusion coefficient of granular temperature $k_{\Theta s}$ according to Gidaspow [53] is given by:

$$\begin{aligned}k_{\Theta s} = {} & \frac{150\rho_s d_s\sqrt{\Theta_s\pi}}{384(1+e_{ss})g_{0,ss}} \\ & \left[1+\frac{6}{5}\varepsilon_s g_{0,ss}(1+e_{ss})\right]^2 + 2\rho_s d_s\varepsilon_s^2 g_{0,ss}(1+e_{ss})\sqrt{\frac{\Theta_s}{\pi}}.\end{aligned} \tag{3.58}$$

The radial distribution function $g_{0,ss}$ is defined as [166]

$$g_{0,ss} = \left[1-\left(\frac{\varepsilon_s}{\varepsilon_{s,max}}\right)^{1/3}\right]^{-1} \tag{3.59}$$

and the collision dissipation energy as

$$\gamma_{\Theta_s} = \frac{12(1 - e_{ss}^2) g_{0,ss}}{d_s \sqrt{\pi}} \rho_s \varepsilon_s^2 \Theta_s^{3/2}. \tag{3.60}$$

Other expression for the diffusion coefficient of granular temperature k_{Θ_s} can be found on [157, 162, 163, 169] and for the radial distribution function $g_{0,ss}$ on [167–169]. An analytical discussion of the solid-phase properties can be found on [170, 171].

3.4 Fluid-particle interaction

The interaction between a fluid and a single particle (droplet) refers to the exchange of properties (mass, momentum, energy transfer) between phases and is responsible for coupling in dispersed phase flows. The section will introduce the phenomena responsible for momentum transfer between the phases and will analyse the forces that act on single particles that are being carried by a fluid.

3.4.1 Momentum transfer

Momentum is transferred between the phases by interphase drag and lift. The forces that act on a particle carried by a fluid can be categorised as steady state drag forces, buoyancy force, unsteady forces (virtual mass, Basset force), lift forces (Saffman lift, Magnus force), and body forces (gravity, Coulomb forces, thermophoretic forces).

Steady-state drag

The steady state drag is the drag force acting on a particle or droplet in a uniform pressure field when there is no acceleration of the relative velocity between the particle and the carrier fluid. The force can be quantified by equation 3.61

$$F_D = \frac{1}{2} \rho_c C_D A |v_c - v_d| (v_c - v_d), \tag{3.61}$$

where ρ_c is the density of the continuous (carrier) phase, A is the projected area of the particle in the direction of the relative velocity, C_D is the drag coefficient and v_c, v_d the velocity of the continuous phase and particle respectively. Therefore, the equation of motion for a particle due to the action of drag would be

$$m_d \frac{dv_d}{dt} = \frac{1}{2}\rho_c C_D A |v_c - v_d|(v_c - v_d). \tag{3.62}$$

By simple rearrangements and simplifications eq. 3.62 can be written as

$$\frac{dv_d}{dt} = \frac{f}{\tau_u}(v_c - v_d), \tag{3.63}$$

where f is the drag factor and τ_u the velocity response time given respectively by

$$f = \frac{C_D \mathrm{Re_d}}{24}, \tag{3.64}$$

and

$$\tau_u = \frac{\rho_d d^2}{18\mu_c}. \tag{3.65}$$

The particle Reynolds number $\mathrm{Re_d}$ is given by

$$\mathrm{Re_d} = \frac{d\rho_c |v_d - v_c|}{\mu_c}. \tag{3.66}$$

The velocity response time expresses the time required for a particle released from rest to achieve 63% ($\frac{exp-1}{exp}$) of the free stream velocity. From eq. 3.65 one can see that the velocity response time is most sensitive to the particle size. For low values of $\mathrm{Re_d}$ the drag factor f approaches unity so eq. 3.63 becomes

$$\frac{dv_d}{dt} = \frac{1}{\tau_u}(v_c - v_d). \tag{3.67}$$

There are several correlations for the drag factor f in the literature [172–178]. The one used in this study is the correlation of Putnam [178]

$$f = 1 + \frac{\mathrm{Re_d}^{(2/3)}}{6} \qquad for \quad \mathrm{Re_d} < 1000 \tag{3.68}$$

$$f = 0.0183\mathrm{Re_d} \qquad for \quad 1000 \leqslant \mathrm{Re_d} < 3 \times 10^5, \tag{3.69}$$

which is a suitable correlation for the whole subcritical region ($\mathrm{Re_d} < 3\times10^5$). At the *critical Reynolds number*, $\mathrm{Re_d} > 3\times10^5$, there is a sudden drop of the drag coefficient (fig. 3.3) due to the development of a turbulent boundary layer around the particle, which moves the separation point of the rearward. The phenomenon is entirely due to boundary layer effects. If the particle is rough transition to turbulence occurs at

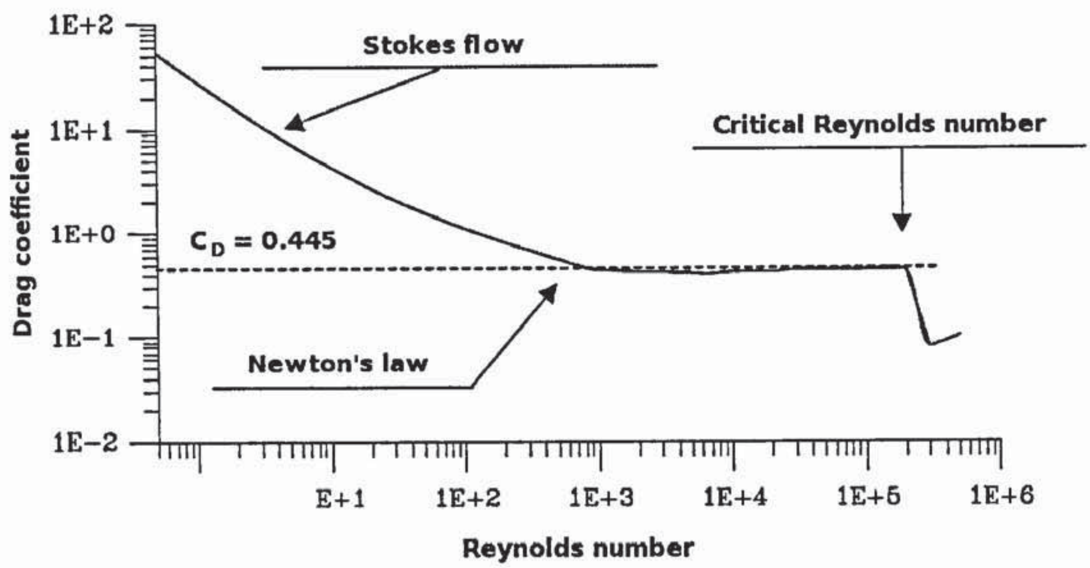

Figure 3.3: Variation of drag coefficient of a sphere with Reynolds number.

a lower Reynolds number and the critical Reynolds number is reduced.

Pressure gradient and buoyancy

The local pressure gradient in the fluid gives rise to a force in the direction of the pressure gradient. The pressure force acting on a particle is

$$F_p = \int_{cs} -p\mathbf{n}dS. \tag{3.70}$$

Applying Gauss divergence theorem,

$$F_p = \int_{cv} -\nabla p dV. \tag{3.71}$$

Assuming that the pressure is constant around the volume of the particle the pressure force is

$$F_p = -\nabla p V_d. \tag{3.72}$$

The pressure gradient due to hydrostatic pressure is given by

$$\nabla p = -\rho_c g \vec{e_z}, \tag{3.73}$$

where z is the direction opposed to gravity. Therefore, the pressure force is

$$F_p = \rho_c g V_d, \tag{3.74}$$

and the equation of motion becomes

$$m_d \frac{dv_d}{dt} = \frac{1}{2}\rho_c C_D A |v_c - v_d|(v_c - v_d) + mg - \rho_c g V_d, \tag{3.75}$$

or

$$\frac{dv_d}{dt} = \frac{f}{\tau_u}(v_c - v_d) + g\Big(1 - \frac{\rho_c}{\rho_d}\Big) \tag{3.76}$$

including gravitational and buoyancy effects.

Virtual mass effect

When a body is accelerated through a fluid, there is a corresponding acceleration of the fluid which is at the expense of work done by the body. The additional work relates to the virtual mass effect. The expression of the virtual mass effect is given by eq. 3.77

$$F_{vm} = \frac{\rho_c V_d}{2}\Big(\frac{Dv_c}{Dt} - \frac{dv_d}{dt}\Big). \tag{3.77}$$

This force is also called the *apparent mass* force because it is equivalent to adding mass to the sphere. The virtual mass force becomes important when $\rho_c > \rho_d$.

Basset force

The Basset force accounts for the viscous effects and addresses the temporal delay in the development of the boundary layer as the relative velocity changes with time. Reeks and McKee [179] have proposed eq. 3.78 for the Basset term, which includes the case when there is an initial velocity.

$$F_{Basset} = \frac{3}{2} d^2 \sqrt{\pi \rho_c \mu_c}\Big[\int_0^t \frac{\frac{Dv_c}{Dt} - \frac{Dv_d}{Dt}}{\sqrt{t - t'}} dt' - \frac{(v_c - v_d)_0}{\sqrt{t}}\Big] \tag{3.78}$$

Saffman lift force

The Saffman lift force [180] is due to the pressure distribution developed on a particle induced by a velocity gradient (fig 3.4). The higher velocity on the top gives rise

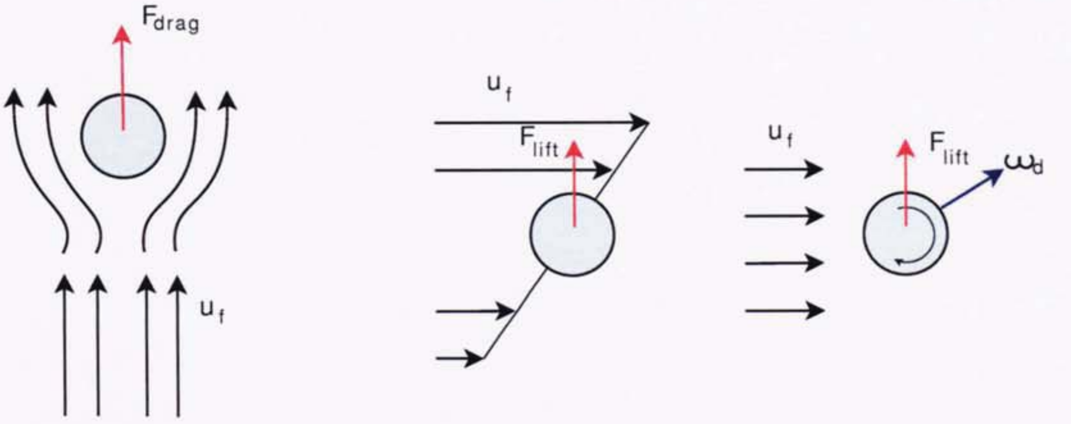

(a) Drag force

(b) Saffman lift force
(Particle in shear flow)

(c) Magnus lift force
(Lift on rotating particle)

Figure 3.4: Drag force, Saffman lift force and Magnus force acting on a single particle.

on lower pressure, while the lower velocity at the bottom side gives rise to higher pressure. and consequently a rise to a lift force. The Saffman lift force is given by

$$F_{saff} = 1.61d^2\sqrt{\mu_c\rho_c}\frac{1}{\sqrt{|\nabla \times v_c|}}[(v_c - v_d) \times \nabla \times v_c]. \tag{3.79}$$

If the relative velocity is positive the lift force is towards the higher velocity of the continuous phase. The opposite happens when the relative velocity is negative. Mei [181] proposed the following correction for $\mathrm{Re_d} >> 1$

$$\frac{F_L}{F_{saff}} = \begin{cases} (1 - 0.3314\sqrt{\beta})exp(\frac{-\mathrm{Re_d}}{10}) + 0.3314\sqrt{\beta} & \text{for } \mathrm{Re_d} \leqslant 40 \\ 0.0524\sqrt{(\beta\mathrm{Re_d})} & \text{for } \mathrm{Re_d} > 40 \end{cases}, \tag{3.80}$$

where

$$\beta = \frac{d}{2|v_c - v_d|}|\nabla \times v_c|. \tag{3.81}$$

Magnus force

The Magnus force is the lift developed due to rotation of the particles as shown in fig. 3.4. The force is induced by the pressure differences between both sides of the particle because of the differential velocity due to rotation. Rubinow and Keller [182] proposed the relationship 3.82 for the calculation of Magnus force

$$F_{Mag} = \frac{\pi}{8} d^3 \rho_c \Big[\Big(\frac{1}{2} \nabla \times v_c - \omega_d \Big) \times (v_c - v_d) \Big], \tag{3.82}$$

where $\frac{1}{2}\nabla \times v_c$ is the local fluid rotation, and ω_d is the rotation of the particle. If the particle rotation is equal to the local rotation of the fluid then inevitably the lift force is equal to zero.

Coulomb force

if the particle is electrically charged and moves inside an electric field, then the Coulomb force acts on it. The Coulomb force is given by

$$F_{Cou} = -q\mathbf{E}, \tag{3.83}$$

where q is the electric charge of the particle and $\mathbf{E}$ the electric field intensity.

Thermophoretic force

If a temperature gradient is present on the continuous phase then this gradient gives rise to the thermophoretic force. Epstein [183] proposed eq. 3.84 for the calculation of the thermophoretic force.

$$F_{Ther} = -\frac{9}{2} \mu_c d^2 Kn \sqrt{\frac{2\pi R}{T}} \frac{k_c/k_d}{1 + 2k_c/k_d} \nabla T, \tag{3.84}$$

where R is the gas constant for the carrier gas and k_c and k_d are the thermal conductivities for the continuous and dispersed phases respectively. The Knudsen number Kn is given by

$$Kn = \frac{\lambda}{d}, \tag{3.85}$$

and it is the ratio of the free mean path of the molecules and the particle diameter.

The forces that will be taken into account through the rest of the thesis are the drag, gravitational, buoyancy and virtual mass forces. The rest of the forces that were described in this section are either inapplicable or assumed to play a negligible role on the particle motion inside the bubbling fluidised bed.

3.5 Solid particles in bubbly flow

Three phase reactors are used extensively in chemical industries and considerable effort has been put in the modelling of three phase (gas/liquid/solid) systems. Different approaches have been used for different applications. Several researchers have used the Eulerian (multifluid) approach for the three phase simulation [184–190] but Euler/Lagrange methods have also been reported [191–193].

In the current study, the Eulerian approach is used to model the bubbling behaviour of the sand bed, therefore the fluidising gas and sand are treated as interpenetrating fluid. The biomass particles are injected into the bed as discrete (Lagrangian) particles and their motion inside the reactor is dominated by the forces described in section 3.4. The most important parameter for the correct representation of the momentum transport from the bubbling bed to the particles is the identification of regimes. When the particle is injected and wandered around the bed, it can find itself inside a dense packed zone, or a more dilute zone, or in the freeboard of the reactor where it is carried only by the fluidising gas. The approach for the differentiation of these regimes adapted in the current study is the one described by Kolev [194] for solid particles inside a bubbly flow. The approach is based on the local volume fraction of phases and an effective fluid viscosity is calculated whenever the particle is a part of the gas-liquid (Eulerian sand) mixture.

According to Kolev [194], if bubble three-phase flow (i.e solid particles in bubbly flow) is defined, two sub-cases are distinguished. If the volume fraction of the space among the solid particles, if they were closely packed, is smaller than the liquid fraction (see fig. 3.5) (in this case the Eulerian sand) then

$$\varepsilon_s^* < \varepsilon_s, \tag{3.86}$$

where

$$\varepsilon_s^* = \frac{1 - \varepsilon_{dm}}{\varepsilon_{dm}} \varepsilon_d \tag{3.87}$$

then the theoretical possibility exists that the particles are carried only by the liquid. The hypothesis is supported if we consider the ratio of the free settling velocity in gas and liquid

$$\frac{w_{dg}}{w_{ds}} = \sqrt{\frac{\rho_d - \rho_g}{\rho_d - \rho_s} \frac{\rho_s}{\rho_g}} >> 1. \tag{3.88}$$

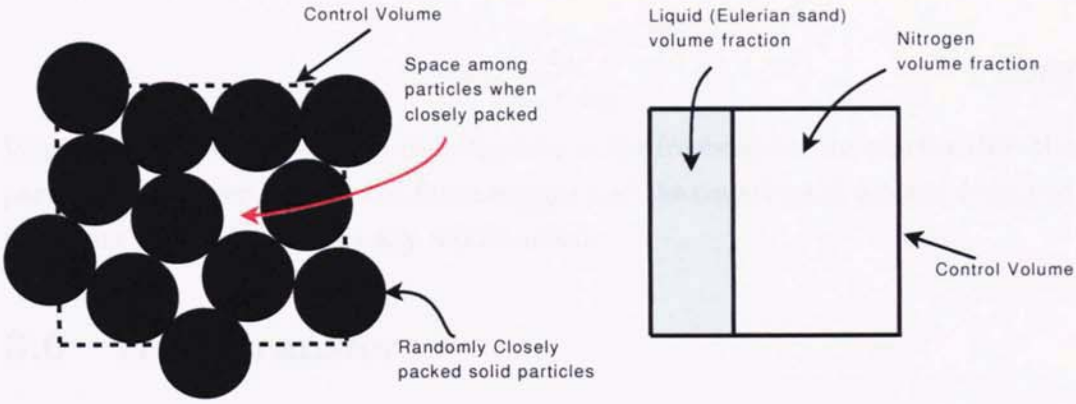

Figure 3.5: Left: Random close packing of spheres in a control volume $\varepsilon_{dm} \approx 63\%$, Right: Volume fraction of continuous phases in control volume.

Due to great differences between gas and liquid densities, the particles sink much faster in gas than in a liquid. Therefore, the drag force between gas and solid particle is zero and the drag force between solid and liquid is computed for a modified particle volume fraction ε_p

$$\varepsilon_p = \frac{\varepsilon_d}{\varepsilon_s + \varepsilon_d} \tag{3.89}$$

and an effective continuum viscosity $\mu_{eff,c}$

$$\mu_{eff,c} = \left(1 - \frac{\varepsilon_p}{\varepsilon_{dm}}\right)^{-1.55}. \tag{3.90}$$

If the volume fraction of the space among the solid particles, if they were closely packed, is larger than the liquid fraction

$$\varepsilon_s^* > \varepsilon_s, \tag{3.91}$$

then only

$$\varepsilon_{dg} = \varepsilon_d(1 - \varepsilon_s/\varepsilon_s^*) \tag{3.92}$$

are surrounded by gas and the drag force can be calculated between one single solid particle and gas as for a mixture

$$\varepsilon_p = \frac{\varepsilon_{dg}}{\varepsilon_g + \varepsilon_{dg}}. \tag{3.93}$$

When the particles are ejected from the bed to the freeboard of the reactor then the particles are carried only by the fluidising gas and the equations of motion described in section 3.4 apply without any modification.

3.6 Heat transfer

Interphase heat transfer

The most significant parameter that makes bubbling fluidised beds suitable for fast pyrolysis processes is their favourable heat transfer properties, taking into account the excellent thermal inertia of the bed as the heat capacity of solids is very large compared to that of the gases. Several correlations have been proposed for the interphase heat transfer coefficients in the literature for packed and fluidised beds [197–201]. In the current study the expression of Gunn [197] (eq. 3.94) has been used since it is valid for a wide range of solid phase volume fractions and its application on a fluidised bed is reasonable (solid phase volume fractions $0 - 60\%$)

$$\begin{aligned} Nu = \frac{h_{gs} d}{k_g} &= (7 - 10\varepsilon_g + 5\varepsilon_g^2) \\ &(1 + 0.7\mathrm{Re_s}^{0.2}\mathrm{Pr}^{1/3}) + (1.33 - 2.4\varepsilon_g + 1.2\varepsilon_g^2)\mathrm{Re_s}^{0.7}\mathrm{Pr}^{1/3}. \end{aligned} \tag{3.94}$$

Intra-particle heat transfer

The heat transported from the bed to the surface of the biomass particles is transferred by conduction toward the centre of the latter. The heat conduction along the radius of the particle is calculated by solving the heat diffusion equation for an isotropic spherical particle, taking into account the phase change phenomena due to pyrolysis, not only of the properties of the particle (thermal conductivity, specific heat capacity, density) but the internal heat generation due to the heat of reaction (ΔH) as well. The heat diffusion equation for a particle undergoing pyrolysis is given by

$$\frac{\partial}{\partial t}(\rho C_{p_{eff}} T) = \frac{1}{r^2}\frac{\partial}{\partial r}\left(k_{eff} r^2 \frac{\partial T}{\partial r}\right) + (-\Delta H)\left(-\frac{\partial \rho}{\partial t}\right). \tag{3.95}$$

The boundary condition at the surface of the particle is given by

$$h(T_\infty - T_s) = -k_{eff} \left. \frac{\partial T}{\partial r} \right|_{r=R} \tag{3.96}$$

and at the centre of the particle

$$\left. \frac{\partial T}{\partial r} \right|_{r=0} = 0. \tag{3.97}$$

Assuming that the instantaneous effective thermal conductivity k_{eff} and effective specific heat capacity $C_{p_{eff}}$ are determined only by the instantaneous presence of solids (wood and char), k_{eff} and $C_{p,eff}$ are given by

$$k_{eff} = k_C + |k_W - k_C|\psi_w \tag{3.98}$$

$$C_{p_{eff}} = C_{p_C} + |C_{p_W} - C_{p_C}|\psi_w. \tag{3.99}$$

Several correlations have been proposed in the literature for the bed-to-surface coefficient as it has already been discussed in section 2.3. The heat transfer coefficient is evaluated from the well-known Ranz-Marshall[195, 196] correlation, when the particle is carried only by the fluidising gas

$$Nu = \frac{hd_p}{k} = 2.0 + 0.6Re_d^{1/2}Pr^{1/3}. \tag{3.100}$$

However, assuming that conductive heat transfer is dominant in the near-particle-region, when the particle is inside the bed, the penetration theory can be applied with the following mixture properties [78, 86]:

$$h_{pen} = \sqrt{\frac{k_m(\rho C_p)_m}{\pi \cdot t}} \tag{3.101}$$

with

$$k_m = \varepsilon_g k_g + (1 - \varepsilon_g)k_s \tag{3.102}$$

and

$$(\rho C_p)_m = \varepsilon_g \rho_g C_{p,g} + (1 - \varepsilon_g)\rho_s C_{p,s}. \tag{3.103}$$

3.7 Reaction kinetics

The kinetic mechanism chosen to describe the pyrolytic behaviour of biomass is the two-stage semi-global mechanism illustrated in fig. 2.8 on section 2.5. The mechanism utilises Arrhenius equation (eq. 2.2) for the determination of the constants K_i, with kinetic parameters derived in the literature. Specifically, the values of the kinetic parameters were obtained by Chan et al., [202] for the primary pyrolysis products, while the fourth and fifth reactions are from Liden et al., [203] and Di Blasi [127] respectively. Table 3.3 shows the pre-exponential factors (A_i) and activation energies (E_i) used for each reaction of fig. 2.8.

Kinetic Parameters	
$A_1 = 2.8 \times 10^8 s^{-1}$	$E_1 = 140 \times 10^3 J/mol$
$A_2 = 1.3 \times 10^8 s^{-1}$	$E_2 = 133 \times 10^3 J/mol$
$A_3 = 3.2 \times 10^7 s^{-1}$	$E_3 = 121 \times 10^3 J/mol$
$A_4 = 2.6 \times 10^6 s^{-1}$	$E_4 = 108 \times 10^3 J/mol$
$A_5 = 1.0 \times 10^6 s^{-1}$	$E_5 = 108 \times 10^3 J/mol$

Table 3.3: Kinetic parameters of wood pyrolysis

The instantaneous mass balance for each one of the products is given by

$$\frac{\partial M_W}{\partial t} = -(K_1 + K_2 + K_3)M_W, \tag{3.104}$$

$$\frac{\partial M_{G1}}{\partial t} = K_1 M_W, \tag{3.105}$$

$$\frac{\partial M_T}{\partial t} = K_2 M_W - (K_4 + K_5)M_T, \tag{3.106}$$

$$\frac{\partial M_{C1}}{\partial t} = K_3 M_W, \tag{3.107}$$

$$\frac{\partial M_{G2}}{\partial t} = K_4 M_T, \tag{3.108}$$

$$\frac{\partial M_{C2}}{\partial t} = K_5 M_T. \tag{3.109}$$

In the current model, the vapours and gases are assumed to immediately leave the particle after the reaction and secondary reactions take place instantaneously, according to the local concentration of the products and not due to the flow of vapours and gases in the pores of the particle. As it will be shown later the small size of the biomass particles used ($350 - 500\mu m$) on the specific reactor makes this assumption quite reasonable. The extra-particle secondary cracking of vapours on external surfaces is not taken into account as well.

Chapter 4

Heat,momentum & mass transport

The chapter presents the results from the development of the computational model. Firstly, the computation of momentum transport from the Eulerian fluidised bed to the discrete (Lagragian) biomass particles are presented, analysing in depth the role of the basic forces exerted on the particles. Secondly, an analytical discussion of heat and mass transport in fluidised beds is presented focusing on the heat transfer from the fluidised bed to the immersed biomass particles as well as on the reaction kinetics of biomass and particle degradation and the interaction of the produced vapours with the fluidised bed. The advantages and disadvantages of the model are analytically described at the end of the chapter.

4.1 Eulerian computation of momentum transport in bubbling fluidised beds

The first attempt in the development of the computational model was to develop the code for the momentum transport from the bubbling bed of the reactor to the discrete biomass particles that are injected in it. The Eulerian approach was used to model the bubbling behaviour of the sand, which is treated as a continuum. The particle motion inside the reactor is computed using drag laws, dependent on the local volume fraction of each phase, as described on sections 3.4 and 3.5. The simulations for the momentum transport were carried out for a cold flow model, so the interphase heat transfer was not taken into account. The current section analyses the dominant forces exerted on a particle from the bubbling bed as well as the effect of the 3^{rd} dimension in the trajectory of the particle, resulting from the breaking of symmetry of the hydrodynamics of the bed.

4.1.1 Model description

This general description of the model applies for all the cases that are going to be discussed from now on with minor modifications according to the simulation problem, which are going to be mentioned.

The $150g/h$ fast pyrolysis lab scale reactor of Aston University is illustrated in fig. 4.1. Nitrogen flows through a porous plate at the bottom of the reactor at a velocity of $U_0 = 0.3m/s$. The superficial velocity is approximately 4 times greater than the minimum fluidising velocity U_{mf} of the reactor, which is typically around $0.08m/s$ using a sand bed with average particle diameter of $440\mu m$ Geldart B Group [9].

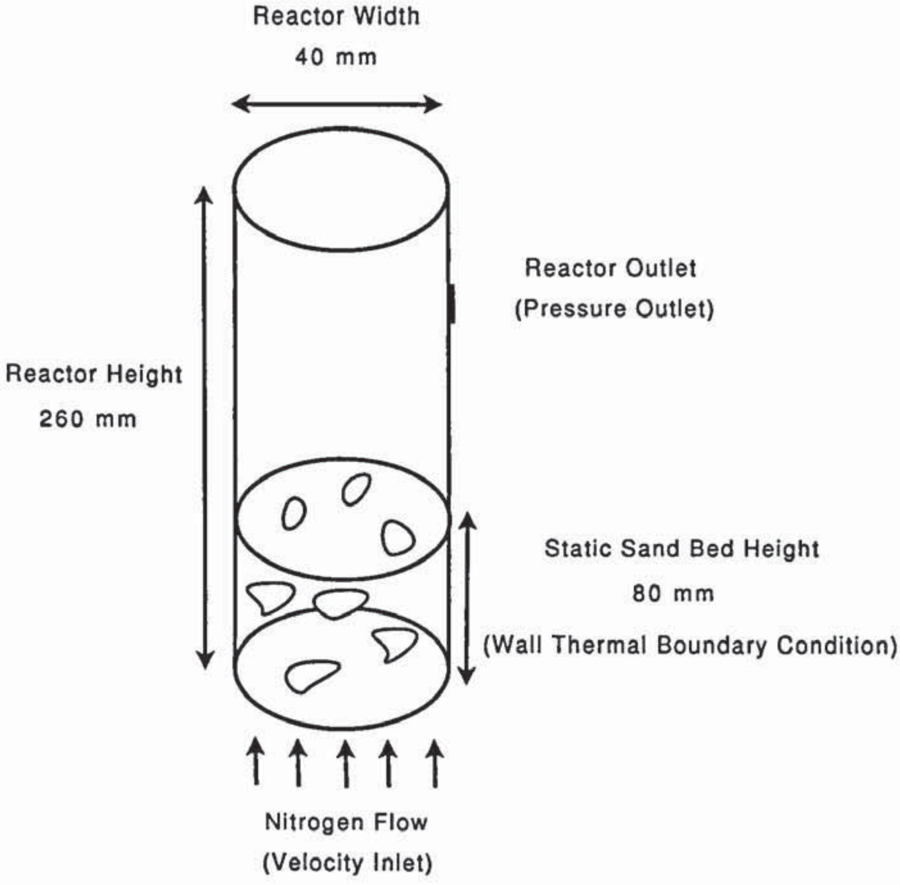

Figure 4.1: The fluidised bed reactor

The particle is injected at the centre of the sand bed which has been previously fluidised. Momentum is transferred from the bubbling bed to the biomass particle as well as from the formed bubbles inside the bed. According to Bridgwater [208], the most appropriate biomass particles sizes for liquid fuel production lie in the range of $100\mu m - 6mm$ with temperature between $700 - 800K$. The studied biomass particle is chosen to be $500\mu m$ in diameter, which is more or less the size of the particles, due to feeding problems, for a small rig like the one studied in the current study. Bigger rigs and commercial plants use larger particles in the range of $2 - 5mm$.

The scope of the simulation is to determine the correct momentum transport inside the reactor. When the particle is injected inside the reactor, it can either be inside a bubble or inside the packed bed. The code will be able to identify the regime of interest, depending on the local volume fraction of the two continuous phases, and calculate the correct drag, buoyancy and virtual mass forces according to the state. The simulations last for a representative number of seconds for fast pyrolysis and in this case the particle remained unreacted since no heat transfer from the bubbling bed was considered at this stage of the model development. 2-D and 3-D simulations were performed and the impact of each case on the particle trajectory is examined

4.1.2 2-Dimensional case

Firstly, the 2-Dimensional case has been modelled and tested. The biomass particle is injected at the centre of the bubbling bed after 1 second of fluidisation. The momentum transport from the bubbling bed and the forces exerted on the particle are modelled. Table 4.1 indicates the simulation parameters.

Property	Value	Comment
Biomass density, ρ_w	$700kg/m^3$	Wood
Biomass particle diameter, d_p	$500\mu m$	Fixed
Superficial velocity, U_0	$0.3m/s$	$\approx 4U_{mf}$
Gas density, ρ_g	$1.25kg/m^3$	Nitrogen
Gas viscosity, μ_g	$1.79 \times 10^{-5}kg/ms$	Nitrogen
Solids particle density, ρ_s	$2500kg/m^3$	Sand
Mean solids particle diameter, d_s	$440\mu m$	Uniform distribution
Restitution coefficient, e_{ss}	0.9	Value in literature
Initial solids packing, ε_s	0.63	Fixed value
Static bed height	$0.08m$	Fixed value
Bed width	$0.04m$	Fixed value

Table 4.1: Simulation Parameters

Figure 4.2 illustrates the hydrodynamics of the fluidised bed at different simulation times with the particle position indicated by the black spot inside the contours. Until the 1^{st} second of the simulation the bed is fluidised without the biomass particle injected in it. Since the sand has gained some velocity in the x and y direction, the biomass particle is injected and momentum is transferred from the fluidised sand to the particle. The velocity of the particle is calculated and its new position is illustrated by the black spot inside the reactor.

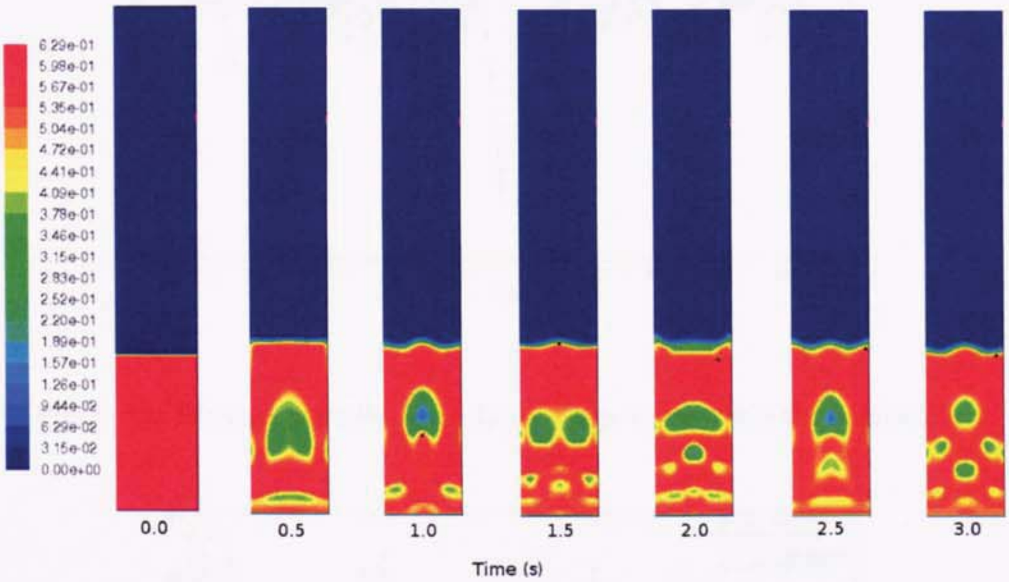

Figure 4.2: Fluidised bed hydrodynamics with biomass particle position

The particle's velocity in the x and y direction is calculated by adding eqs. 3.76 and 3.77 and its instantaneous values are shown in figure 4.3. The velocity components are highly dependent on the local velocity of the Eulerian solid phase (sand) and nitrogen. Depending on the regime of interest, since the local volume fraction of the two Eulerian phases define the drag, buoyancy and virtual mass force, the particle's velocity is computed. The local volume fraction of sand and nitrogen as well as the local **x** and **y** velocity components of sand and nitrogen are shown in figures 4.4, 4.5, 4.6 respectively.

By examining the plots of the particle velocity, the local velocities of sand and nitrogen in figures 4.5, 4.6 and the equations that describe the drag and virtual mass force (1^{st} term of eq. 3.76, and eq. 3.77) one can immediately picture the way these forces are going to act on the particle. The drag force is a function proportional to the velocity difference between the particle and the carrier fluid, while the virtual

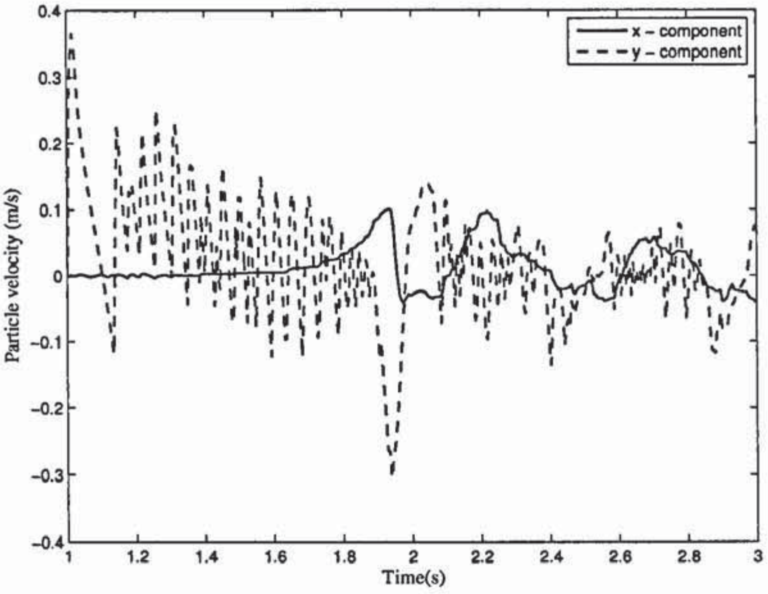

Figure 4.3: Biomass particle x - y velocity components inside the fluidised bed

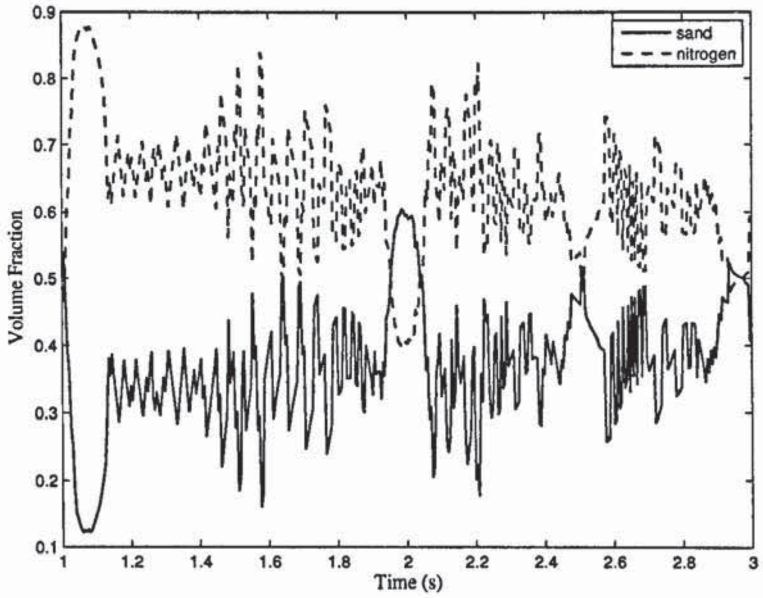

Figure 4.4: Sand and nitrogen local volume fraction

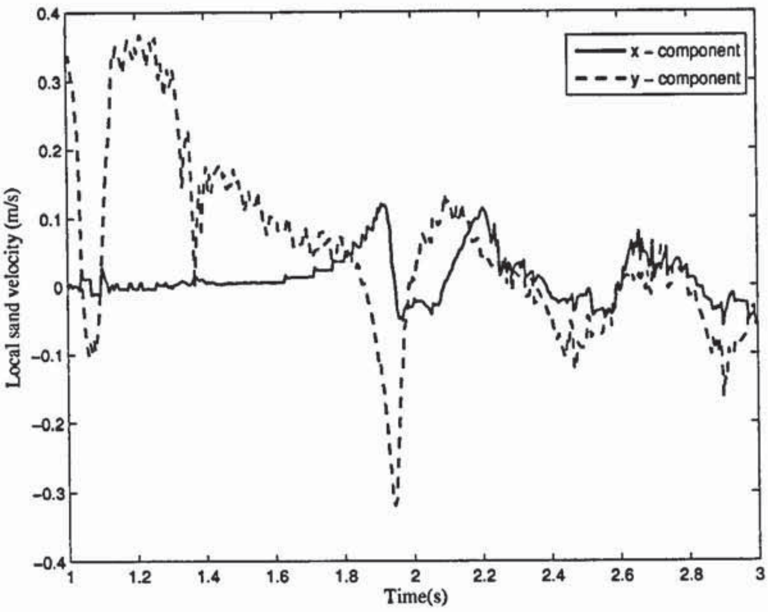

Figure 4.5: Local sand x - y velocity components

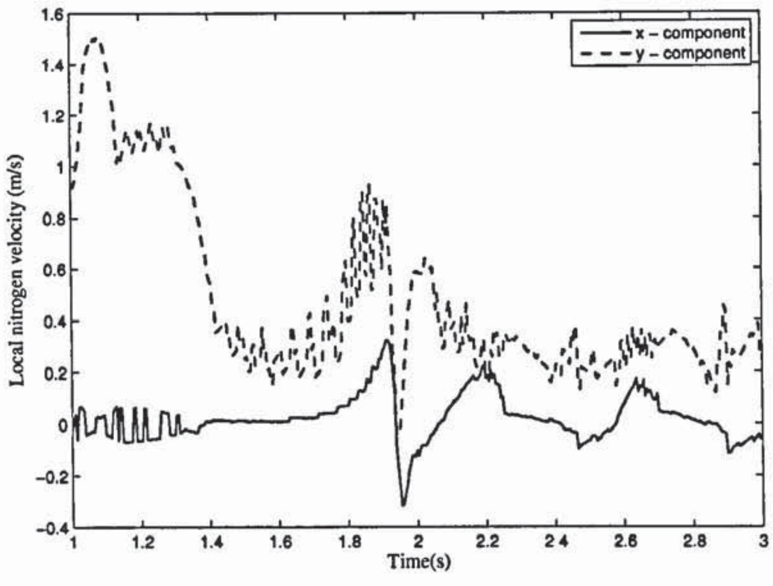

Figure 4.6: Local nitrogen x - y velocity components

mass force is dependent on the velocity gradients of the particle and the carrier fluid. Thus, whenever sudden slopes occur on the velocity plots , higher amounts of forces are expected. The plots of the drag force and virtual mass components are shown in figures 4.7, 4.8.

In fig. 4.7 we can see the big differences in the amount of drag produced in the two directions (x - y) as well as the great differences as the particle changes positions inside the reactor and therefore the regime of interest. The big amounts of drag force produced are caused when the particle finds itself in excess of sand and it is mainly carried out by the latter, while when the particle is inside a bubble the drag force reduces significantly. The drag force diagram is a good indicator of the position and the region of the bed that the particle is inside. As we can see the drag force in the y - direction is much greater than the x - direction since the sand and nitrogen velocities in the x - direction are much lower than in the y - direction. However, this small amount of drag produced in the x - direction is mainly responsible for the increase on the biomass particle's x - velocity in the positive direction and therefore the particle finds itself at the right hand side (positive) of the reactor at the end of the simulations.

Fig. 4.8 illustrates the virtual mass force developed during the motion of the

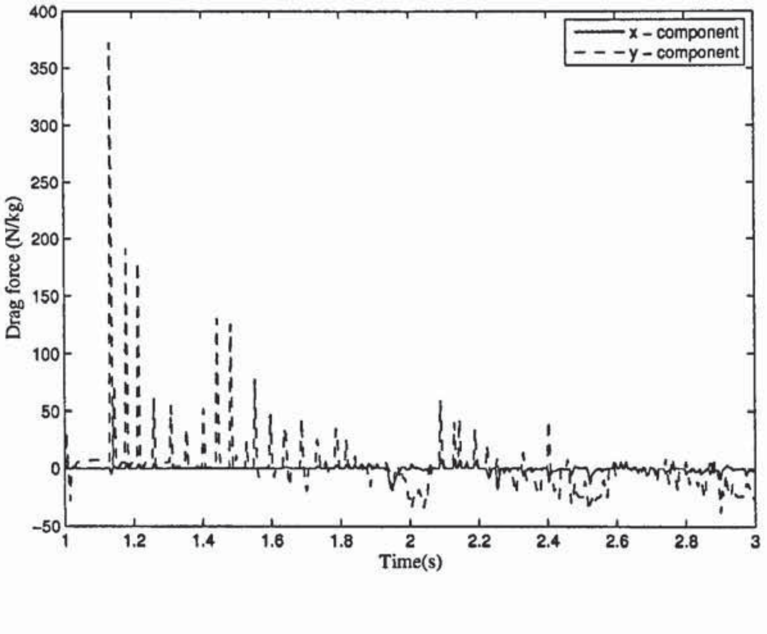

Figure 4.7: Drag force per unit mass, x - y components

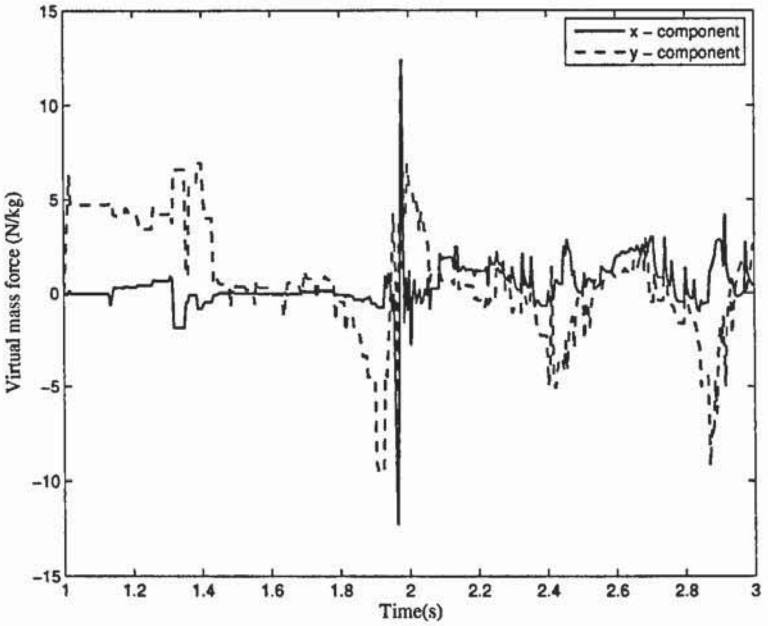

Figure 4.8: Virtual mass force per unit mass, x - y components

particle. There are mainly 3 regions of interest. At the injection of the particle a relatively big amount of virtual mass force is produced due to the high gradients in the velocities of the two fluids. Close to 2 seconds a big "*spike*" mainly in the x but also in the y - direction seems to occur. By examining the graphs of the local sand and nitrogen velocities one can easily understand how that occurred. Close to 2 seconds a high velocity gradient seems to occur in the x and y - direction of the particle, sand and nitrogen velocities. Therefore, by corresponding the velocities graphs to the virtual mass equation (eq. 3.77) the big fluctuation of the virtual mass force is explained. We also have to notice that when the particle finds itself inside a low sand concentration zone the virtual mass force tends to zero due to the great difference between the biomass particle and nitrogen gas densities. Therefore, the virtual mass is important only when the density of the carrier fluid is greater than the discrete particle's density.

The particle remains inside the reactor at the end of the simulation because the drag force exerted on the particle from nitrogen, is not high enough to carry out of the reactor an non-reacting particle of density $700kg/m^3$ and diameter of $0.05 \times 10^{-2}m$. The terminal velocity of such a particle can be computed and it is approximately $\approx 1.6m/s$. We can see in fig. 4.6 that the local velocity of nitrogen tends to approach this value only at the beginning of the injection of the particle and nowhere else. However, when a particle is pyrolysed and its density reduces significantly the nitrogen velocity is usually high enough to exert the required drag force on the particle and hence lead it out of the reactor efficiently.

4.1.3 3-Dimensional case

A 3-Dimensional case has also been modelled and tested and the results were compared with the 2-Dimensional one. Again, the biomass particle is injected at the centre of the bubbling bed after 1 second of fluidisation and the momentum transport from the bubbling sand and the forces exerted on the particle are evaluated. The simulation parameters are the same as the ones described in table 4.1.

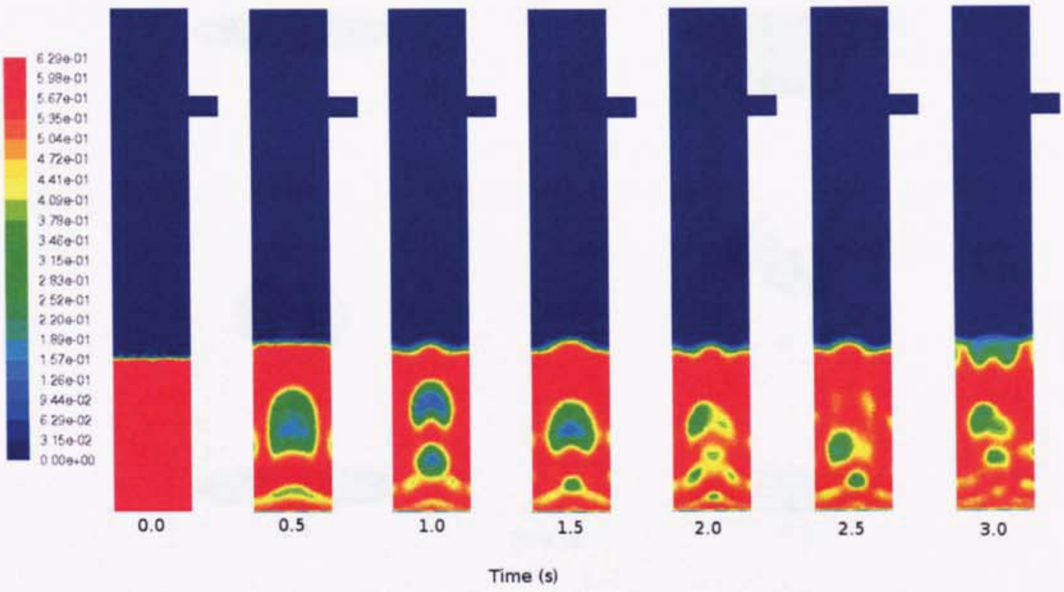

Figure 4.9: Fluidised bed hydrodynamics on a slice at the centre of the 3-D reactor

Figure 4.9 illustrates the hydrodynamics of the fluidised bed on a slice at the centre of the 3-D reactor at different simulation times, so the differences with the hydrodynamics of the 2-D simulation can be visible. Figure 4.10 shows the bubble formation (isosurface of nitrogen volume fraction of 0.7) and the particle position relative to them.

We can observe that the hydrodynamics of the bed in the 2-D and 3-D case are

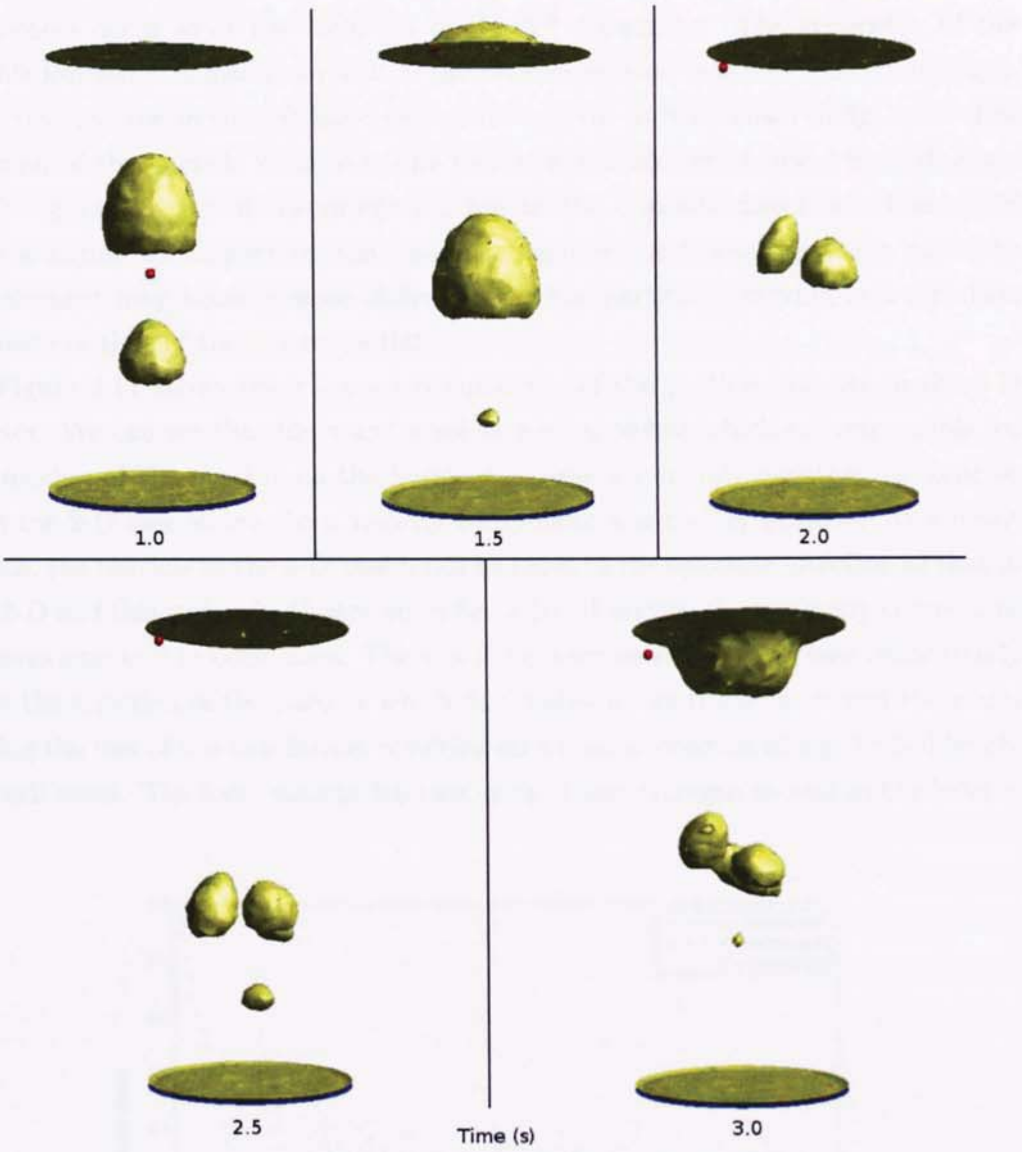

Figure 4.10: Isosurfaces of bubbles (nitrogen volume fraction 0.7) in the fluidised bed with relative particle position

slightly different. In the 3-D simulation the bed does not behave as symmetrically as the 2-D. The bubbles are formed in a more random pattern and consequently the particle motion is affected. Figure 4.10 clearly shows in a 3-D illustration how the bubbles shown in fig. 4.9 have been formed. However, the bed expansion is similar to both cases. The comparison between the 2 cases shows that considerable differences occur after the inclusion of the 3^{rd} dimension. The symmetry of the bubble formation is lost as a result of the sand expansion in the z - axis, resulting in a particle motion in the left hand side of the reactor as it is shown in fig. 4.10. The position of the particle relative to the bed height is almost identical in both cases at the specific times of the simulation but in the opposite direction. This could have a significant impact on the residence time of the biomass particle since the entrainment may become more difficult when the particle is moving in a direction opposite of that of the reactor outlet.

Figure 4.11 shows the x - y - z components of the particle velocity in the 3-D reactor. We can see that the x and z velocity components which are responsible for the motion of the particle on the horizontal plane are mainly negative, in contrast with the 2-D case where the x velocity component was mainly positive. As a result of this, the particle in the 3-D case tends to move in the opposite direction of that in the 2-D and this is clearly illustrated in fig. 4.10. However, the y velocity component behaves similarly in both cases. There is a big positive velocity increase immediately after the injection of the particle which diminishes to fluctuations around the x axis during the rest of the simulation, resulting on a similar position along the bed height in both cases. The local volume fraction of sand and nitrogen as well as the local x,

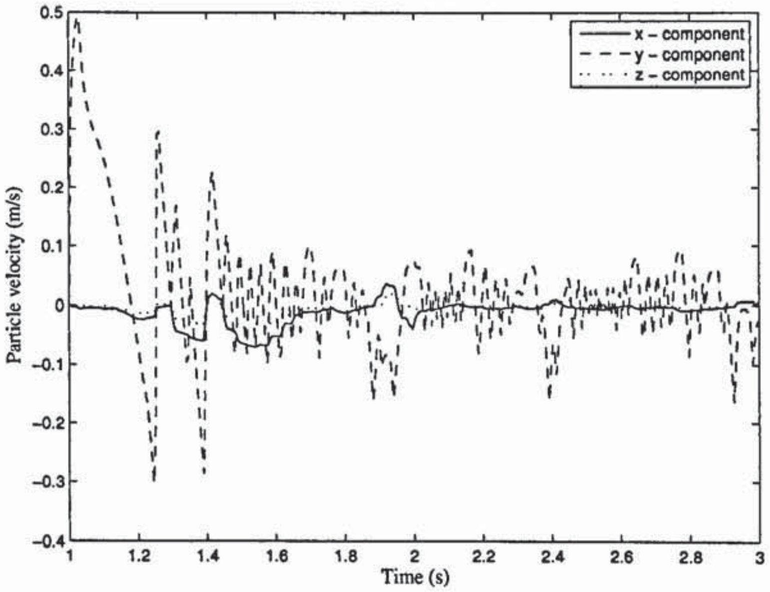

Figure 4.11: Biomass particle x - y - z velocity components inside the fluidised bed

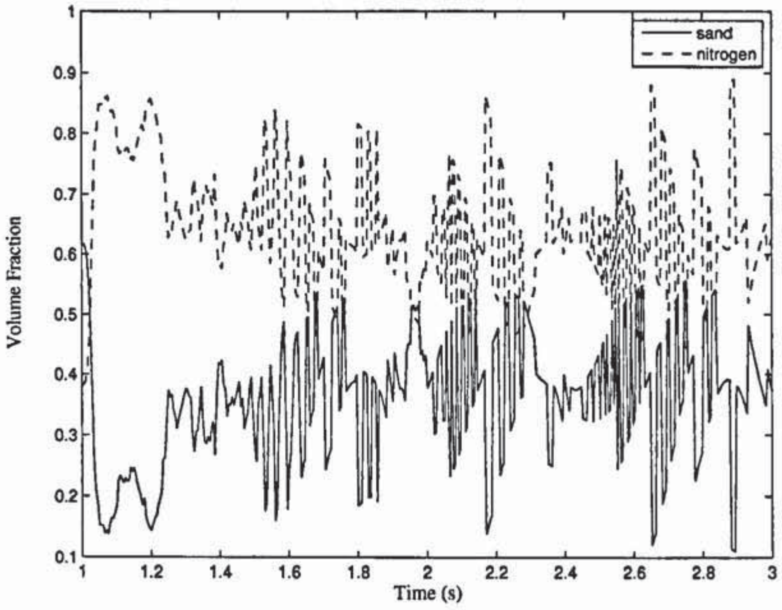

Figure 4.12: 3-D sand and nitrogen local volume fraction

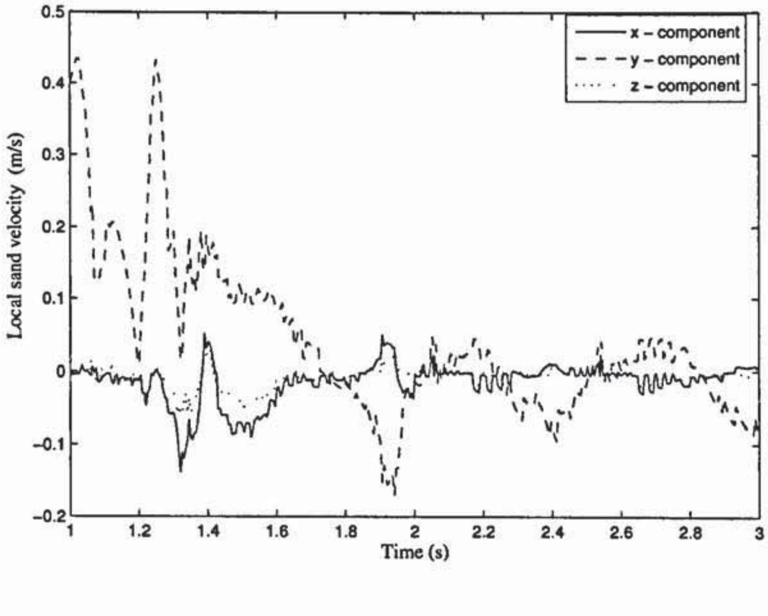

Figure 4.13: Local sand x - y - z velocity components

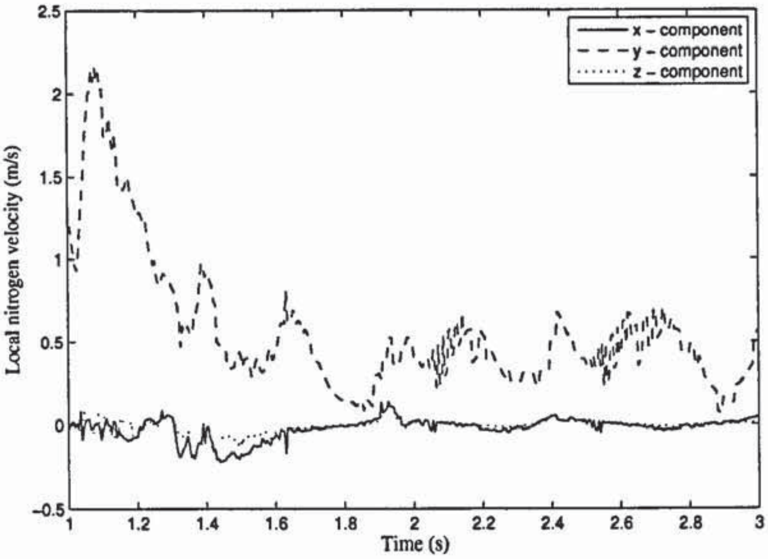

Figure 4.14: Local nitrogen x - y - z velocity components

y and z velocity components of sand and nitrogen are shown in figures 4.12, 4.13, 4.14 respectively.

By observing the graphs of local volume fraction, sand and nitrogen velocities, we can conclude that the particle in the 3-D case, spends most of its time during its motion, in low sand concentration areas of the bed and thus having as a result, lower drag force produced. In the 2-D case, during the first 0.5 seconds of the particle's motion, it seems that the sand concentration is higher close to the feeding point and thus the higher number of "*spikes*" in the y-direction of drag force plot (fig. 4.15) which indicates greater drag. In the first 0.3 seconds of the 3-D case the particle is moving in a low sand concentration area (low drag force), where suddenly enters a high concentration zone and a sudden increase in the y-direction drag force component is observed. As a general behaviour, by examining the figures 4.7,4.15 of the 2-D and 3-D cases respectively, many similarities are observed, resulting to the similar behaviour of the particle in both cases. However, the x and z-component of the drag force tend to be negative in the 3-D case, thus pushing the particle to the left hand side of the reactor.

Considerable differences can be noticed in the virtual mass force diagrams of the two cases. Despite the fact that the maximum values of the virtual mass force are almost the same in both cases figs. 4.8, 4.16 show that the peaks of the force occur

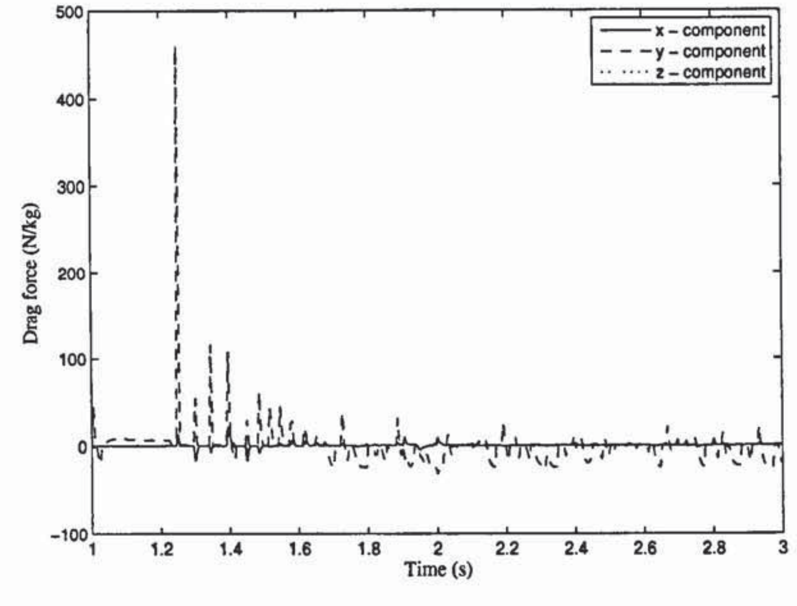

Figure 4.15: Drag force per unit mass, x - y - z components

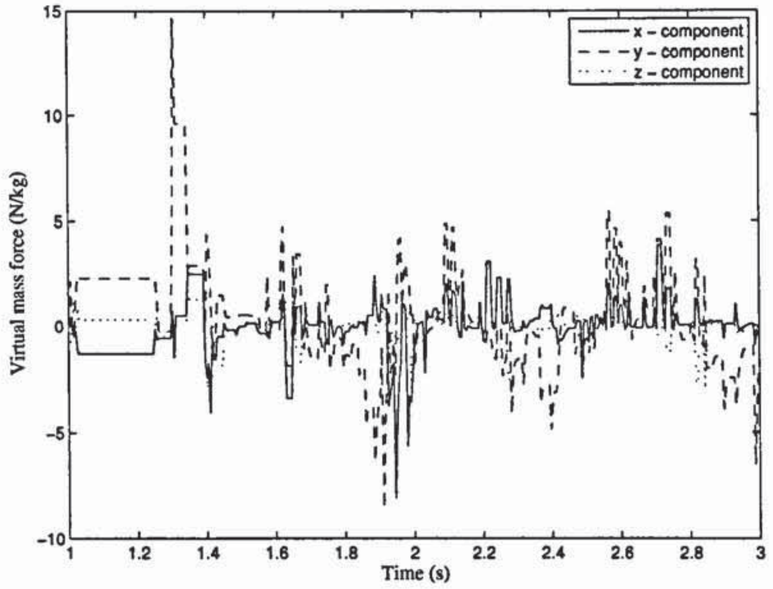

Figure 4.16: Virtual mass force per unit mass, x - y - z components

at different instances and have a slightly different pattern. This can be explained by the fact that the bubbles seem to be formed in a different pattern in the 3-D case, so the particle ends up at a region of different sand concentration with different velocity gradient. This information can also be extracted from the plots of local sand, nitrogen and particle velocities (Figs. 4.11, 4.13, 4.14).

By comparing the drag and virtual mass force diagram for both cases we can clearly see that the major factor that influences the particle motion is the drag force generated by the carrier fluid in each case. The magnitude of the virtual mass force becomes significant when the velocity of the carrier fluid is relatively small and only when its density is greater than the discrete particle's density. For instance, when the particle finds itself in a region of low sand concentration (period of 0.2 seconds after the injection) there is a great increase in nitrogen velocity (big velocity gradient), which gets over $2m/s$ and still the fluid produces only $2N/kg$ of virtual mass force. At 0.3 seconds the particle has progressed to a higher sand concentration zone, where the latter accelerates to $0.4m/s$. The virtual mass force produced at this point has reached almost $15N/kg$ despite the fact that the carrier fluid (at this instance the Eulerian sand) accelerates slower to a much lower velocity. However, while the virtual mass force at its peak can reach $15N/kg$ the drag force at the same instance produces almost $480N/kg$. Virtual mass force plays an important role either when the particle finds itself in a low sand concentration or the carrier fluid velocity components accelerate in a low magnitude region.

4.1.4 Conclusions

The studied fluidised bed comprises of solid sand grains which are fluidised from a gas to result in a fluid-like behaviour. Therefore, momentum is transported in fluidised beds by collisions of sand grains with biomass particles together with the drag produced by the continuous phase (gas). The averaged approach (Eulerian-Eulerian) adopted for the behaviour of the sand, led to the representation of the collisional forces between the solid particles with drag functions associated with the fluid-like behaviour of the sand.

However, modelling of forces on particles inside a fluid flow is not an easy task. Steady and unsteady forces act on the particles due to the relative motion of fluids as well as rotational effects. In this study, the forces considered to act on the particle are the steady-state drag, the pressure gradient, buoyancy force and the virtual mass force. Rotational effects of the particle have not been considered, so lift forces

(Saffman force, Magnus force) were assumed not to play a significant role. Also, the limitations of FLUENT that does not give access to flow variables on neighboring computational cells to the user led to this assumption. The torque on a discrete particle is a function of the curl of the velocity field and requires the discretisation of spatial derivatives. Also, sphericity effects were not considered at this stage since the particle was assumed to be totally spherical.

A complete Eulerian approach on momentum transport in fluidised beds should include all the possible effects of particle motion. The dominant force however is the drag force induced by the carrier phase and simplifications of the equations can be made for computational convenience.

It was also shown that the geometrical approach of the problem results in different simulation observations. The hydrodynamics of the bed changed significantly from the 2-D to 3-D case. It was shown that in the 3-D case a bubble was formed close to the feeding point of the reactor and the drag force was quite reduced at the injection time compared with the 2-D case. It is intelligible that due to computational power limitations 2-D simulations are generally preferred (fluidised bed hydrodynamics) for research purposes, however when heat, mass and momentum transport is considered the 3-D approach looks the most appropriate and promising one.

From a computational point of view, the model extends a state of the art commercial CFD software, to fully simulate a multiphase flow process involving momentum transport from a bubbling state. The user defined code development however is extensive and demands correct access to FLUENT's computational cells and threads after the separation of the computational domain. This is usually the major source for computational errors, so UDF coding has to be fully understood and clarified by the programmer.

4.2 Eulerian computation of heat & mass transport in bubbling fluidised beds

After the completion of the momentum transport model for discrete particles inside a fluidised bed, the research focused on the development of the code for the determination of the bed-to-surface heat transfer, as well as the incorporation of chemical kinetics in the main code structure and its association with the discrete particles. Assuming that conductive heat transfer is dominant in the near particle region when the particle finds itself in the dense packed regime the correlation of Mickley and Fairbanks [78] (eq. 3.101) was used for the calculation of the heat transfer coefficient, while the Ranz-Marshall [195, 196] correlation was used for the case that the particle is in the freeboard of the reactor. The chemical kinetics of biomass were based on a two-stage, semi-global mechanism as it is shown on fig. 2.8, with kinetic constants given in table 3.3. The simulation parameters are the same as the ones mentioned on table 4.1, except that this time the density of nitrogen was taken as $\rho_g = 0.456 kg/m^3$, and nitrogen viscosity as $\mu_g = 3.44 \times 10^{-5} kg/ms$, values that correspond to the fluid properties at $773K$. The sand bed is assumed to be at a uniform temperature of $773K$.

4.2.1 Bed hydrodynamics and position of particle

Figure 4.17 illustrates the hydrodynamics of the fluidised bed at different simulation times with the particle position indicated by the black spot inside the contours. Until the 1^{st} second of the simulation the bed is fluidised without the biomass particle injected in it. Since the sand has gained some velocity in the x and y direction, the biomass particle is injected and momentum is transferred from the fluidised sand to the particle. The velocity of the particle is calculated by integrating in time the

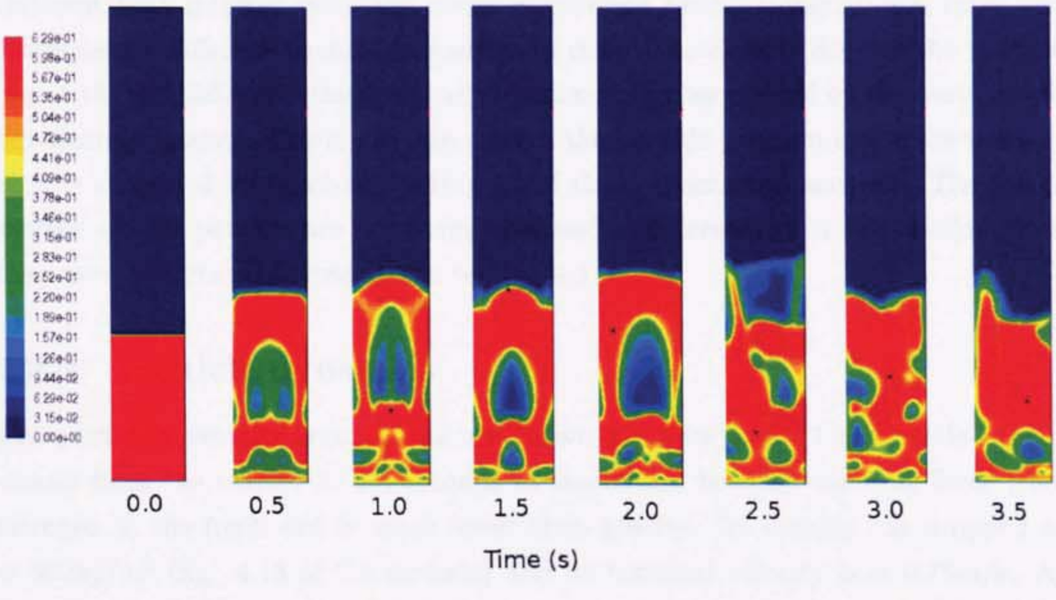

Figure 4.17: Fluidised bed hydrodynamics with biomass particle position

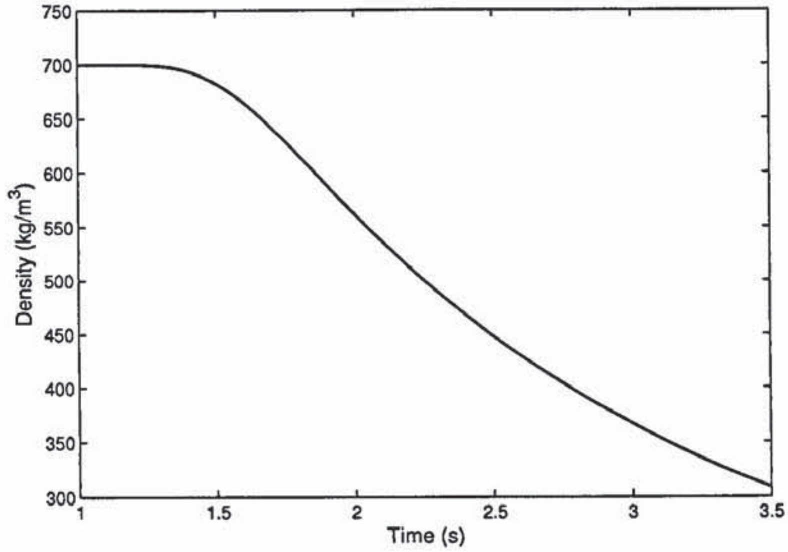

Figure 4.18: Average particle density

equation of motion for discrete particles (eqs 3.76 and 3.77), and its new position is illustrated by the black spot inside the reactor. The particle's position in the reactor is a result of the heat transfer and phase change due to reaction effects. Different heat transfer rates will result in different biomass degradation rates and consequently different particle properties in time. The density drop of the particle (fig. 4.18) will differ and the drag and virtual mass forces exerted on the particle will significantly change. The model can predict the particle position inside the reactor, as it is subjected to pyrolysis, taking all of these effects into account. The forces exerted on the particle are not being analysed and presented in this section since they were analytically presented in section 4.1.

4.2.2 Particle dynamics

The particle's velocity components are shown in figure 4.19. The particle cannot escape from the reactor in 2.5 seconds of simulation because the drag force from nitrogen in the freeboard is much lower than gravity. Its density has dropped to $\approx 300kg/m^3$ (fig. 4.18 at 2.5 seconds) and its terminal velocity is $\approx 0.75m/s$. As fig. 4.20 shows, the average y-velocity component of nitrogen on the freeboard of the reactor ranges from $0.4 - 0.5m/s$. This means that nitrogen cannot provide the necessary drag to carry out of the reactor the pyrolysed particle and further

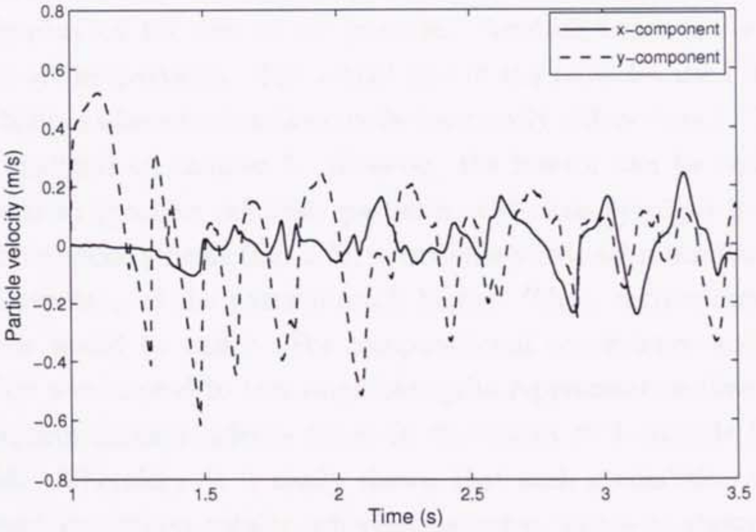

Figure 4.19: Particle velocity components

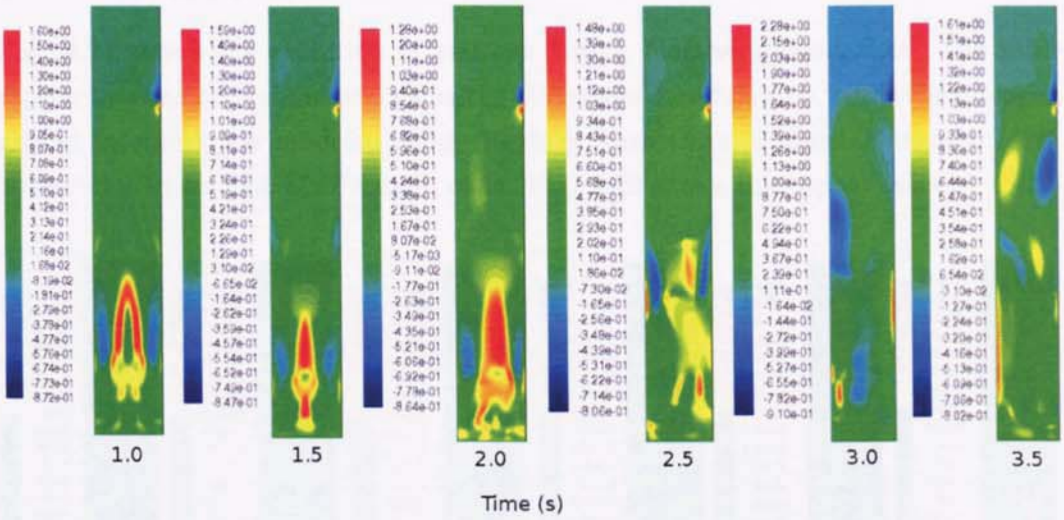

Figure 4.20: Contours of y-velocity component of nitrogen

degradation is necessary to reduce its density to the required levels. This of course increases the residence time of the char particle inside the reactor which has a catalytic effect on vapour yields and favours further char and gas formation.

However, the assumption that the particle retains its initial volume is crucial.

Shrinkage usually occurs during pyrolysis as well as char attrition would have a significant impact on the size of the particle. Another factor is the size as well as the shape of the particles. The actual size of the particles used in the reactor approaches $350\mu m$ where their sphericity factor greatly differs from 1. These aspects are further analysed on chapter 5. However, the reactor can be easily and more efficiently used to pyrolyse cellulosic particles. Cellulose pyrolysis is described by the Broido-Shafizadeh scheme (fig. 2.7), where char yields are much lower ($\approx 4-5\%$) and the density drop of the particle much higher. Thus, entrainment of char out of the reactor would be easier. For computational convenience and time saving the simulation was limited to this small but quite representative time period. Fast pyrolysis requires small residence times in the range of 2 seconds for maximum vapour yields. Therefore, it is easily shown that such a condition would not be easily achieved for $500\mu m$ totally spherical particles, where as shown the particle residence time will greatly exceed the required limit.

4.2.3 Evolution of volatiles

Fig. 4.21 shows the evolution of vapours during biomass degradation. The sand-vapour interaction is simulated using the Gidaspow drag function, while the nitrogen-vapour interaction is modeled using the drag correlation of Morsi-Alexander [176], both included on FLUENT's main code. Fig. 4.22 shows the vapour velocity distri-

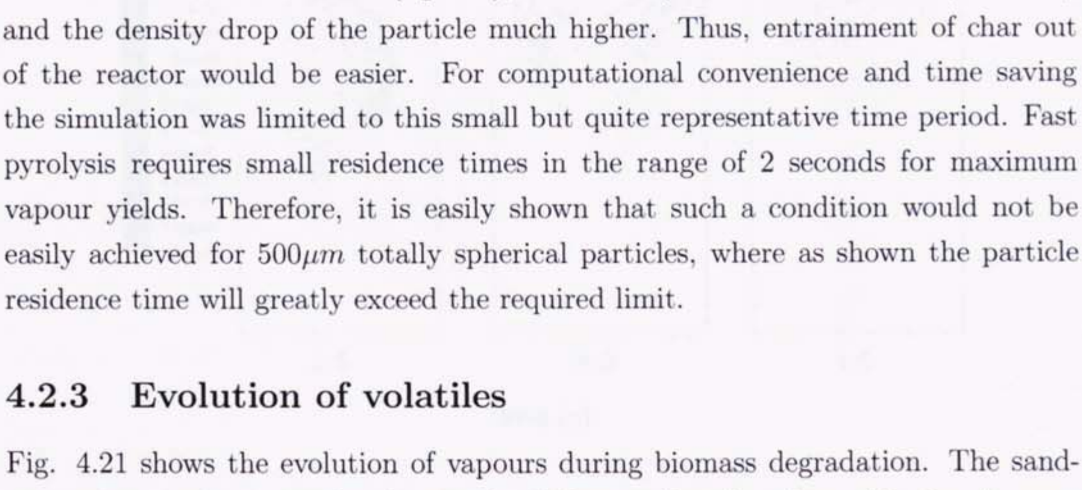

Figure 4.21: Volume fraction of vapours

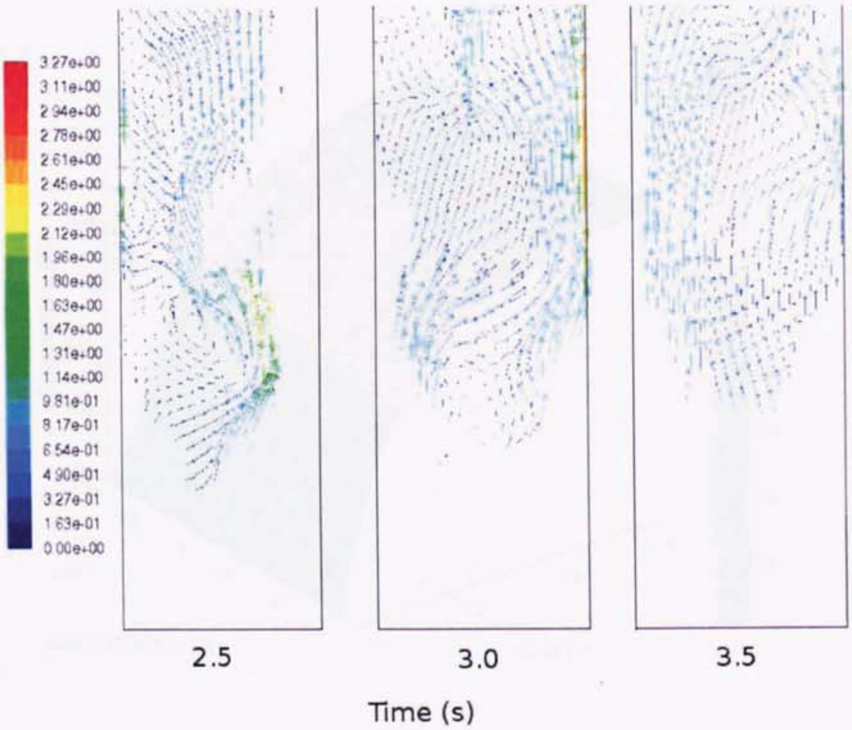

Figure 4.22: Vectors of velocity magnitude of vapour inside the bed

bution inside the bed. Modelling the flow of the evolved vapours one can determine its residence time, which is a significant factor regarding the final bio-oil yield since vapours are catalyzed by char, reducing bio-oil conversion efficiency. In relation to biomass particle dynamics, the model can provide a good guide for reactor design especially on the aspect of char-volatiles interaction. In this specific case, we can notice that after 1 second of the injection of biomass the vapours have reached the outlet of the reactor. Considering that the normal vapour residence time for maximum yields is close to 2 seconds, the simulation shows that the reactor is capable of producing this desirable effect.

4.2.4 Heat transfer

The radial temperature distribution is shown in figure 4.23. The surface plot shows the different temperature profiles inside the particle for different times during pyrolysis. The particle reaches the reactor temperature in ≈ 0.6 seconds and the exothermic nature of the reaction makes the internal points of the particle to reach

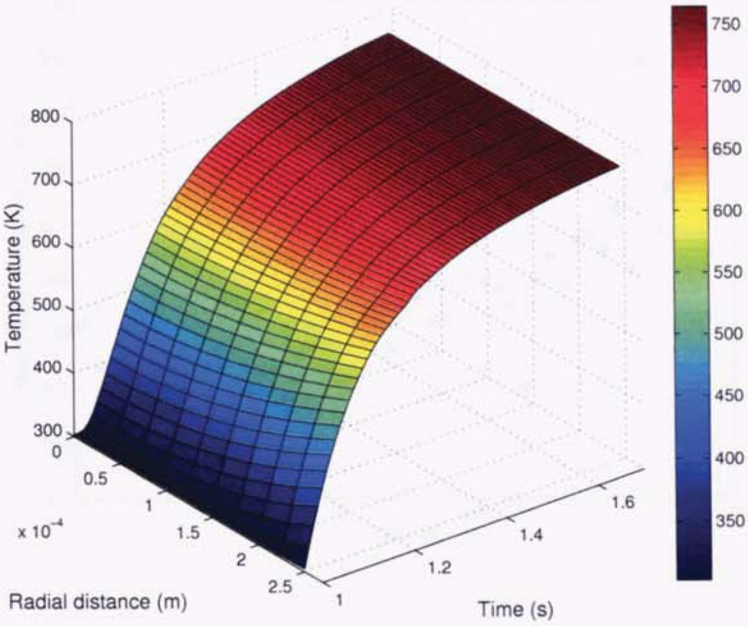

Figure 4.23: Radial temperature distribution

a slightly higher temperature than that of the reactor. However, this raise in temperature is in the order of $0.5 - 2K$ and it cannot be easily noticed in fig. 4.23. Therefore, it can be considered insignificant and does not affect the product yields.

The heat transfer coefficient (fig. 4.24) ranges from $190 - 475W/m^2K$ (average of $\approx 350W/m^2K$) which is a typical range for fluidised bed reactors of Geldart B group particles [209]. The model takes into account the degradation of the particle in the calculation of the convective and conductive heat transfer in each time-step. Due to phase change phenomena the properties of the particle change and the heat transferred is significantly affected as it is indicated in eqs. 3.95 and 3.96. The radial temperature profile however seems to be relatively flat. This is due to the small biomass particle size which for an average heat transfer coefficient of $h \approx 350W/m^2K$ has a *Biot* number of $Bi \approx 0.28$. This results in almost radially uniform product yields as it is shown on the surface plots of figure 4.25. The fact that conduction acts faster than convection makes the internal points of the particle reach the surface temperature very quickly. Also, the fact that biomass degradation starts at about 400^oC makes the temperature gradient which is more intense in the

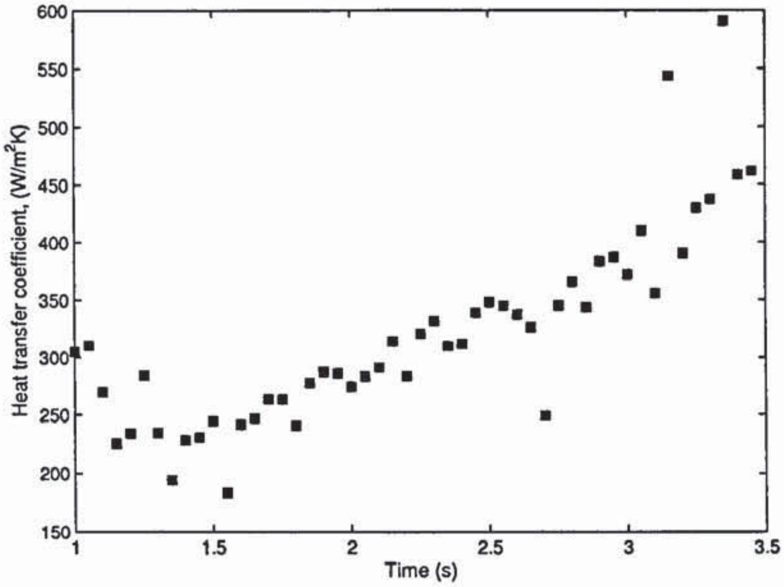

Figure 4.24: Local heat transfer coefficient

intermediate temperatures and favour char formation, to be relatively insignificant in the degradation of the particle in the case of fast pyrolysis. Therefore, for a small particle like the one studied in this case, where the temperature gradient at the initiation of the reaction is not significant, the assumption that the particle maintains a uniform temperature can be considered to be valid even when $Bi > 0.1$. As shown in fig. 4.23 the particle has reached an almost uniform temperature, so the product distribution is radially uniform. The case of course would not be the same if a larger diameter particle was examined, where the *Biot* number is greater and the temperature gradient more significant. The UDF can be used to model such a case and gives the opportunity to the user to define the number of nodal points along the radius of the particle, something that makes the user to have a complete control over the required time-step for algorithm convergence.

4.2.5 Product yields

The simulation time of the particle is 2.5 seconds but we can still see $\approx 30\%$ of wood unreacted (fig. 4.25). The reason for simulating 2.5 seconds is because usual residence times for fast pyrolysis are close to 2 seconds. The particle needs almost 0.6 seconds to reach the reactor temperature, so the particle is pyrolysed for almost

2 seconds. Also, the computational needs and outputs, led to this limited, but quite representative time of simulation. The final vapour yield reached $\approx 45\%$ by weight of wood, while the gases $\approx 10\%$ and char $\approx 15\%$ respectively. The reason for the relatively increased char formation and decreased vapour production in the 70% of the wood that has reacted is the 0.6 seconds that the particle needs to be heated up to $773K$. At the early stages of the biomass injection the particle spends more than half a second in intermediate temperatures $(303-700K)$ which favour the formation of char. In a process that lasts around to 2 seconds, this transitional stage from atmospheric to reactor temperature can significantly affect the final bio-oil yields.

Typical fast pyrolysis yields on dry wood basis would recommend vapour yields of $\approx 75\%$. However, the reaction kinetics scheme takes into account intra-particle vapour cracking catalyzed by char, which contributes to the higher amount of char and gas products. Also, complete degradation of the particle would result to higher amount of vapour yields. According to [138] the same reaction kinetics scheme, without taking into account the secondary reactions, would produce yields of $\approx 23\%$

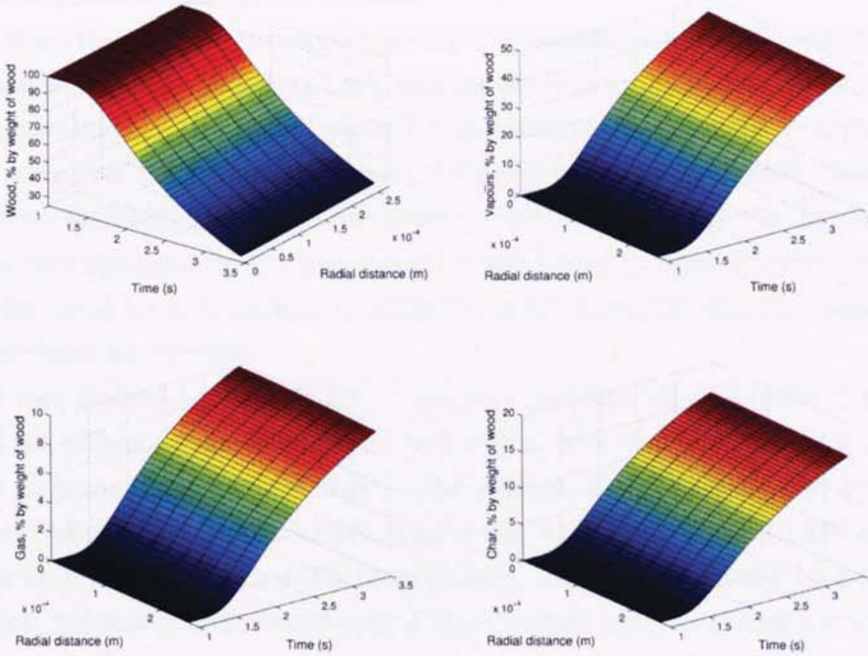

Figure 4.25: Product yields

char, $\approx 13\%$ gas and $\approx 64\%$ vapours, for complete (100%) biomass degradation at $773K$. Therefore, the yields produced in the simulation are pretty similar with those produced by the single particle models in the literature, since complete degradation of the particle would result to almost identical yields percentages. This indicates the correct implementation of the reaction kinetics in the UDF associated with the discrete particle.

4.2.6 Model advantages and drawbacks

A complete fast pyrolysis model in bubbling fluidised bed reactors would have certain advantages over single particle models especially on the direction of reactor design.

Simulating the complete process of fast pyrolysis, one can have a realistic view of what is happening inside the reactor. Reactor designs can be optimised for efficient char entrainment, something that would increase bio-oil yields. Vapours are catalyzed by char, lowering bio-oil yield efficiency. Bed hydrodynamics can be simulated for different reactor geometries and its effect on the heat transfer coefficient and biomass degradation can be quantified. Possible effects of the products to the bed hydrodynamics can also be noticed.

However, the computational cost of such a simulation is high. The extensive code development and the extremely high amount of memory allocation slows down the simulations significantly. Especially in 3-dimensional cases the mass, momentum and energy sources of a 3^{rd} Eulerian phase (in this case the vapours) would make things even worse. Combining these factors together with the fact that the tiny amount of mass source released from the particle at the early stages of pyrolysis and makes the simulation need more iterations to achieve convergence, the computational delays can sometimes be extreme.

The user defined function (UDF) contains numerical algorithms for the solution of the heat diffusion equation inside the particle. The code uses the flow time-step for the time marching of heat flux at the surface of the particle and conduction along its radius. Both flow solution (performed by FLUENT) and UDF algorithm solution have to converge in a synchronous way. This sometimes can be a reason for significant reduction of the time-step if the Courant number is high, which means high computational delays in the general solution of the flow field due to small time-steps.

Post-processing of the UDF output file can also be a problem. Using small time-steps (in the order of $10^{-4}-10^{-5}$) results in large output files with thousands of data, for simulations in the order of seconds. However, such a situation can be relatively easily resolved by including small *"data-save"* loops, specifying the number of time-steps to save.

4.2.7 Conclusions

Sections 4.1 and 4.2 have described the basic results and procedure followed to develop a complete fast pyrolysis model of biomass in bubbling fluidised bed reactor. Several useful observations were made and conclusions were derived.

Modelling of multiphase flows combined with discrete particle tracking can be possible by incorporating external a User-defined function in a commercial CFD software. FLUENT 6.2 was used as the modelling framework for the simulation with an extensive computational sub-routine to account for the heat and momentum transport from the fluidised bed to the biomass particle, as well as the prediction of the radial distribution of temperature and product yields. This was done by associating reaction kinetics of biomass with the properties of the moving discrete biomass particle.

It was found that the model can predict the residence time of vapours and biomass particle. The properties of the pyrolysing particle can be predicted since the model accounts for its degradation which has an immediate effect on its trajectory inside the reactor. The model can be a useful guide for reactor design where char entrainment is of major importance. It can be easily modified and simplified for computational convenience if all the information of biomass pyrolysis is not needed (i.e not to include evolution of vapours if only char formation and entrainment is necessary etc.). It can be also applied to different processes such as combustion or gasification by simple modifications on the structure of the computational code.

The range of applications of such model is very large. It can be used very simply as a reactor design guide taking into account many parameters by single modifications of the external computational code. Optimum feedstock particle sizes and shapes can be determined for efficient fast pyrolysis as well as char entrainment. Geometrical modifications can be easily made taking into account not only the hydrodynamics of the bed as it is used to be by the majority of the fluidised bed hydrodynamic models, but also how the geometry of the reactor will affect the reacting biomass particles in terms of momentum and heat transfer as well as the residence times of the pyrolysis vapours. This observation can be also applied to scaling of reactors since the hydrodynamic similarity is not the only factor that defines the efficiency of a process. The effect of biomass shrinkage on the product yields as well as on the dynamics of the discrete particles can be treated in a different way than it used to be on the single particle models developed so far. Finally, following the findings of the literature on fluidised bed heat transfer characteristics and in combination with a CFD model like the one developed in this study, the engineer can be easily guided towards the correct selection of feedstock properties for the optimum operation of a specific kind of reactor.

Chapter 5

Case studies

The chapter presents four applications of the computational model developed for fast pyrolysis. The case studies include the examination of the effect of particle size, particle shape and point of injection on char entrainment in fluidised beds, as well as the effect of biomass shrinkage on heat, momentum transport and product yields, and the effect of particle size on the bed-to-surface heat transfer coefficient. The examined case studies can show any defects on the design of the reactor and can provide substantial information for optimisation and determine the most appropriate biomass particle sizes and shapes for this kind of reactor. All the cases are based on the core computational code for heat, mass and momentum transport in fluidised beds. Whenever the code is extended to account for additional physical phenomena, the extension equations are analytically presented.

5.1 CFD investigation on the effect of particle size on char entrainment in bubbling fluidised beds

In this case study the fluid - particle interaction inside the $150g/h$ fluidised bed reactor of fig. 4.1 is modelled. Three char particles of sizes $500\mu m$, $250\mu m$, and $100\mu m$ are injected into the fluidised bed and the momentum transport from the fluidising gas and fluidised sand is modelled. Due to the fluidising conditions and reactor design the char particles will either be entrained from the reactor or remain inside the bubbling bed. The particle size is the factor that differentiates the particle motion inside the reactor and their efficient entrainment. The 3-Dimensional simulation has been performed using the revised momentum transport model presented in section 4.1. Heat transfer from the bubbling bed to the char particles is not taken into account, since the particles are assumed to have been totally pyrolysed and converted to char. The density used for the char particles is $200kg/m^3$, which is a representative value of char (table 5.1). In a real situation though, the final density of the particles would rather depend on the rate as well as the degree of biomass degradation.

Three random positions inside the sand were chosen for the injection of the char particles. Table 5.1 defines the char particle injection positions as well as the rest of the simulation parameters.

Property	Value	Comment
Reactor central axis,	$(0.0, 0.0, 0.0)$	Along the height of the reactor
$500\mu m$ particle,	$(0.0, 0.04, 0.0)$	Centre of sand bed
$250\mu m$ particle,	$(0.01, 0.06, 0.01)$	Random point at the sand bed
$100\mu m$ particle,	$(0.005, 0.05, -0.01)$	Random point at the sand bed
$U_{t_{500}}$	$0.57m/s$	Terminal velocity of $500\mu m$ particle
$U_{t_{250}}$	$0.18m/s$	Terminal velocity of $250\mu m$ particle
$U_{t_{100}}$	$0.032m/s$	Terminal velocity of $100\mu m$ particle
Gas density, ρ_g	$0.456kg/m^3$	Nitrogen ($773K$)
Gas viscosity, μ_g	$3.44 \times 10^{-5}kg/ms$	Nitrogen ($773K$)
Char particles density, ρ_d	$200kg/m^3$	Char
Solids particle density, ρ_s	$2500kg/m^3$	Sand
Mean solids particle diameter, d_s	$440\mu m$	Uniform distribution
Restitution coefficient, e_{ss}	0.9	Value in literature
Initial solids packing, ε_s	0.63	Fixed value
Static bed height	$0.08m$	Fixed value
Bed width	$0.04m$	Fixed value

Table 5.1: Simulation parameters for different size char particles

Fig. 5.1 shows the bed hydrodynamics and relative particle positions at different times of the simulation in an isometric representation. Since it was impossible to capture all three particle positions at the isometric views of fig. 5.1 due to bubble formation and eruption, slices across the sand bed at $0.02m$ intervals were taken at time $t = 1.0s$ (fig. 5.2) to visualise the flight of the particles inside the reactor. The outlet of the reactor is also visible.

The simulation lasted for 1.5 seconds which means that the flight time of the particles was 1 second (injection of particles started at 0.5 seconds of the simulation).

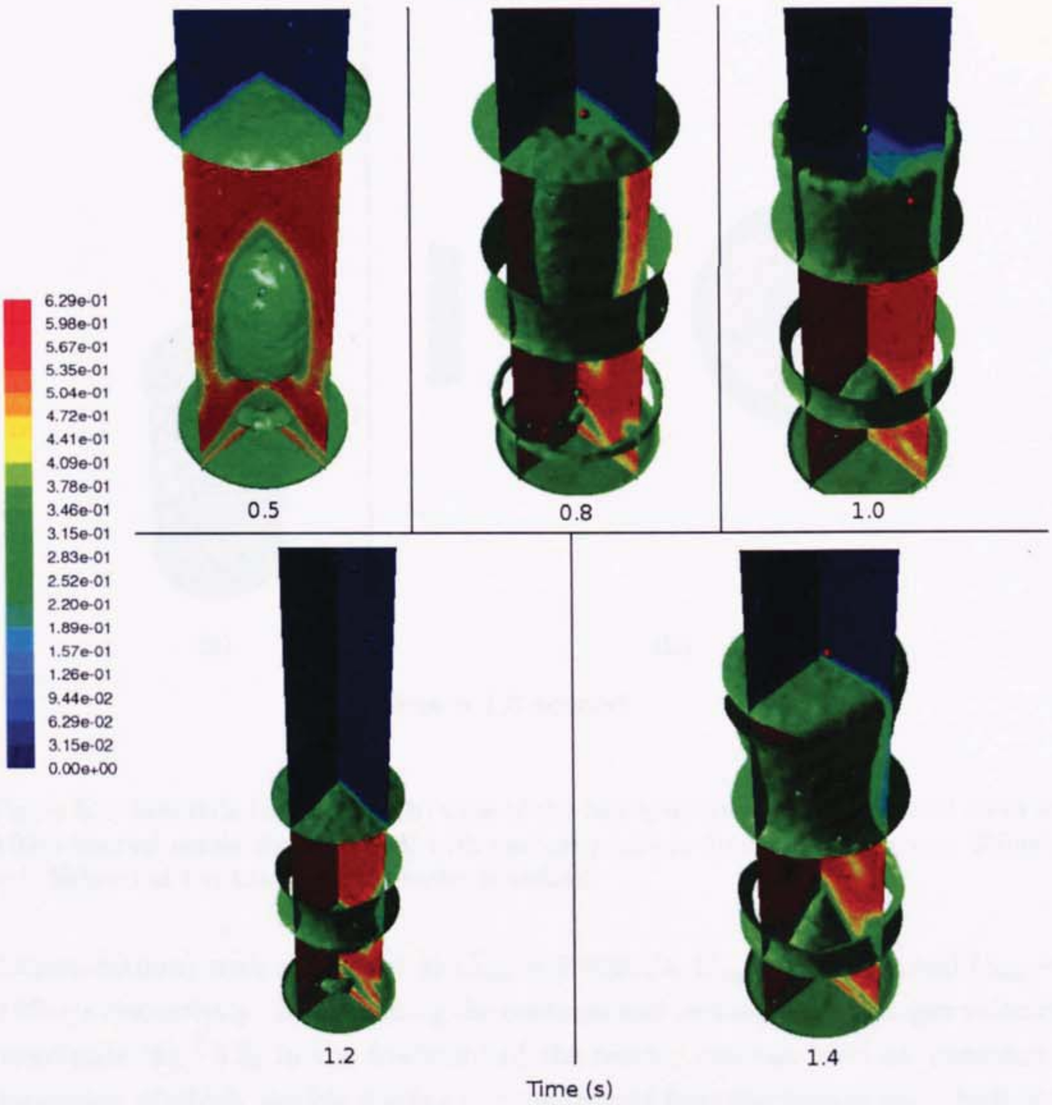

Figure 5.1: Fluidised bed hydrodynamics with char particle positions. Nitrogen bubbles shown at 0.7 volume fraction.

There are numerous correlations to determine the terminal velocity of a particle and the reader is referred to [1] for a detailed description. The particles were injected at random positions inside the reactor at $t = 0.5s$ and the momentum transport from the fluidised bed was calculated according to the momentum transport model presented in section 4.1. However, when the particles were ejected from the bed to the freeboard of the reactor, the particles are carried only by the upward flowing gas stream. The terminal velocities of the three different size particles ($100\mu m$,

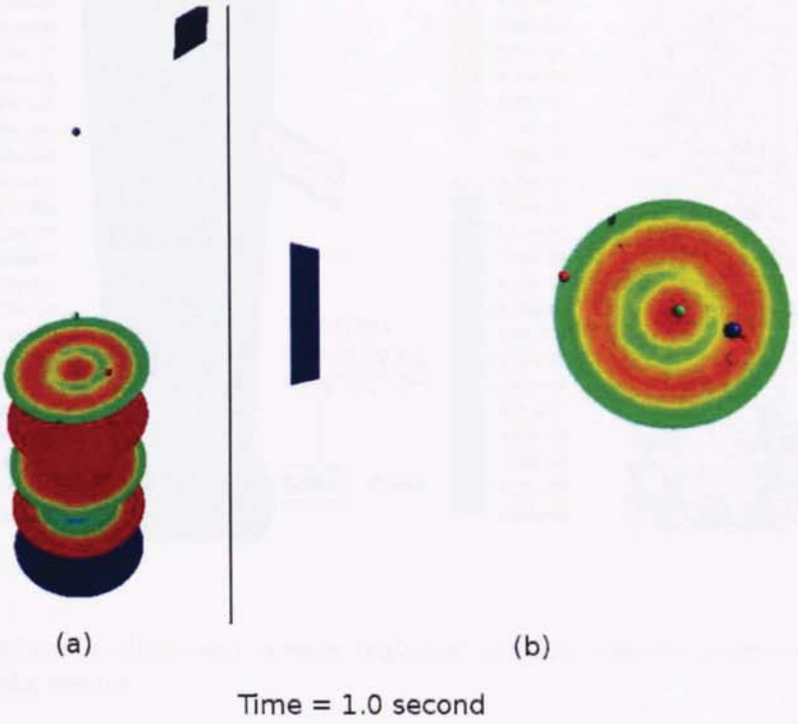

Figure 5.2: Isometric (a) and top (b) view of the bed hydrodynamics (horizontal slices at $0.02m$ interval across the sand bed) with particle positions (blue: $100\mu m$, green: $250\mu m$, red: $500\mu m$) at $t = 1.0s$. Reactor outlet is visible.

$250\mu m$, $500\mu m$) were calculated as $U_{t_{100}} = 0.032m/s$, $U_{t_{250}} = 0.18m/s$ and $U_{t_{500}} = 0.57m/s$ respectively. By examining the contours and vectors of the nitrogen velocity magnitude (fig. 5.3) in the freeboard of the reactor one can have an immediate impression of which particle is going to be entrained from the reactor and which one is more likely to fall back into the bed.

The velocity magnitude of nitrogen in the freeboard of the reactor ranges from $\approx 0.25-3m/s$. However, the maximum increase in velocity occurs close to the outlet of the reactor. The maximum velocity of nitrogen in the transport disengaging zone of the reactor only reaches $0.47m/s$. In this specific region of the reactor the finer particles are separated from the larger ones and entrained from the reactor. By comparing the velocity of nitrogen and the terminal velocities of the three char particles that have been injected, we should expect the $100\mu m$ and $250\mu m$ particles to be entrained from the reactor while the $500\mu m$ to fall back into the bed and continue mixing with the sand particles.

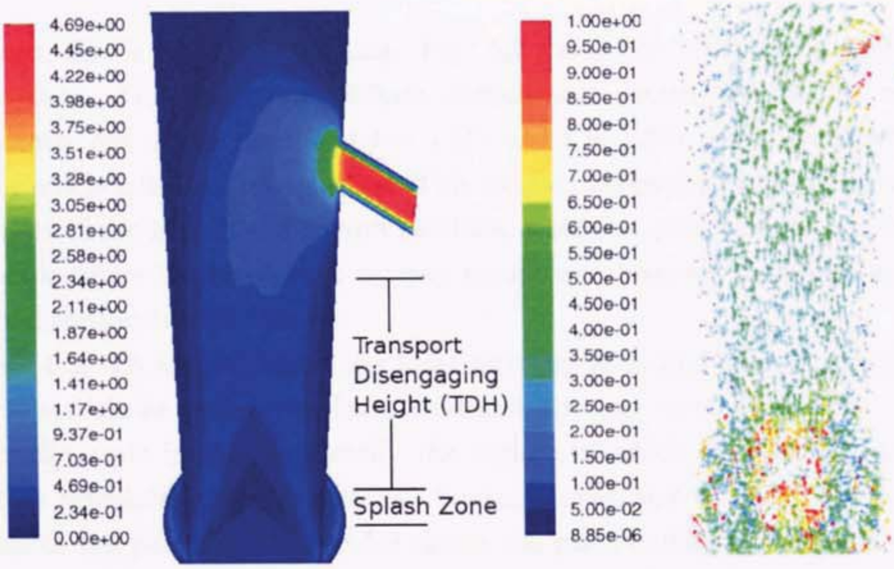

Figure 5.3: Contours (left) and vectors (right) of nitrogen velocity magnitude at the freeboard of the reactor

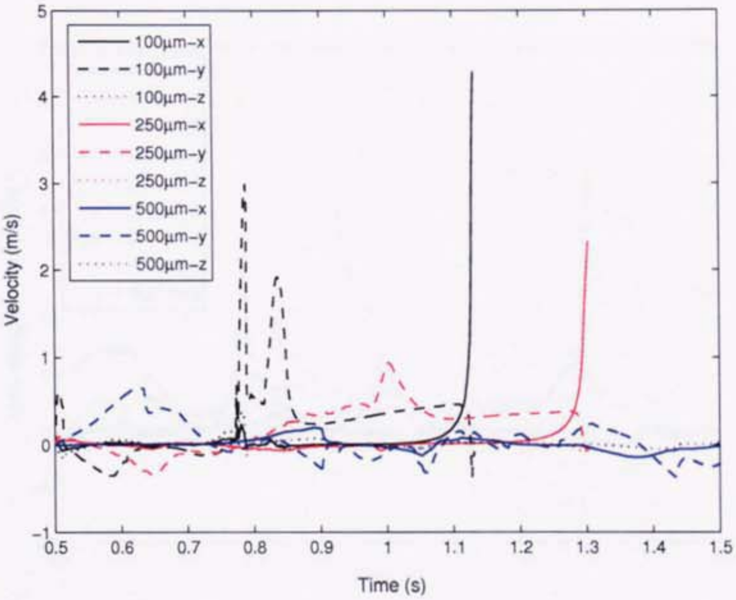

Figure 5.4: Velocities of the three char particles in the x, y, z direction

Indeed, this is what is happening. Fig. 5.4 shows the velocity components for each particle. The $100\mu m$ and $250\mu m$ particles are entrained from the bed and consequently out of the reactor at $t = 1.13s$ and $t = 1.30s$ respectively, while the $500\mu m$ particle falls back into the bed. This can be seen by the increase in x-velocity component of the $100\mu m$ and $250\mu m$ particles, which happens close to the outlet of the reactor where the nitrogen x-velocity component becomes dominant and drag in the x-direction is more intense.

Figs. 5.5, 5.6 and 5.7 show the local nitrogen and sand velocity components for each particle as well as the local sand and nitrogen volume fractions. This is the way the code is able to identify the regime in which each particle is found as well as calculates the gravitational, buoyant, drag and virtual mass forces for each one of the particles. Figure 5.8 shows the particle flights inside the reactor. The Cartesian coordinates refer to the reactor dimensions considering as centre the $(0, 0, 0)$ coordinate at the bottom of the reactor. The $100\mu m$ and $250\mu m$ particles are efficiently entrained from the reactor (reactor outlet $(0.02, 0.21, 0)$), while the $500\mu m$ one remains inside the bed despite the fact that the bed has ejected it in the freeboard several times as it is illustrated in figs. 5.1, 5.2 and 5.8.

Figures 5.9 and 5.10 show the drag and virtual mass forces calculated for each

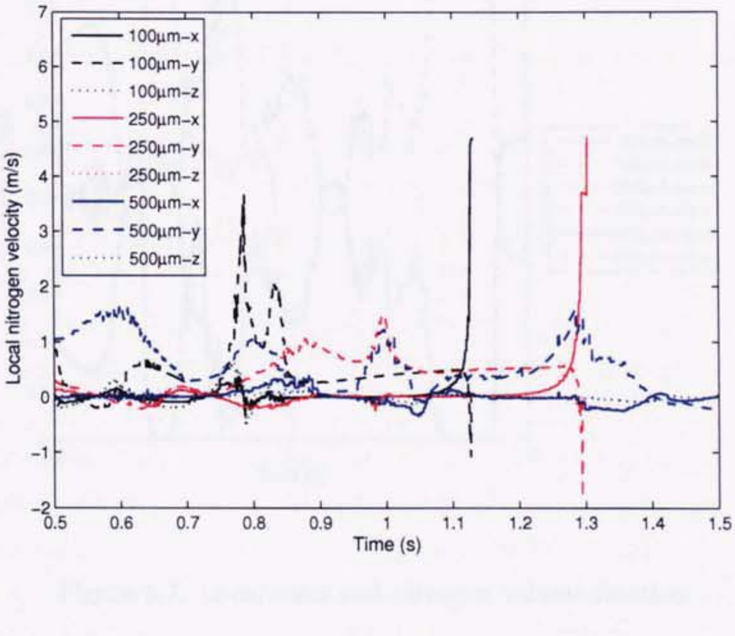

Figure 5.5: Local nitrogen velocity for each particle

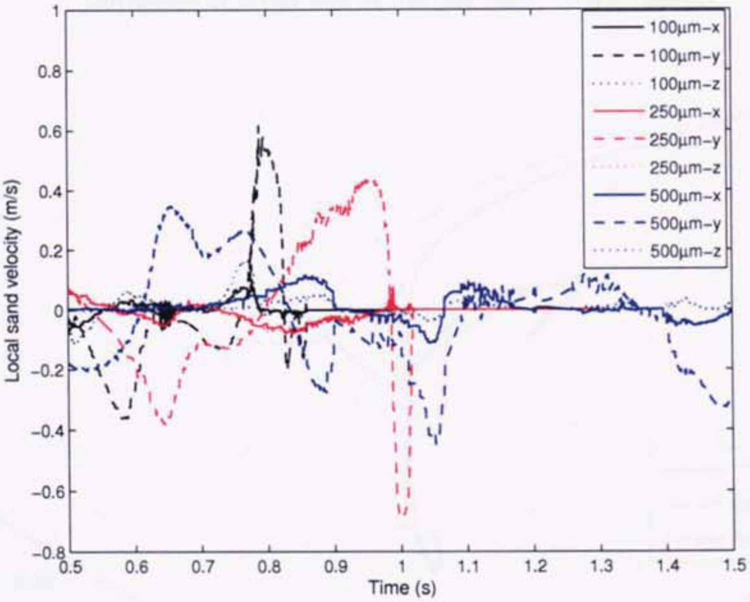

Figure 5.6: Local sand velocity for each particle

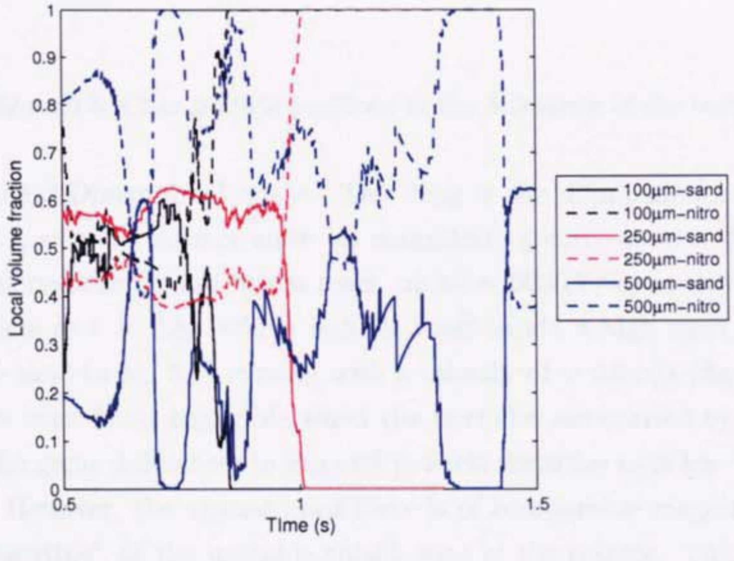

Figure 5.7: Local sand and nitrogen volume fraction

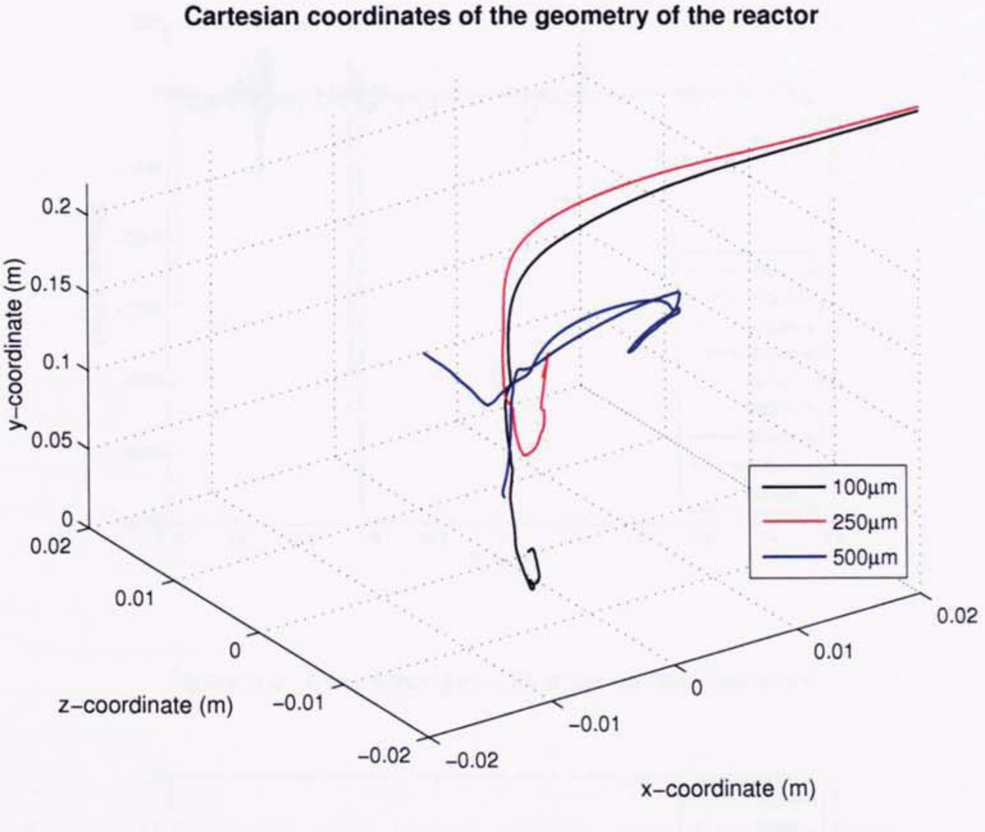

Figure 5.8: Char particle positions in the 3-D space of the reactor

particle in the 3-Dimensional space. The drag is the dominant force that moves the particles inside the reactor since its magnitude greatly exceeds the magnitude of the virtual mass force and it can reach up to $\approx 6000N/kg$ as in the case of the $100\mu m$ particle at $t \approx 0.8s$, where it finds itself inside a high sand concentration zone ($\approx 60\%$ sand in fig. 5.7) moving with a velocity of $\approx 0.6m/s$ (fig. 5.6). Virtual mass force is considered negligible when the particles are carried by the fluidising gas due to the great differences in gas and particle densities as it has been shown in section 4.1. However, the virtual mass force is of comparable magnitude when the particle is "floating" at the unstable splash zone of the reactor. This can be easily noticed by comparing the magnitude of drag and virtual mass forces for the $500\mu m$ particle in the region of $0.8 - 1$ seconds where the latter is ejected from the bubbling bed and falls back to the sand bed again. The amount of drag at the splash zone of the reactor comes close to $200N/kg$ where the virtual mass force at this point is

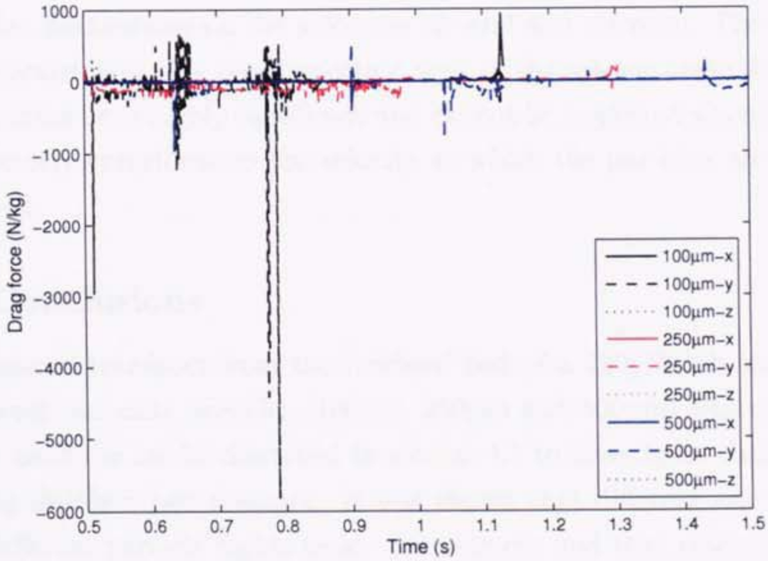

Figure 5.9: Drag force per unit mass on char particles

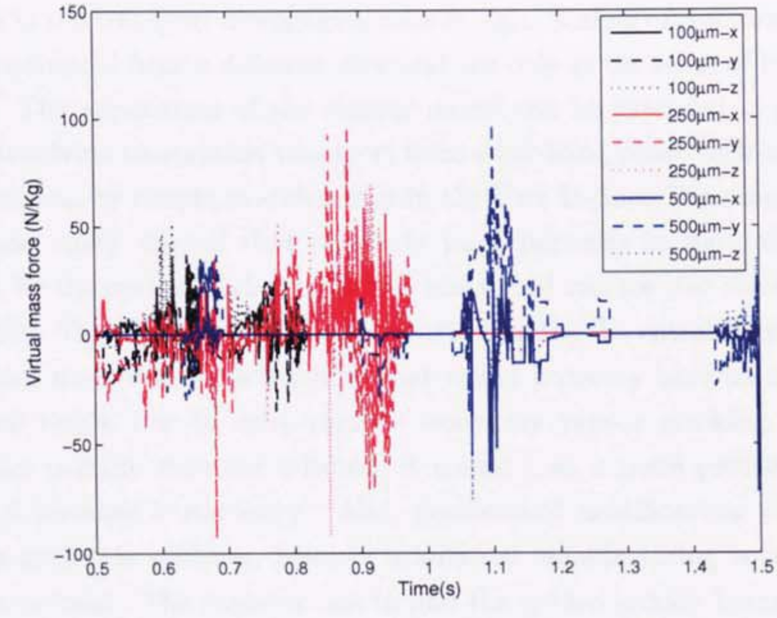

Figure 5.10: Virtual mass force per unit mass on char particles

almost $100N/kg$. The unstable nature of the splash zone where the bubbles erupt, cause sudden fluctuations on the velocities of sand and nitrogen. The high velocity gradients occurring at this very important zone of the reactor make the inclusion of the virtual mass force highly significant and cannot be neglected since its magnitude will significantly contribute to the velocity at which the particles are ejected from the sand bed.

5.1.1 Conclusions

The momentum transport from the fluidised bed of a $150g/h$ lab scale reactor to three different size char particles ($100\mu m$, $250\mu m$ and $500\mu m$) was modelled. The case study used the model described in section 4.1 to investigate char entrainment in bubbling fluidised bed reactors. It was shown that different size particles will result in different particle flights inside the reactors and that reactor design could be optimised by modifications guided by the simulations.

Char entrainment is of high importance in fast pyrolysis, since vapours are catalyzed by char/ash and reduce bio-oil yields. The significance of a computational model that is able to predict particle residence times as well as char and sand particle elutriation in the transport disengaging zone is high. Scaling of reactors can be modelled and optimised from a different view and not only in the sense of hydrodynamic similarity. The application of the current model can be extended to several other processes involving momentum transport from a bubbling phase such as combustion and gasification, by simple modifications in the User Defined Function.

The case study showed that relatively large particles in the order of $500\mu m$ would not be the optimum choice for a fluidised bed reactor like the one modelled in this study. The higher volume of the particle makes the entrainment of the final char product more difficult something that would certainly have an impact at the final bio-oil yields, due to extra-particle secondary vapour cracking. In the case that smaller particle sizes are selected, it means that a more precise and intense grinding of biomass is necessary. Also, geometrical modifications of the reactor could overcome this problem, however additional manufacturing costs have to be taken into account. The engineer has to find the golden section between accuracy, cost and efficiency for this kind of process.

As it was mentioned in section 4.1, the rotational effects of the particles were not taken into account due to certain programming limitations. Also, the assumption that the char particles were totally spherical was made. The sphericity effects are further analysed in section 5.2. However, one can state that the model accurately predicted the different size particle behaviour and entrainment inside the reactor using simple calculations. It was also shown how the virtual mass force acting on the particle plays a significant role when the particle finds itself at the unstable splash zone and how the bubble eruption, which results to sudden velocity fluctuations, gives rise to virtual mass and becomes of comparable magnitude with the exerted drag force.

5.2 Modelling the effects of sphericity and injection point on char entrainment from bubbling fluidised beds

In this study, the interaction between non-spherical particles and continuous fluids inside a $150g/h$ fluidised bed reactor is modelled. Three char particles of $350\mu m$ size but different shape (cube, sphere, tetrahedron) are injected into the fluidised bed and the momentum transport from the fluidising gas and fluidised sand is modelled. Due to the fluidising conditions, reactor design, particle shape and point of injection, the char particles will either be entrained from the reactor or remain inside the bubbling bed. The sphericity of the particles is the factor that differentiates the particle motion inside the reactor and their efficient entrainment out of it. A 3-Dimensional simulation has been performed using the momentum transport model for bubble three-phase flow as it has been described in section 4.1. Heat transfer between the continuous and discrete phases is not taken into account, because it is assumed that the non-spherical particles have already been pyrolysed and converted to char.

Three different shape particles (cube, sphere, tetrahedron) were selected to study the effect of sphericity on the particle trajectory inside the reactor. Fig. 5.11 illustrates the three different particle shapes used in the current simulation.

The motion of the particles inside the reactor is computed using the momentum transport model described in section 4.1. However, for a nonspherical particle the degree of sphericity has to be taken into account. This is quantified by the shape factor,

$$\Psi = \frac{A_{sp}}{A}, \tag{5.1}$$

Figure 5.11: Particle shapes

where A_{sp} is the surface area of the sphere of the same volume with the nonspherical particle and A is the actual surface area of the latter. The surface area of the equivalent sphere is

$$A_{sp} = \pi^{1/3}(6V)^{2/3}, \tag{5.2}$$

where V is the particle volume. The corresponding diameter of the equivalent sphere is

$$D_{sp} = \left(\frac{6V}{\pi}\right)^{1/3}. \tag{5.3}$$

The effective Reynolds number is calculated for the modified sphere diameter (inserting D_{sp} in eq. 3.66) as well as the effective drag factor (Eq. 3.68 and 3.69). The virtual mass force (eq. 3.77) is also affected since it is a function of the volume of the particles. The effective volume of the particles is quite different therefore differences on the virtual mass force are also expected, when the particles find themselves inside similar conditions of bubbling. The injection point of the particles is quite different as well. The tetrahedral particle was injected at the centre of the sand bed, while the cubical and spherical particles were injected closer to the wall of the reactor in the x-axis and z-axis respectively. In this way one can notice the effect of the point of injection since the particle size is similar but the shape is different. In the case study presented in section 5.1 the injection points were quite different as well, however the extreme differences in particle sizes made the comparison of these effects more difficult. Table 5.2 shows the simulation parameters of the effect of sphericity case.

The three different shape particles were injected inside the sand bed at random

Property	Value	Comment
Reactor central axis	$(0.0, 0.0, 0.0)$	Along the height of the reactor
Tetrahedral particle	$(0.0, 0.04, 0.0)$	Centre of sand bed
Spherical particle	$(-0.01, 0.05, 0.005)$	Random point at the sand bed
Cubical particle	$(0.005, 0.035, -0.01)$	Random point at the sand bed
Effective diameter of tetrahedron	$210\mu m$	Computed from eq. 5.3, $\Psi = 0.671$
Effective diameter of sphere	$350\mu m$	Totally spherical, $\Psi = 1$
Effective diameter of cube	$437\mu m$	Computed from eq. 5.3, $\Psi = 0.806$
Terminal velocity of tetrahedron	$0.132m/s$	Fluid: Nitrogen at $773K$
Terminal velocity of sphere	$0.326m/s$	Fluid: Nitrogen at $773K$
Terminal velocity of cube	$0.465m/s$	Fluid: Nitrogen at $773K$
Gas density, ρ_g	$0.456kg/m^3$	Nitrogen ($773K$)
Gas viscosity, μ_g	$3.44 \times 10^{-5}kg/ms$	Nitrogen ($773K$)
Solids particle density, ρ_s	$2500kg/m^3$	Sand
Mean solids particle diameter, d_s	$440\mu m$	Uniform distribution
Restitution coefficient, e_{ss}	0.9	Value in literature
Initial solids packing, ε_s	0.63	Fixed value
Static bed height	$0.08m$	Fixed value
Bed width	$0.04m$	Fixed value

Table 5.2: Simulation parameters for different shape char particles

positions as it is shown on table 5.2, at time $t = 0.5$ seconds. Due to extensive computational needs and power necessary, the simulation lasted for ≈ 1.45 seconds, which is the time where two of the particles have been entrained.

Figure 5.12 shows the relative position of the particles with the bubbles formed in the bed at different times of the simulation. At time $t = 0.5$ seconds only the cubical particle is visible and that means that at the time of injection the spherical and tetrahedral particles were injected in side the bubble. Also at time $t = 1.4$ seconds the tetrahedral particle has already escaped from the reactor as well as the cubical one is ready to do so. However the spherical particle remained inside the reactor for the 1.45 seconds of simulation.

As table 5.2 suggests the terminal velocity of the spherical particle ($0.326m/s$) is much lower than the terminal velocity of the cube ($0.465m/s$). Thus, there is no question that the sphere should be entrained from the bed since the cube did. However, this is also a matter of where the particle has been injected and its radial position inside the reactor. The spherical particle has been trapped inside the bed because of its injection point close to the wall. Figures 5.12, 5.13 and 5.14 show that the spherical particle is not only injected close to the wall but is also pushed towards

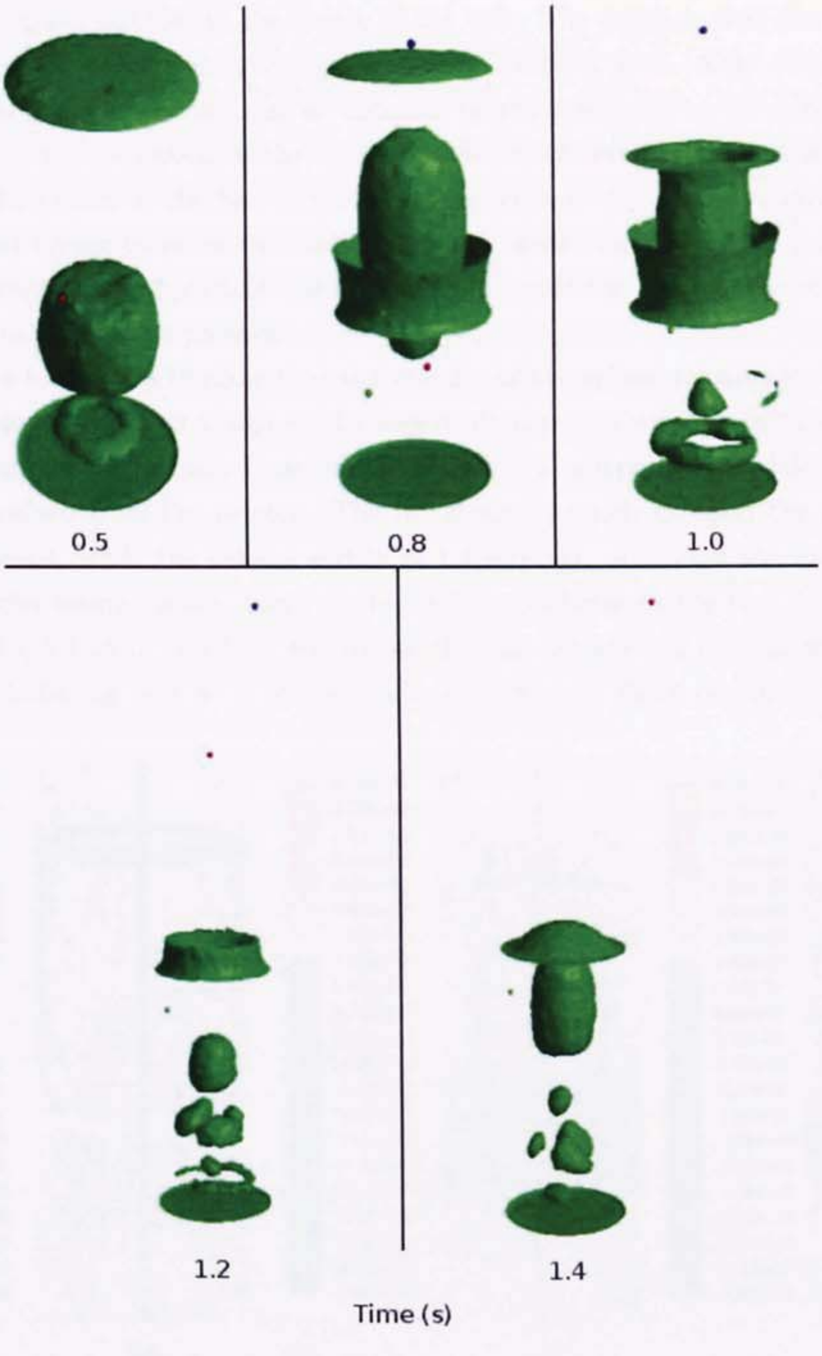

Figure 5.12: Bubbles in the bed with relative particle positions at different times (blue: tetrahedral, green: sphere, red: cube). Bubbles shown at Nitrogen volume fraction of 0.7.

it by the formed bubbles in the centre of the bed. The result is that the spherical particle cannot be efficiently ejected from the bubbling bed. Also, the fact that the cubical particle was injected at different height compared to the spherical one and avoided the formation of the initial bubble at 0.5 seconds made it be directed towards the centre of the bed in the following seconds due to the relative motion of the sand trying to cover the "sand vacuum" caused by the bubble passage. In contrast, the spherical particle was further sunk inside the bed by the recirculating sand due to the bubble passage.

Figures 5.15 and 5.16 show that the velocity of the sphere remains low and that the particle is always in a high sand concentration region without being ejected to the freeboard of the reactor. However, the tetrahedral and cubical particles managed to be entrained from the reactor. The tetrahedral particle escaped the reactor in ≈ 1.2 seconds, while the cubical one in ≈ 1.4 seconds. Although the flight of the two particles seems similar, there are big differences between the two. Comparing, figures 5.15, 5.16,5.17 and 5.18, we can see that the tetrahedral particle was ejected from the bubbling bed at ≈ 0.8 seconds and then its flight continued normally

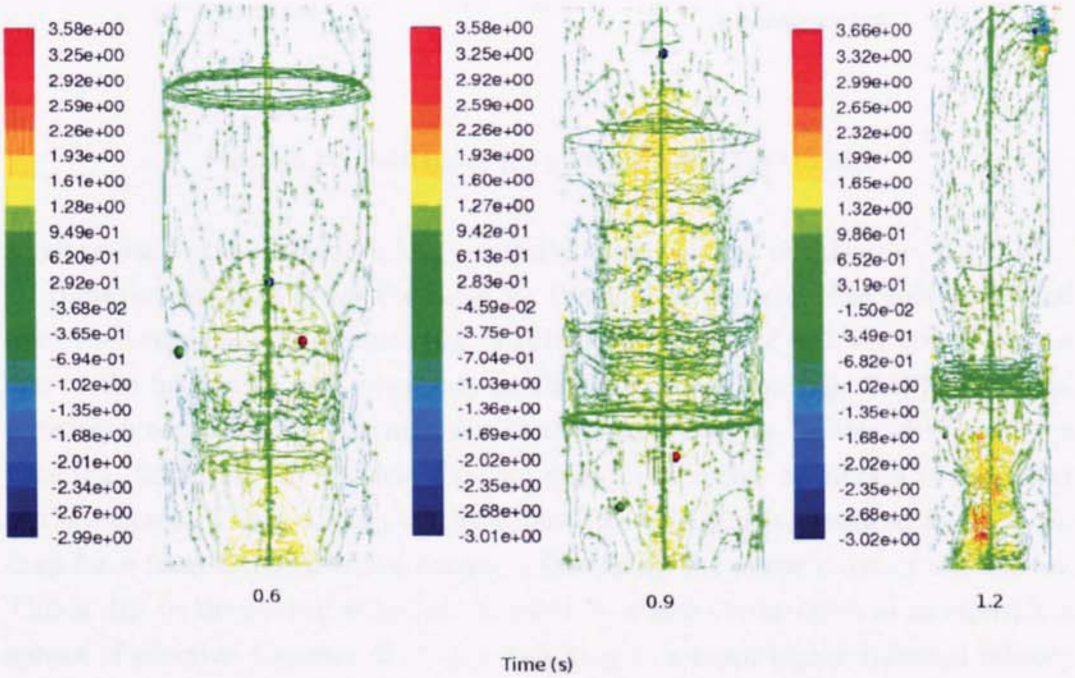

Figure 5.13: Contours of Nitrogen y-velocity component with velocity vectors and particle positions at different times (blue: tetrahedral, green: sphere, red: cube).

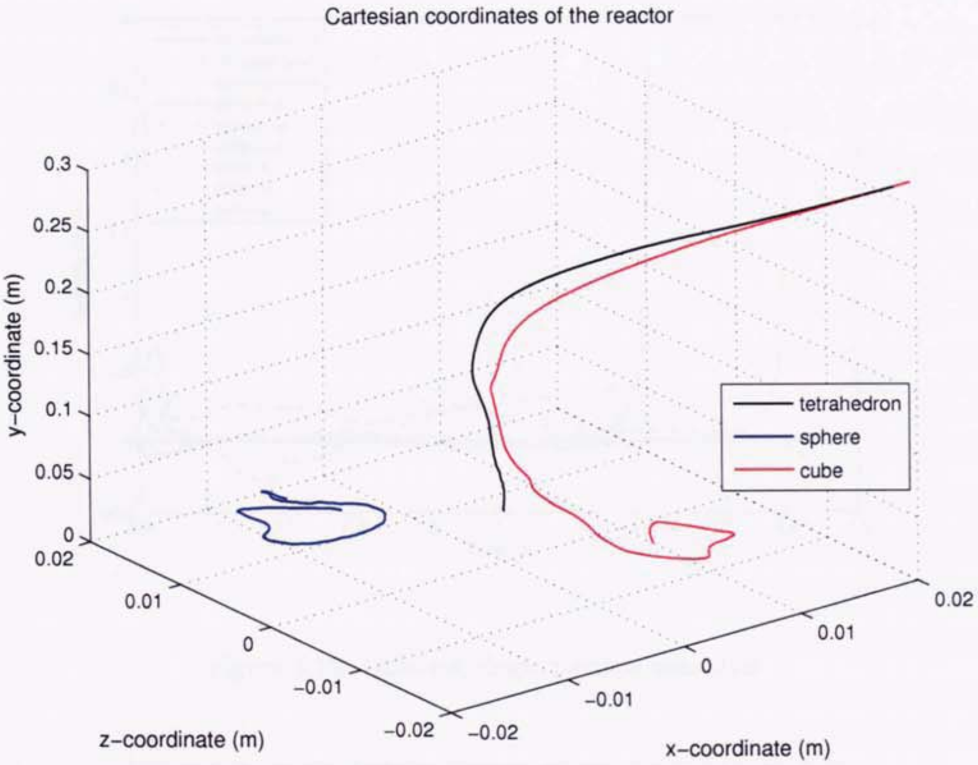

Figure 5.14: Position of the particles inside the reactor.

accelerating to the reactor outlet (y-velocity component of tetrahedron, fig. 5.15).

However, the case is not the same for the cubical particle. The cube is ejected from the bed at ≈ 0.97 seconds (fig. 5.16)with a velocity of $\approx 1 - 1.5m/s$. This is due to the high local sand y-velocity at the time of ejection (fig. 5.17). The local y-nitrogen component is also high due to the eruption of the bubble at the ejection time (fig. 5.18), but the particle does not seem to smoothly accelerate to the outlet of the reactor. The y-velocity of the cubical particle is being reduced because the drag force from nitrogen is not capable of dragging the particle out of the reactor. This is due to the cubical shape of the particle, which corresponds to an equivalent sphere of effective diameter of $437\mu m$, resulting to a much higher terminal velocity than the tetrahedral particle. Thus, the particle slows down since the sum of the drag and virtual mass forces (figs. 5.19, 5.20) are not enough to carry out the particle. The particle will slow down until the relative velocity between the latter

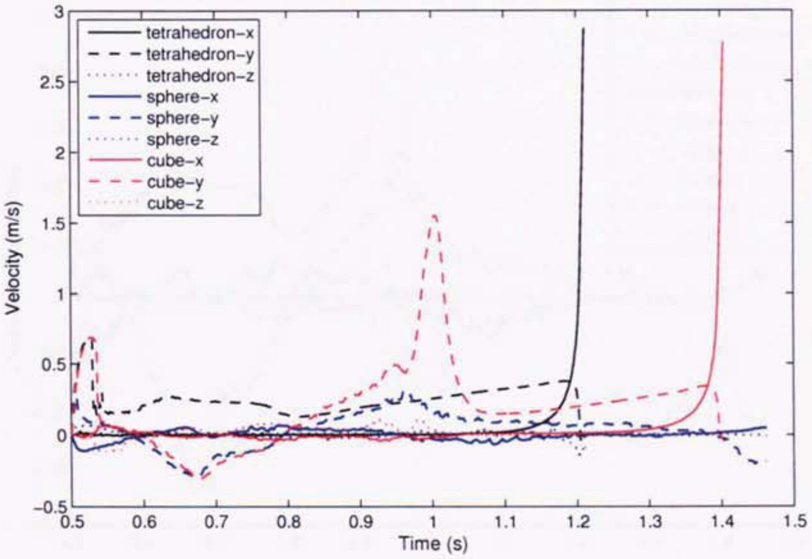

Figure 5.15: Different shape particle velocities

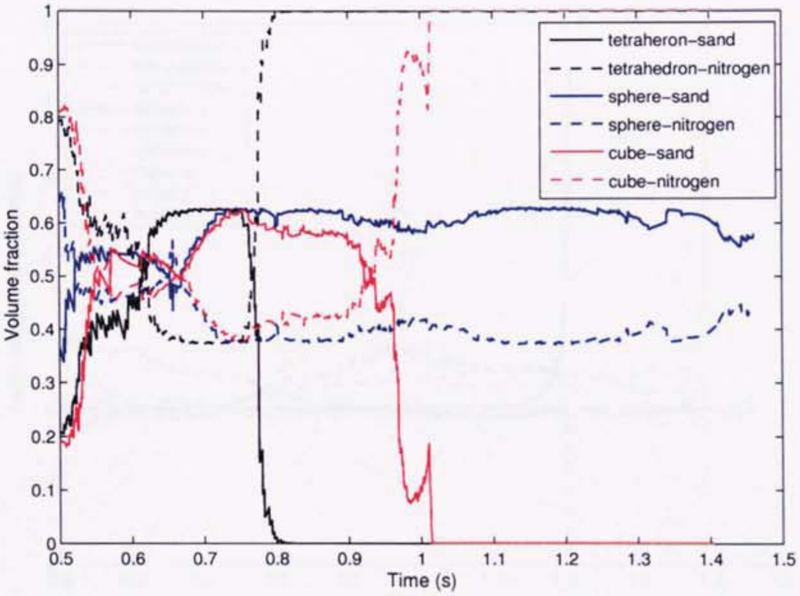

Figure 5.16: Local volume fraction.

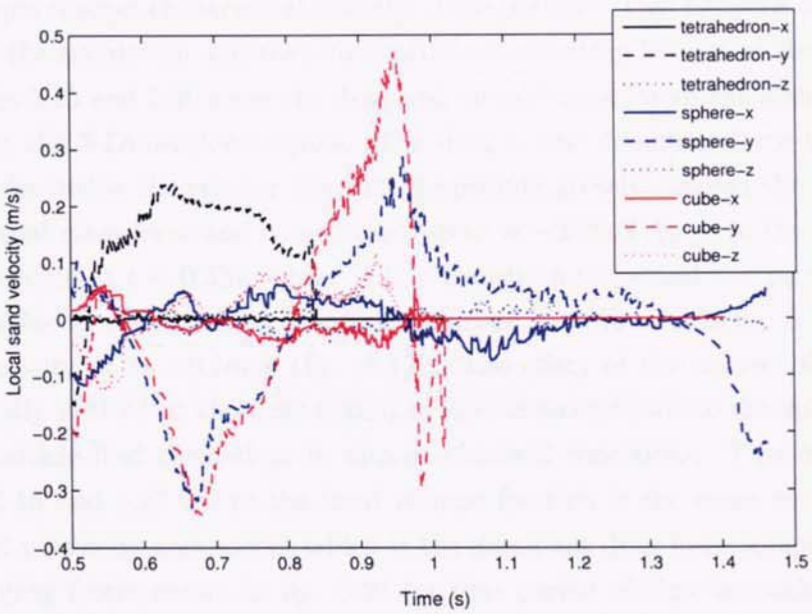

Figure 5.17: Local sand velocity.

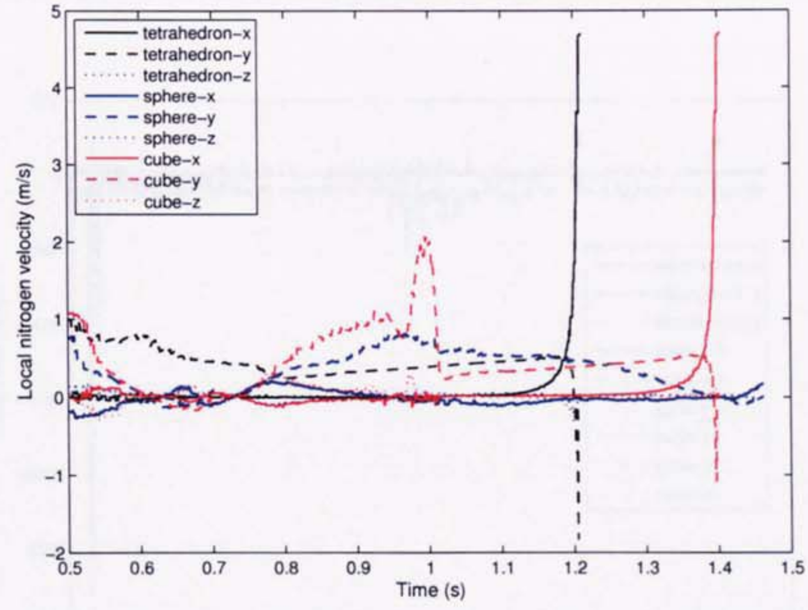

Figure 5.18: Local nitrogen velocity.

and nitrogen reaches the terminal velocity of the particle. This happens at the ≈ 1.1 second of the simulation and then the particle is smoothly led out of the reactor.

Figures 5.19 and 5.20 show the drag and virtual mass forces calculated for each particle in the 3-Dimensional space. The drag is the dominant force that moves the particles inside the reactor since its magnitude greatly exceeds the magnitude of the virtual mass force and it can reach up to $\approx -3000N/kg$ as in the case of the cubical particle at $t \approx 0.53s$, where it is a transition stage and the particle moves from a bubble to a higher sand concentration zone ($\approx 40\%$ sand in fig. 5.16) moving with a velocity of $\approx -0.1m/s$ (fig. 5.17). The effect of the degree of sphericity can be easily noticed at the time period of 0.6-0.8 seconds where the spherical and cubical particle find themselves in almost identical conditions. This can be seen in figs. 5.16 and 5.17 where the local volume fraction is the same as well as the local sand y-velocity component which is the dominant drag force component. The effective drag factor shown in fig. 5.21 for that period of time is much higher for the cubical particle since it is a function of the particle Reynolds number which becomes greater for a higher effective diameter of the particle. The average drag factor difference for the two particles at the same conditions is close to 1 unit. Thus, the drag force exerted on the cubical particle is expected to be higher. Virtual mass

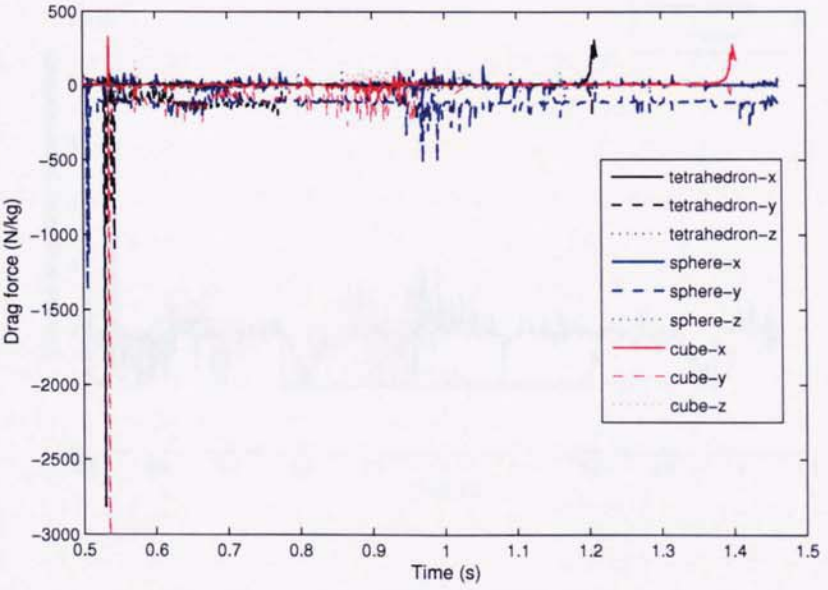

Figure 5.19: Drag force per unit mass.

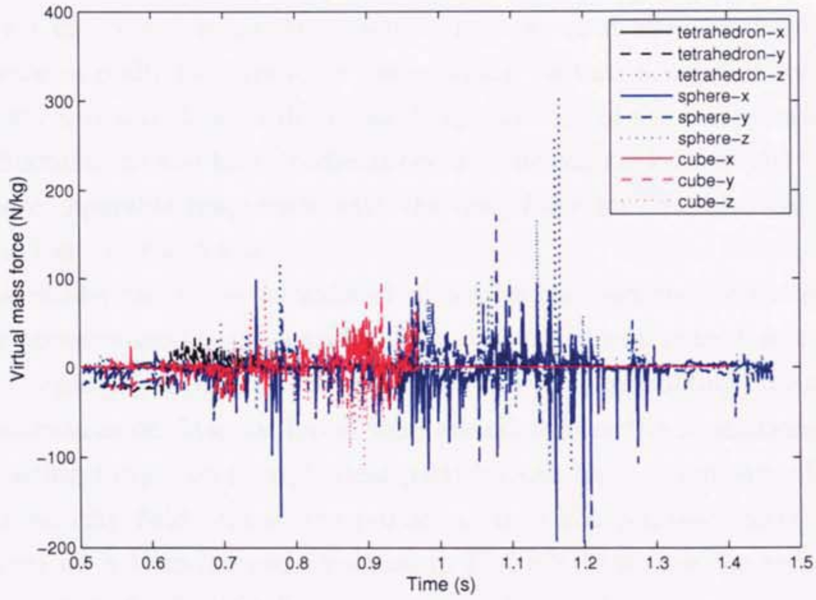

Figure 5.20: Virtual mass force per unit mass.

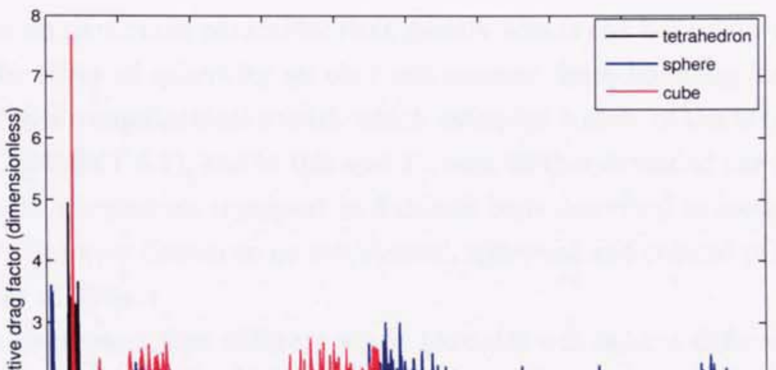

Figure 5.21: Effective drag factor

force is considered negligible when the particles are carried by the fluidising gas due to the great differences in gas and particle densities as it was mentioned in section 4.1. It becomes really important for the spherical particle because it remains inside the fluidised bed and close to the unstable splash zone of the reactor where sudden velocity fluctuations and high gradients occur. One can notice that the virtual mass force is of comparable magnitude with the drag force for the spherical particle by comparing figs. 5.19 and 5.20.

In this study, the forces considered to act on the particle are the steady-state drag, the pressure gradient, buoyancy force and the virtual mass force. Rotational effects of the particle have not been considered due to programming limitations so lift forces (Saffman force, Magnus force) were excluded from the simulations. However, the fluctuating torque on nonspherical particles can have significant effects due to the shear velocity field around the particles. It is not possible though to include these effects on a User-Defined Function in FLUENT because the access of solver variables is limited. FLUENT calculates rotational effects on particles when one uses the models already included in FLUENT's core code.

5.2.1 Conclusions

Sphericity is an important parameter that greatly affects the behaviour of a moving particle. The effect of sphericity on char entrainment from bubbling fluidised beds was studied in a computational model, which extended a state of the art commercial CFD code (FLUENT 6.2), and in this specific case further extended the user defined sub-routine for momentum transport in fluidised beds described in section 4.1. The studied particles were chosen to be tetrahedral, spherical and cubical of sides length and diameter of $350\mu m$.

The results showed that different shape particles will behave differently as they move inside the fluidised bed. It was also shown in the case of the spherical particle that its radial position of injection on the reactor has a great effect in its residence time. The results were very distinct even in this case that very small particles were examined ($350\mu m$) and it is expected that the effect will be greater in even larger particles. The magnitude of the drag force was greater for the largest effective diameter particle when the same conditions were examined since the drag factor is heavily dependent on the particle Reynolds number which increases with particle diameter. The virtual mass force should behave in a similar manner since it is a directly proportional to the effective volume of the particle, however its dependence on the fluid velocity gradients cannot make this distinction clearly obvious.

One cannot derive a general conclusion of optimum shape of particles. Non-spherical particles present peculiar heat transfer characteristics which may result to poor biomass degradation. Also, it is difficult to model the heat transfer characteristics of complex shapes due to the lack of symmetry about any possible axis. In a process such as fast pyrolysis, where good intra and extra-particle heat transfer is of great importance as well as particle and vapour residence times, one cannot certainly desire any shape and size of particles that either limit the product yields by fast entrainment without significant conversion or by catalysis of vapours due to extremely long residence times. The phenomena have to be carefully treated and optimum selections of particle sizes and shapes have to be made.

In chemical processes, all sorts of shapes and sizes of particles can be found. The challenge is to design and optimise reactors and chemical process equipment, to be able to deal with a large range of particle shapes and sizes. Computational models can provide a good indication of what may happen in such cases. Char entrainment is of high importance in fast pyrolysis, since vapours are catalyzed by char/ash and reduce bio-oil yields. The significance of a computational model that will be able to predict particle residence times as well as char and sand particle elutriation in the transport disengaging zone is high.

5.3 Modelling the effect of biomass shrinkage

In this case study, the fluid - particle interaction and the impact of shrinkage on pyrolysis of biomass inside the $150g/h$ fluidised bed reactor is modelled. Two $500\mu m$ in diameter biomass particles are injected into the fluidised bed with different shrinkage conditions. The two different conditions consist of 1) shrinkage equal to the volume left by the solid devolatilisation, and 2) shrinkage parameters equal to approximately half of particle volume. The effect of shrinkage is analysed in terms of heat and momentum transfer as well as product yields, pyrolysis time and particle size considering spherical geometries. The Eulerian approach is used to model the bubbling behaviour of the sand, which is treated as a continuum. Heat transfer from the bubbling bed to the discrete biomass particle, as well as biomass reaction kinetics are modelled according to the penetration theory of Mickley and Fairbanks [78] and two-stage semi-global mechanism of fig. 2.8, with kinetic constants given at table 3.3. The particle motion inside the reactor is computed using the revised momentum transport model described in section 4.1.

5.3.1 Shrinkage parameters

The current section introduces the shrinking parameters applied to the discrete particles. The volume occupied by the solid structure of the particle is assumed to decrease linearly with the wood mass and to increase with the char mass, by a chosen shrinkage α_{sh}, as devolatilisation takes place.

$$\frac{V_S}{V_{W0}} = \frac{m_W}{m_{W0}} + \frac{\alpha_{sh} m_C}{m_{W0}} \tag{5.4}$$

The volume occupied by the volatiles is made by two contributions. The first is due to the initial volume occupied by the volatiles V_{G0}, and the second by the fraction β_{sh}, of the volume left by the solid as consequence of devolatilisation $(V_{W0} - V_S)$:

$$V_G = V_{G0} + \beta_{sh}(V_{W0} - V_S). \tag{5.5}$$

To account for structural changes during pyrolysis, V_{G0} also varies linearly with the composition of the degrading medium from an initial value V_{gi} determined by the initial solid porosity to a final value taken as a fraction, γ_{sh} of the initial one $(V_{Gf} = \gamma_{sh} V_{Gi})$: $V_{G0} = \eta V_{Gi} + (1-\eta) V_{Gf}$, where $\eta = m_W / m_{W0}$. Thus, the total volume is expressed as

$$V = V_S + V_G = \eta V_{Gi} + (1-\eta)\gamma_{sh} V_{Gi} + \beta_{sh}(V_{W0} - V_S) + V_S. \tag{5.6}$$

In this study, the initial effective solids volume V_{W0} is taken as half of the initial biomass concentration. The shrinkage parameters were chosen to be different for each one of the injected particles.

1. $\alpha_{sh} = 1$, $\beta_{sh} = 0$, $\gamma_{sh} = 1$ (shrinkage equal to the volume left by the solid devolatilisation)

2. $\alpha_{sh} = 0.5$, $\beta_{sh} = 0$, $\gamma_{sh} = 0.5$.

The model will examine whether the differences in the shrinkage parameters will result in different particle behaviour inside the bed regarding heat and momentum transport from the fluidised bed, as well as product yields and residence times.

Property	Value	Comment
Biomass density, ρ_w	$700kg/m^3$	Wood
Biomass particle diameter, d_p	$500\mu m$	Fixed
Biomass specific heat capacity, C_{p_w}	$1500J/kgK$	Wood
Char specific heat capacity, C_{p_c}	$1100J/kgK$	Char
Biomass thermal conductivity, k_w	$0.105W/mK$	Wood
Char thermal conductivity, k_c	$0.071W/mK$	Char
Superficial velocity, U_0	$0.3m/s$	$\approx 4U_{mf}$
Gas density, ρ_g	$0.456kg/m^3$	Nitrogen ($773K$)
Gas viscosity, μ_g	$3.44 \times 10^{-5}kg/ms$	Nitrogen ($773K$)
Gas specific heat capacity, $C_{p,g}$	$1091.6J/kgK$	Nitrogen ($773K$)
Gas thermal conductivity, k_g	$0.0563W/mK$	Nitrogen ($773K$)
Solids particle density, ρ_s	$2500kg/m^3$	Sand
Sand temperature	$773K$	Uniform
Sand specific heat capacity, $C_{p,s}$	$835J/kgK$	Fixed
Sand thermal conductivity, k_s	$0.35W/mK$	Fixed
Mean solids particle diameter, d_s	$440\mu m$	Uniform distribution
Restitution coefficient, e_{ss}	0.9	Value in literature
Initial solids packing, ε_s	0.63	Fixed value
Static bed height	$0.08m$	Fixed value
Bed width	$0.04m$	Fixed value
Heat of reaction	$\Delta H = -255kJ/kg$	Koufopanos et al. [142]
Shrinkage parameters	$\alpha_{sh} = 1, \beta_{sh} = 0, \gamma_{sh} = 1$ $\alpha_{sh} = 0.5, \beta_{sh} = 0, \gamma_{sh} = 0.5$	Values in literature
Reactor central axis,	$(0.0, 0.0, 0.0)$	Along the height of the reactor
$\alpha = 0.5, \beta = 0, \gamma = 0.5$ particle,	$(-0.002, 0.04, 0.0)$	Injection point
$\alpha = 1, \beta = 0, \gamma = 1$ particle,	$(0.002, 0.04, 0.01)$	Injection point

Table 5.3: Simulation parameters for shrinkage of biomass

5.3.2 Model parameters

Table 5.3 shows the simulations parameters used for the modelling of the impact of biomass shrinkage.

For the implementation of the model certain parameters have been quantified and assumptions made, in order to provide, as much as possible, an insight to the fast pyrolysis process in bubbling beds.

- The reactor uses $\approx 350\mu m$ in diameter particles as feed. The particles used in the model were chosen to be $500\mu m$ in diameter. This was actually done to increase the Biot number as much as possible in order to get a relatively higher temperature gradient inside the particle.

- The particles used in the simulation were assumed to be totally spherical, whereas the particles used in experiments can be found on all sorts of shapes. The actual sphericity of the particles greatly differs from 1.
- The particles were injected very close to each other, to achieve similar heating and momentum transport conditions for both of them. In this way, the shrinkage effect can be quantified and compared.
- The model does not take into account the vapour evolution from the discrete phase, as this would slow down the simulation significantly. The mass sources though are calculated by the code, however they are not loaded in the simulation and not released in the computational domain. The inclusion of the tiny amount of mass source of vapours that are produced in each time-step has a major impact in the computational time of a 3-D simulation like the one performed in this study.

5.3.3 Results & discussions

Bed hydrodynamics and particle positions

Figure 5.22 illustrates the hydrodynamics of the fluidised bed at different simulation times together with the positions of the particles. The particles cannot be noticed at the first two snapshots (0.5 – 1.5 seconds contours), due to the formation and evolution of a large bubble close to the injection point. Also, the velocity magnitude vectors of nitrogen are plotted to illustrate the motion and velocity of nitrogen inside the bed, since it plays a significant role in the heat and momentum transport to the biomass particles. For the first 0.5 seconds of the simulation the bed is fluidised without the biomass particles injected in it. Since the sand has gained some velocity, the biomass particle are injected and momentum is transferred from the fluidised sand to the particles.

As we can see, a big bubble has been formed surrounding the injection point at 0.5 seconds and the two particles are immersed into the bubble. Thus, at the early stages of the simulation the momentum and heat is mainly transferred from nitrogen and not the sand. As the simulation progresses, the bubbles decrease in size and the biomass particles have moved on to the surface of the bed and close to the front wall and stayed there for the rest of the 2 seconds of the simulation.

From the simulation point of view, the injection of the particles at 0.5 seconds of fluidisation is a good choice since the sand and nitrogen have gained some velocity

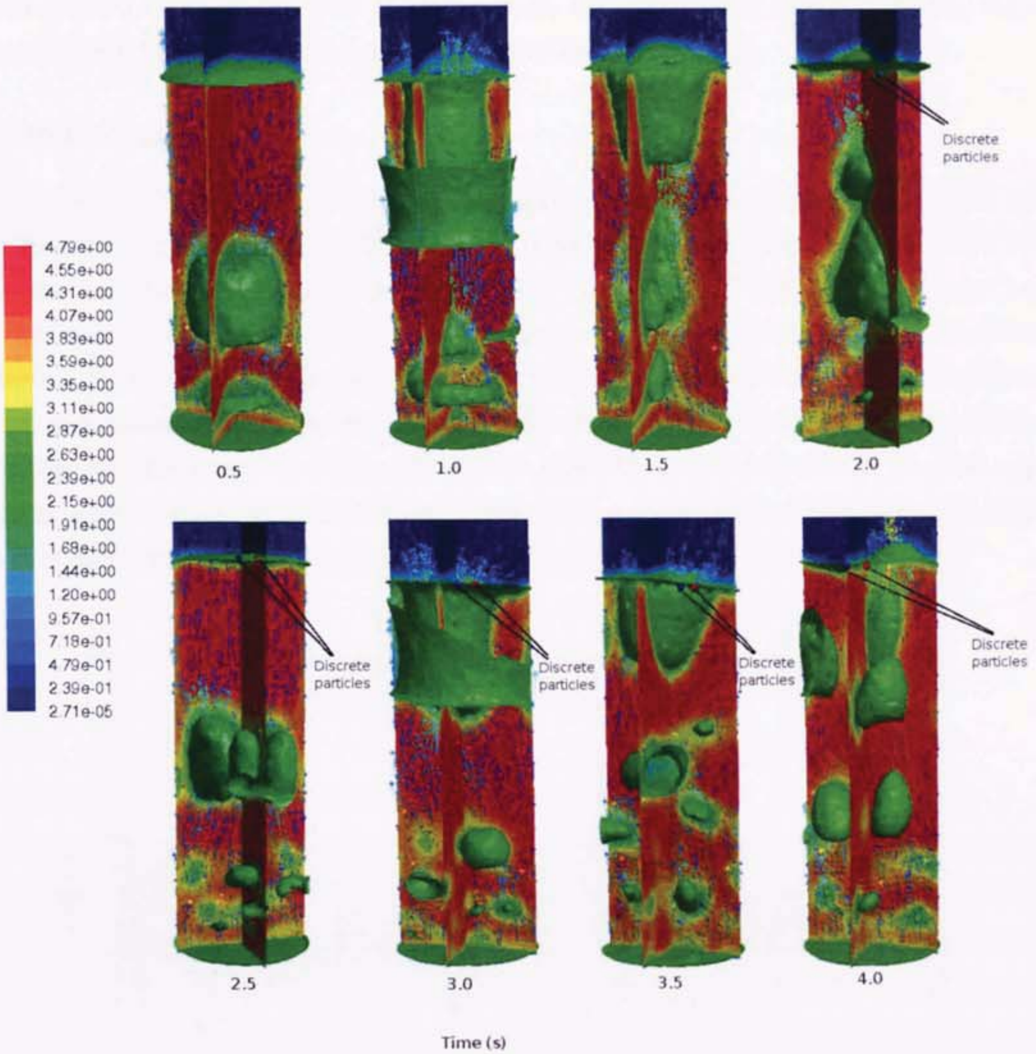

Figure 5.22: Fluidised bed hydrodynamics with particle positions. The particles are covered by the bubbles at 0.5, 1 and 1.5 seconds . Nitrogen velocity magnitude vectors are also visible.

in all directions and the interactions between the bubbling bed and the discrete particles can be quantified. It also reduces the computational time significantly. However, from the process optimisation point of view, the injection of the particles should wait for some seconds until the bed has reached a more stable fluidised state and the solids distribution is more homogeneous. As we can see the diameter of the bubbles formed at the initiation of the fluidisation greatly exceeds the ones that follow in the next seconds. This is the main reason that the particles have been pushed close to the wall of the reactor, something that makes difficult their entrainment from the reactor after they have been pyrolysed.

Particle dynamics

The velocity of the particle is calculated by integrating in time the equation of motion for discrete particles (eqs. 3.76 and 3.77), and their new position is illustrated by the red and blue spheres inside the reactor (fig. 5.22). The particle's position in the reactor is a result of the heat transfer and phase change due to reaction effects. Different heat transfer rates will result in different biomass degradation rates and consequently different particle properties in time. The density drop of the particle will differ and the drag and virtual mass forces exerted on the particle will significantly change. The model can predict the particle position inside the reactor, as it is subjected to pyrolysis, taking all of these effects into account.

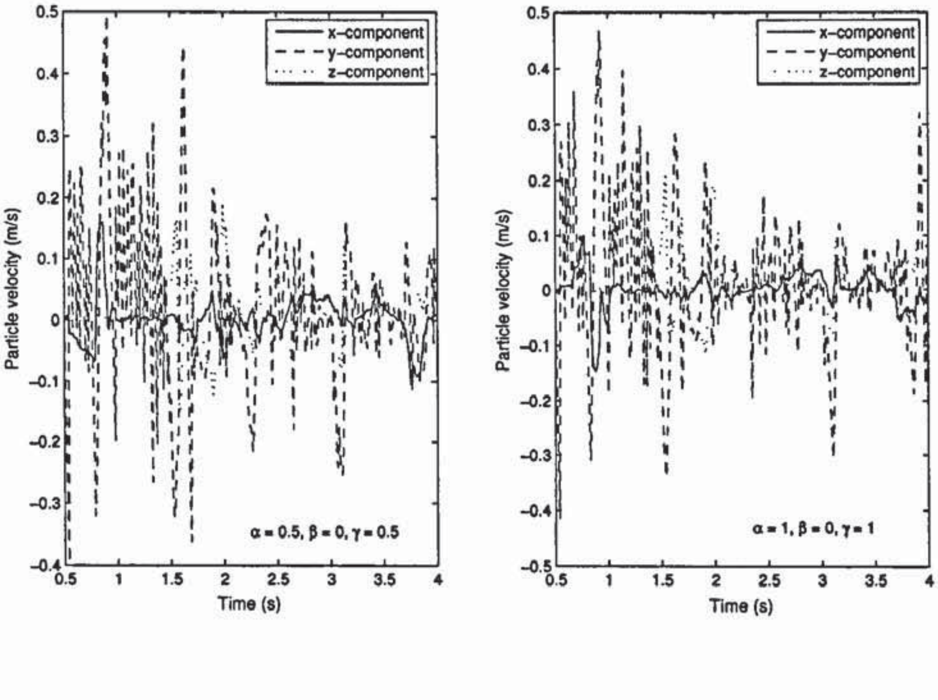

Figure 5.23: Velocity components of particles with different shrinkage conditions

Fig. 5.23 illustrates the velocity components of the particles as they move inside the reactor. In section 3.4, the various parameters that affect the motion of the discrete particles were discussed and it is really obvious that the most important physical ones are the diameter of the particles and their density, since they highly define the drag, virtual mass, gravitational and buoyant forces. In fig. 5.23 we cannot easily distinguish if the shrinkage of the particles plays an important role in the development of their motion. However it can be claimed that the particle with the higher shrinkage conditions ($\alpha = 0.5, \beta = 0, \gamma = 0.5$)appears to have higher velocities especially in the y-z direction than the less shrinking one ($\alpha = 1, \beta = 0, \gamma = 1$). At some points the velocity difference of the particles can exceed $0.1m/s$ as in the situation of the 1.7 seconds of simulation.

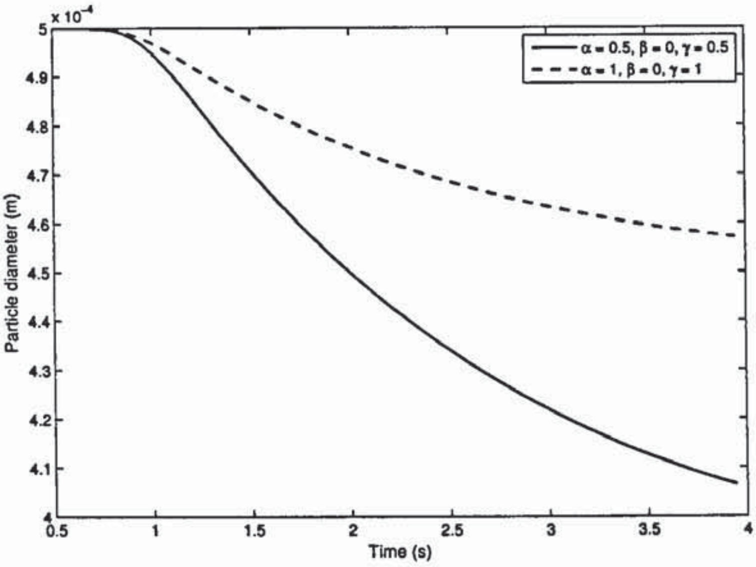

Figure 5.24: Reduction in particle diameters during pyrolysis due to shrinkage

The reason for this, since almost identical momentum is transferred to both particles, is the different reduction in diameter and density of the two particles due to shrinkage. Figure 5.24 shows the reduction in the diameter of the particles because of the different shrinkage conditions and we can see that the final difference is close to $50\mu m$. The decrease in the diameter of the particle affects the velocity response time (eq. 3.65) and makes the particle more vulnerable to fluid velocity fluctuations. Also, fig. 5.25 shows the change of particle volumes and densities with time. We can see that the particles result in almost identical densities at the end of the simulation with different volumes. This means that the mass of the products produced during pyrolysis was proportional to the volume occupied by the particles. However, the small size of the particles does not allow us to to easily estimate the effect of shrinkage on the dynamics of the particles, since the dimensional differences

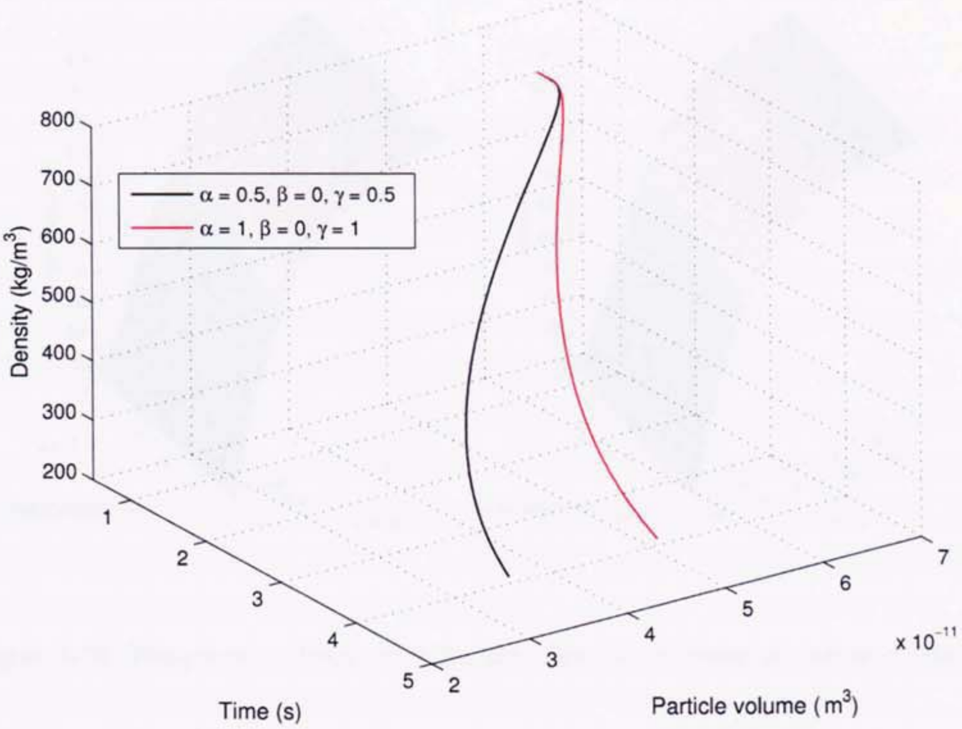

Figure 5.25: Reduction in particle volume and density during pyrolysis due to shrinkage

are in the order of microns. As a general conclusion someone could argue that shrinkage has a negligible effect on particle dynamics in the sub-millimeter scale.

Heat transfer & product yields

Figure 5.26 shows the temperature distribution inside the two pyrolysing biomass particles. We can see that the particles have reached the reactor temperature in almost 0.5 seconds, something which is typical for the heat transfer rates that the fluidised beds provide. The temperature gradients inside the two particles are almost identical, since the particles will start degrading after their temperature has reached $\approx 400^oC$. The temperature at the surfaces and centres of the two particles can be seen on fig. 5.27 and notice that minor differences occur in the heating rates of the two particles.

The heat transfer coefficient for both particles at different times is shown in fig. 5.28. The points that the heat coefficient is reduced is when the particle finds itself

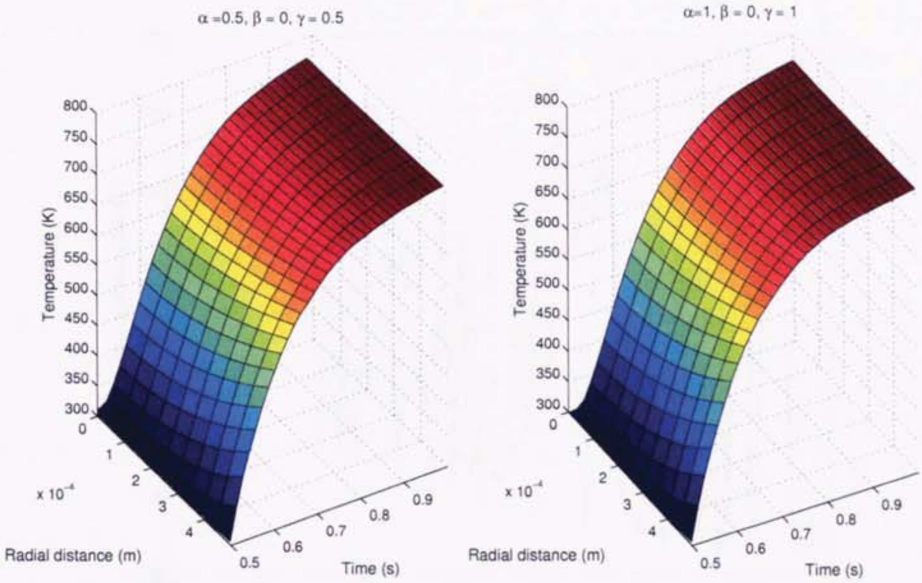

Figure 5.26: Temperature distribution for particles with different shrinkage conditions

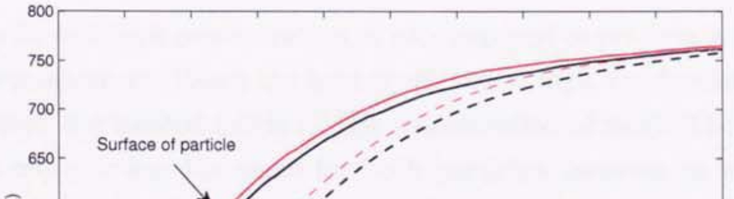

Figure 5.27: Surface and centre temperatures for particles with different shrinkage conditions

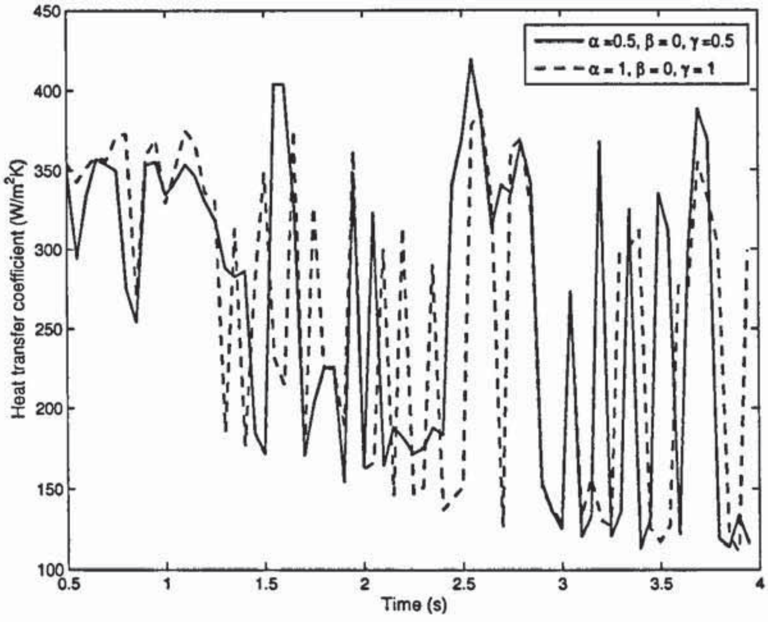

Figure 5.28: Heat transfer coefficient for particles with different shrinkage conditions

in a low velocity but high concentration of nitrogen and convection is the dominant heat transfer mechanism. When the heat coefficient is high, conduction is dominant and the particles are located inside a high concentration of sand. The heat transfer coefficient is more or less the same for both particles, however as we are getting to the half and towards the end of the simulation the heat transfer coefficient for the highly shrinking particle seems to be slightly higher than the less shrinking one. This obviously occurs because the heat transfer coefficient depends on the physical parameters of the particle such as density and consequently mass and surface area. These differences can be up to $\approx 40W/m^2K$ towards the end of the simulation. This effect though plays a negligible role in the degradation of the particle because at the time that it happens, the particles have already reached the temperature of the reactor and the surface heat transfer coefficient cannot control their rate of degradation. The rapid heating that usually occurs in fluidised beds and the small size of the particles that result in a very small Biot number (in this case for an average heat transfer coefficient of $250 - 300W/m^2K$, $Bi \approx 0.174$), causes the particles to be rapidly heated with negligible heat transfer resistance. The fact that the particle will start to react at $\approx 400^oC$ makes the effect of the heat transfer

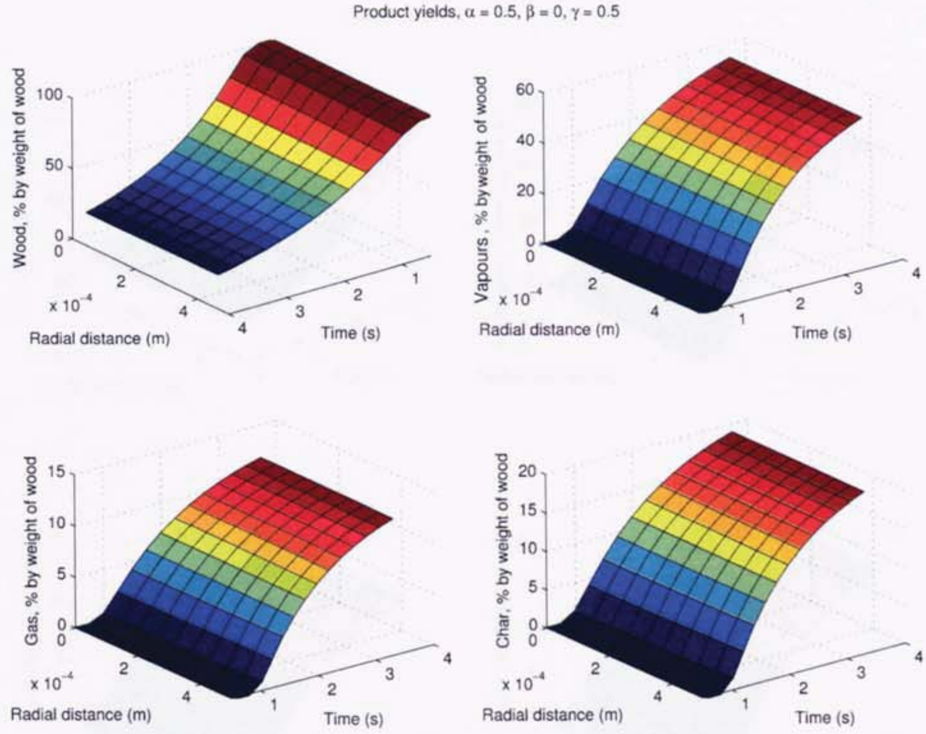

Figure 5.29: Product yields for shrinking conditions ($\alpha = 0.5, \beta = 0, \gamma = 0.5$)

coefficient and shrinkage even less intense. As it is shown in figs. 5.26 and 5.27 the particles have reached a uniform temperature distribution along their radius due to their small size, when the surface temperature has reached $\approx 673K$.

Figures 5.29 and 5.30 show the radial distribution of the products. We can see that the different shrinkage conditions do not have a significant impact on the product yields and pyrolysis time of the particles. The differences on the product yields cannot exceed 1% in any case. Thus, the pyrolysis of thermally thin particles where the resistance to the internal heat transfer is very small compared to the external one, results to small residence times of volatiles inside the particle and secondary reactions have minor impact to product yields. The flat profile of the radial product distribution is due to the small Biot number of the particles, which resulted in a relatively uniform temperature distribution. In both cases the wood concentration was decreased to $\approx$ 19% by its initial weight. Vapour yields were as high as $\approx$ 51%, while gas and char yields $\approx$ 11% and $\approx$ 19% by weight of wood

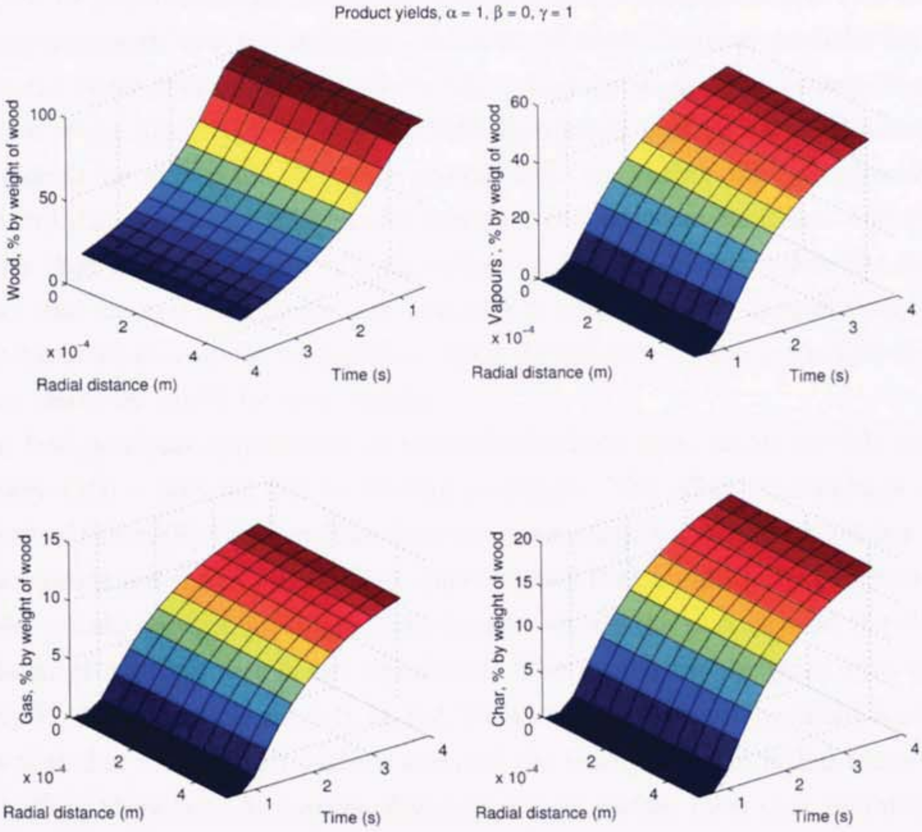

Figure 5.30: Product yields for shrinking conditions ($\alpha = 1, \beta = 0, \gamma = 1$)

respectively. According to [138] the same reaction kinetics scheme, without taking into account the secondary reactions, would produce yields of $\approx 23\%$ char, $\approx 13\%$ gas and $\approx 64\%$ vapours, for complete (100%) biomass degradation at $773K$. Therefore, the yields produced in the simulation are pretty similar with those produced by the single particle models in the literature, since complete degradation of the particle would result to almost identical percentages. The shrinkage of the particles can also be seen on the product distribution illustrated in figs. 5.29, 5.30.

5.3.4 Conclusions

The effect of biomass shrinkage inside a bubbling fluidised was modelled and significant conclusions could be made.

It can be concluded that shrinkage does not have a significant effect on the momentum transport from the bubbling bed to the discrete biomass particles for small sizes in the order of $500\mu m$. The effect of shrinkage on momentum transport can be neglected when fluidised beds operate with such small particle sizes. However, the same cannot be stated for shrinkage parameters that shrink the particles close to their total disintegration. The model excluded this extreme condition and studied particles that shrink until half of their initial volume. If someone takes into account the fact that the specific reactor uses particles of approximately $350\mu m$ then the situation becomes even more insignificant since the relative volume reduction between the two particles would be even smaller.

For fast pyrolysis applications in lab-scale fluidised beds, small particle sizes are necessary $(350 - 500\mu m)$ due to feeding problems. The effect of shrinkage on the pyrolysis of thermally thin particles does not have a significant impact neither on the product yields nor the pyrolysis time. Due to small Biot number, the progress of the reaction is only dependent on the heat transfer inside the particle and the effect of the chemical reaction rate is not significant. The results highly agree with already developed single particle models in the literature [93, 106]. The main reason for this is that due to the small particle size and the nearly uniform radial temperature distribution, there is no formation of an active char surface layer that would have an impact on the final bio-oil yields. The case would not be the same in the thermally thick regime where the temperature difference between the surface and the centre of the particle is significant. The faster progress of the reaction at the surface creates an active char layer which catalyses the vapours flowing at the inner structure of the particle and favours further gas and char formation. As stated above for the momentum transport case, the actual size of the particles used in the specific reactor comes close to $350\mu m$, something that would make the heat transfer characteristics even less susceptible to shrinking conditions.

The model did not consider extreme cases, such as shrinking conditions close to total disintegration of the particles, something that has been studied extensively in the literature. This case would be expected to derive different momentum transport prediction since the diameter of the particle would have been almost eliminated and entrainment will become easier. However, minor differences are expected on the heat transferred to the particle, since the decomposition of biomass starts approximately when the particle has reached the temperature of the reactor. Thus, the volumetric product yields are expected to be similar.

Computational fluid dynamics models can give important information regarding the overall process of fast pyrolysis. They can efficiently used to derive important conclusions in the industrial sector, regarding the design and optimisation of bubbling fluidised bed reactors by deeply understanding the factors that highly influence the process.

5.4 Modelling the effect of particle size on bed-to-surface heat transfer

In this case study the fluid - particle interaction and the impact of different heat transfer conditions on pyrolysis of biomass inside a $150g/h$ fluidised bed reactor is modelled. Two different size biomass particles ($350\mu m$ and $550\mu m$ in diameter) are injected into the fluidised bed. The different size of the particles will result in different heating rates and conditions since the $350\mu m$ particle is smaller than the sand particles in the reactor ($440\mu m$), while the $550\mu m$ is larger. The bed-to-surface heat transfer for the $550\mu m$ particle case is calculated according to the penetration theory of Mickley and Fairbanks [78] and for the case of $350\mu m$ particle according to the findings of Collier et al. [81] for smaller diameter particles than that of the fluidised bed. Conductive heat transfer is assumed for the larger biomass particle ($550\mu m$) inside the bed, while biomass-sand contacts for the smaller biomass particle ($350\mu m$) were considered unimportant. The Eulerian approach is used to model the bubbling behaviour of the sand, which is treated as a continuum, as described in section 4.1. Biomass reaction kinetics are modelled according to the two-stage, semi-global model shown in fig. 2.8 which takes into account secondary reactions, with kinetic constants given at table 3.3. The particle motion inside the reactor is computed using drag laws, dependent on the local volume fraction of each phase.

In the case that the biomass particle diameter is larger than the diameter of the sand particles in the bed the heat transfer coefficient is calculated using the penetration theory given by eq. 3.101. However, if the diameter of the biomass particle is smaller than the diameter of the sand particles then a modified Nusselt number based on the minimum fluidising velocity is used to calculate the heat transfer coefficient according to the findings of Collier et al., [81].

$$Nu = 2 + 0.9\mathrm{Re}_{\mathrm{p,mf}}{}^{0.62}(d_p/d_{bed})^{0.2}, \tag{5.7}$$

where

$$\mathrm{Re}_{\mathrm{p,mf}} = \frac{\rho_g U_{mf} d_p}{\mu_g}. \tag{5.8}$$

5.4.1 Model parameters

The simulation parameters are shown in table 5.4.

Property	Value	Comment
Biomass density, ρ_w	$700 kg/m^3$	Wood
Biomass particle diameter, d_p	$550\mu m$	Fixed
	$350\mu m$	Fixed
Biomass specific heat capacity, C_{p_w}	$1500 J/kgK$	Wood
Char specific heat capacity, C_{p_c}	$1100 J/kgK$	Char
Biomass thermal conductivity, k_w	$0.105 W/mK$	Wood
Char thermal conductivity, k_c	$0.071 W/mK$	Char
Superficial velocity, U_0	$0.3 m/s$	$\approx 4U_{mf}$
Gas density, ρ_g	$0.456 kg/m^3$	Nitrogen ($773K$)
Gas viscosity, μ_g	$3.44 \times 10^{-5} kg/ms$	Nitrogen ($773K$)
Gas specific heat capacity, $C_{p,g}$	$1091.6 J/kgK$	Nitrogen ($773K$)
Gas thermal conductivity, k_g	$0.0563 W/mK$	Nitrogen ($773K$)
Solids particle density, ρ_s	$2500 kg/m^3$	Sand
Sand temperature	$773K$	Uniform
Sand specific heat capacity, $C_{p,s}$	$835 J/kgK$	Fixed
Sand thermal conductivity, k_s	$0.35 W/mK$	Fixed
Mean solids particle diameter, d_s	$440\mu m$	Uniform distribution
Restitution coefficient, e_{ss}	0.9	Value in literature
Initial solids packing, ε_s	0.63	Fixed value
Static bed height	$0.08m$	Fixed value
Bed width	$0.04m$	Fixed value
Heat of reaction	$\Delta H = -255 kJ/kg$	Koufopanos et al., [142]

Table 5.4: Simulation parameters for the effect of particle size on bed-to-surface heat transfer

For the implementation of the model certain parameters have been quantified and assumptions made, in order to provide, as much as possible, an insight to the fast pyrolysis process in bubbling beds.

- The particles used in the simulation were assumed to be totally spherical, whereas the particles used in experiments can be found on all sorts of shapes. The actual sphericity of the particles greatly differs from 1.

- The particles were injected very close to each other, to achieve similar initial heating and momentum transport conditions for both of them.
- The model does not take into account the vapour evolution from the discrete phase, as this would slow down the simulation significantly. The mass sources though are calculated by the code, however they are not loaded in the simulation and not released in the computational domain. The inclusion of the tiny amount of mass source of vapours that are produced in each time-step has a major impact in the computational time of a 3-D simulation like the one performed in this study.

5.4.2 Results & discussions

Bed hydrodynamics and particle positions

Figure 5.31 illustrates the hydrodynamics of the fluidised bed at different simulation times together with the positions of the particles. Whenever the particles are not visible, are covered by the formed bubbles. Also, the velocity magnitude vectors of nitrogen are plotted to illustrate the motion and velocity of nitrogen inside the bed, since it plays a significant role in the heat and momentum transport to the biomass particles. For the first second of the simulation the bed is fluidised without the biomass particles injected in it. Since the sand has gained some velocity, the biomass particles are injected and momentum is transferred from the fluidised sand to the particles.

Examining fig. 5.31, we can see that at the time that the particles are injected, a small bubble has been formed just underneath them, which eventually carries them to the top of the bed. At the time that the particles reach the unstable splash zone of the fluidised bed, cannot be entrained since their terminal velocity ($U_{t,350} = 0.94m/s$ and $U_{t,550} = 1.72m/s$ at a density of $700kg/m^3$) is much higher than the velocity of nitrogen at the freeboard of the reactor (range of $0.47 - 0.71m/s$ at the centre of the reactor, which gradually tends to $0m/s$ approaching the wall), and consequently fall back to the bed. The particles stay close to the splash zone of the bed, while the formed bubbles at the central axis of the reactor push them towards the wall of the reactor on the following seconds. As pyrolysis of the particles takes place and density drops (fig. 5.32), the smaller particle ($350\mu m$) is entrained at approximately 6 seconds of simulation (5 seconds residence time). The entrainment of the particle is also a strong function of the radial position of the particle inside the reactor, since

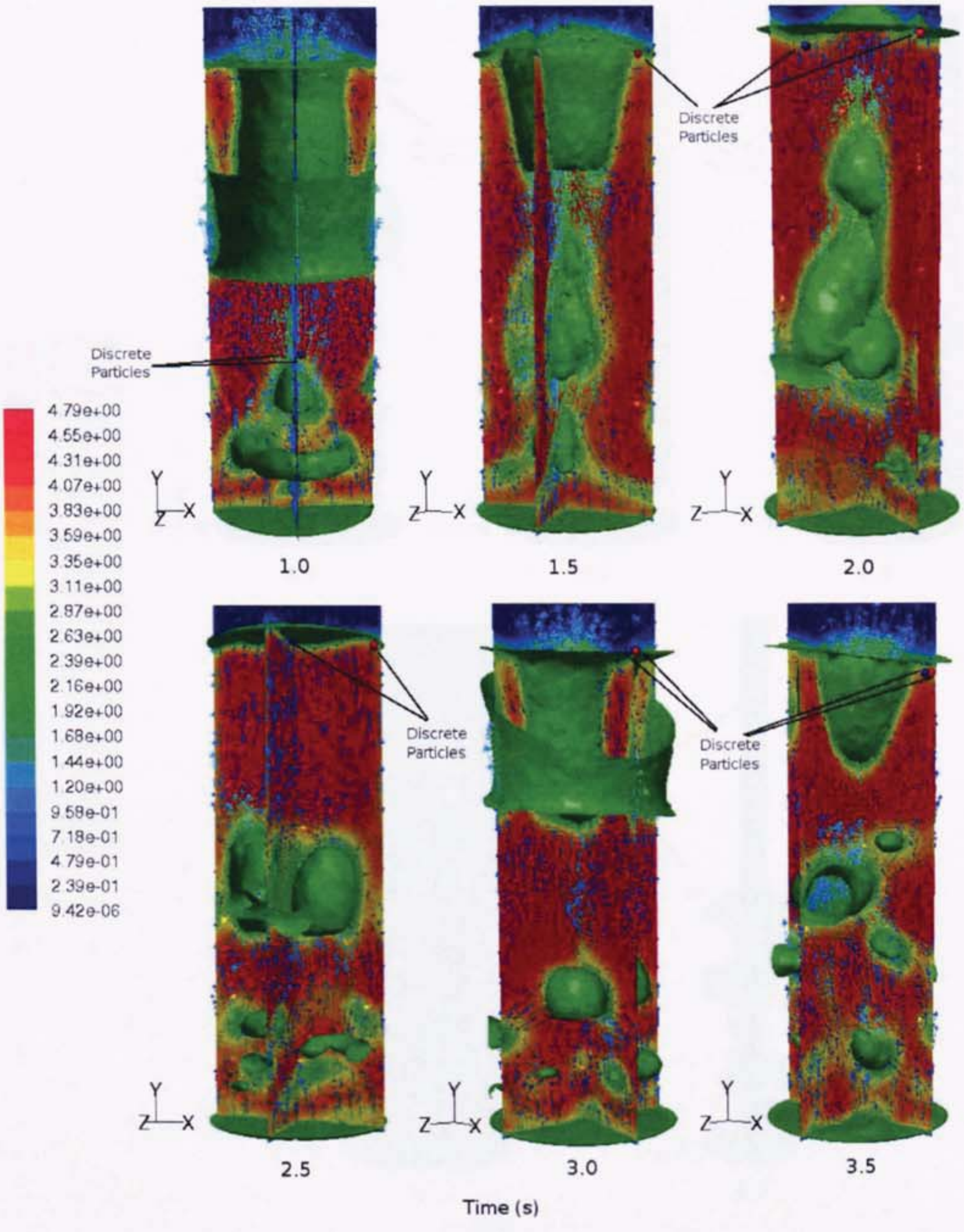

Figure 5.31: Bed hydrodynamics with particle positions and vectors of nitrogen velocity magnitude. Blue particle: $350\mu m$, Red particle: $550\mu m$.

nitrogen velocities close to the wall tend to be much lower than at the centre. At the time of entrainment, the density of both particles has dropped to approximately

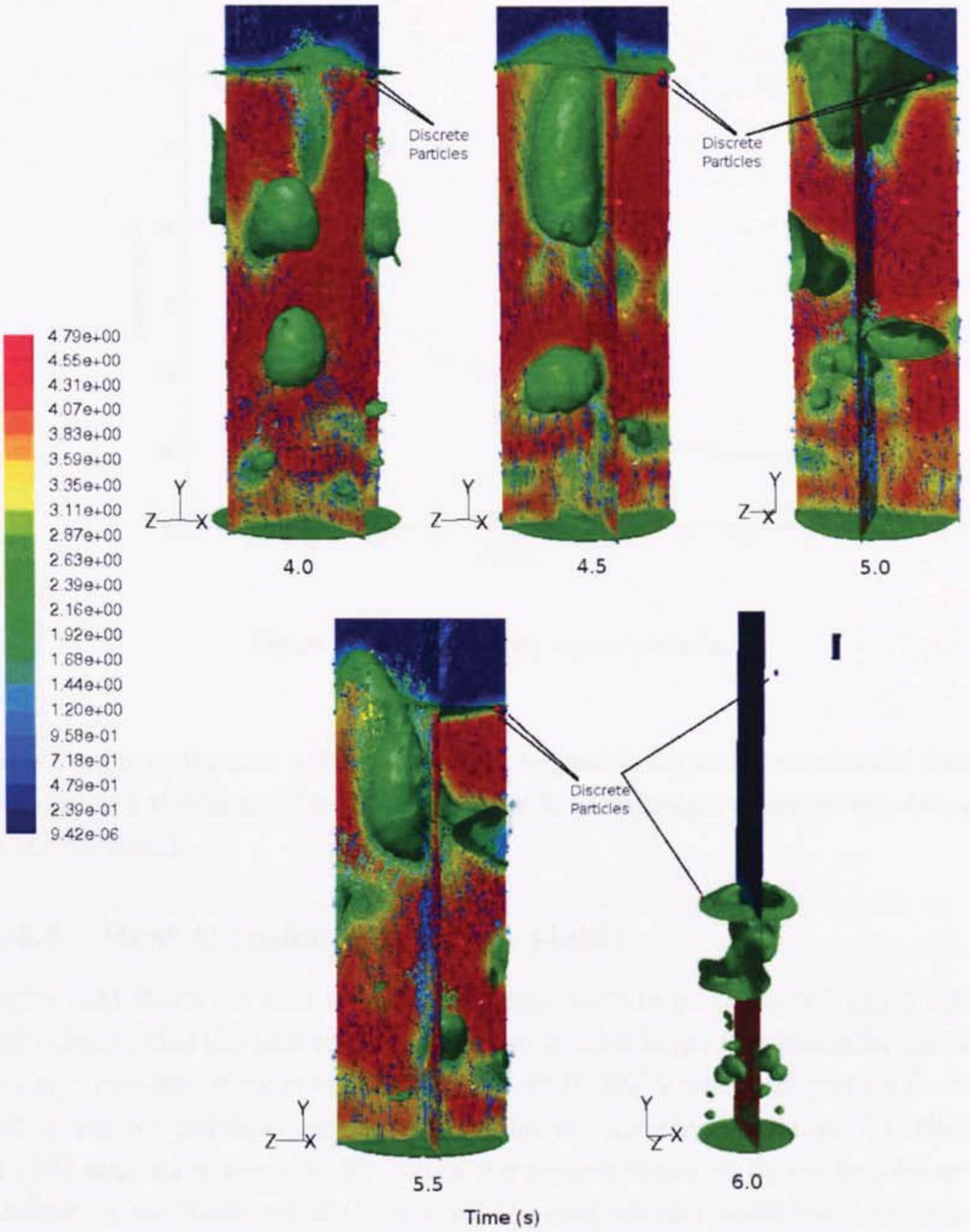

Figure 5.31: (Cont'd) Bed hydrodynamics with particle positions and vectors of nitrogen velocity magnitude. Blue particle: $350\mu m$, Red particle: $550\mu m$.

$190kg/m^3$. The respective terminal velocities for this density are $U_{t,350} = 0.31m/s$ and $U_{t,550} = 0.62m/s$, something that makes the entrainment of the smaller particle

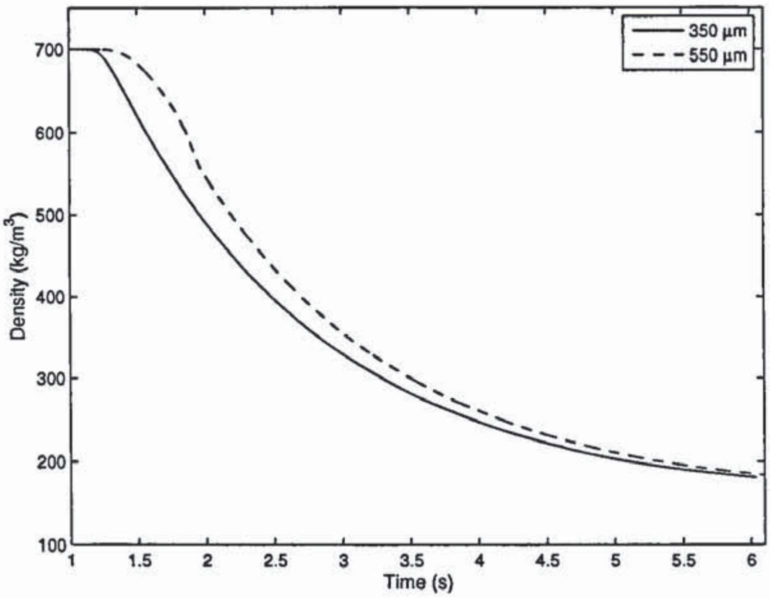

Figure 5.32: Density drop of the particles

easier even from the near wall area. The larger particle cannot be entrained if it does not approach the centre of the reactor, where larger nitrogen velocities are observed at the freeboard.

5.4.3 Heat transfer & product yields

Figure 5.33 shows the heat transfer coefficient for both particles. We can immediately observe that the heat transfer coefficient is much larger for the smaller particle, having a constant value of approximately $\approx 310W/m^2K$ when the particle finds itself among the fluidised sand particles. This is what the correlation of Collier et al., [81] suggests in equation 5.7. When the particle is carried by the bubbles or by nitrogen in the freeboard of the reactor, the heat transfer coefficient increases up to approximately $\approx 500W/m^2K$ due to convection effects from the higher velocity nitrogen in that area.

However,the heat transfer coefficient is smaller for the larger particle when finds itself among the fluidised sand (approximately $\approx 150W/m^2K$) and conductive effects are assumed to be dominant, with a maximum value of approximately $\approx 310W/m^2K$ at the time of injection. The heat transfer coefficient becomes greater (approxi-

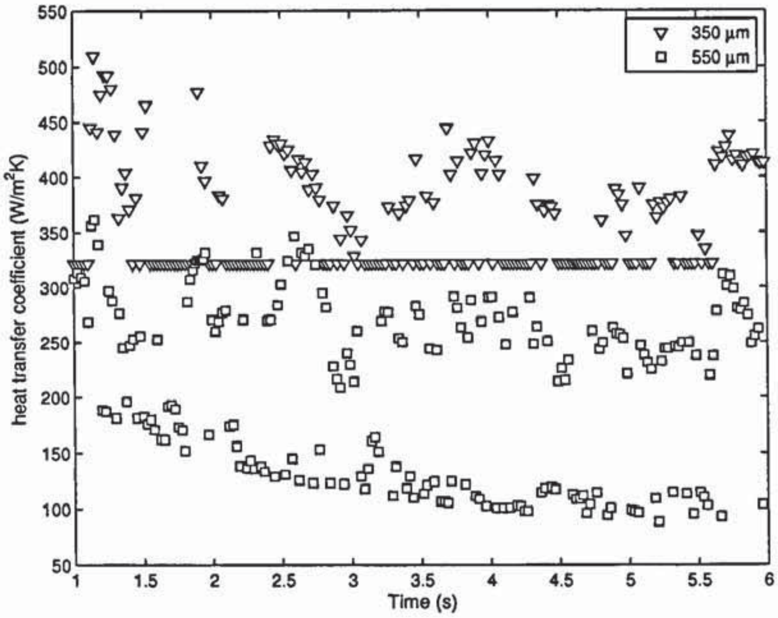

Figure 5.33: Heat transfer coefficient for both particles

mately $\approx 300W/m^2K$) when the particle is carried by the bubbles or transferred to the splash zone of the bubbling bed where convective effects by the high velocity nitrogen is dominant.

The low values of heat transfer coefficient of the larger particle are due to the fact, that at the time of injection the bubbles in the bed have become the dominant phase. Therefore, the properties of the emulsion phase (eqs. 3.102 and 3.103) due to high voidage variations at the heat transfer surface have been gas-dominated. Also, the short residence time of the emulsion packets at the heat transfer surface makes the gas surface layer at the heat transfer area increasingly important and the emulsion model fails to predict correctly the heat transfer coefficient.

Figure 5.34 shows the temperature at the surface and the centre of the particles until they reach the temperature of the reactor. Due to the small Biot number of the particles ($Bi_{350} \approx 0.22$, $Bi_{550} \approx 0.17$, using the thermal conductivity of biomass), something that was shown on the previous case studies as well, the small temperature gradient inside the particle does not affect pyrolysis products, resulting in a uniform radial distribution of product yields. As fig. 5.34 shows the temperature difference at the surface and the centre of the particles are not significant, especially at pyrolysis

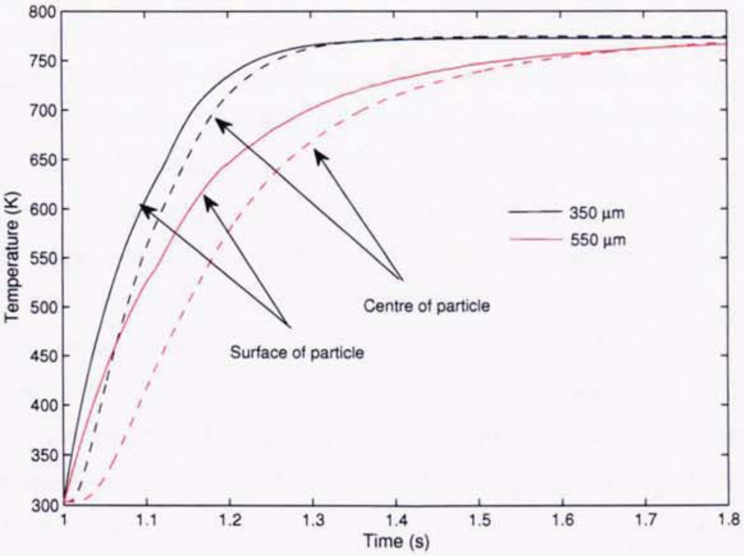

Figure 5.34: Temperature rise at the surface and the centre of the particles

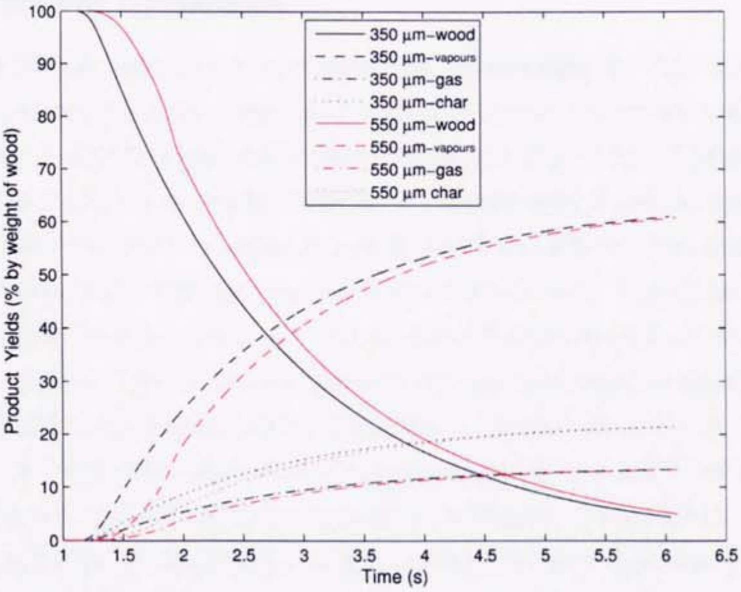

Figure 5.35: Product yields for both particles

elevated temperatures ($> 400^oC$) and thus the product yields shown at fig. 5.35 are given averaged in the volume of the particle and not radially distributed.

The biomass particles were almost totally pyrolysed in the 6 seconds of the simulation (5 seconds of pyrolysis). As it is shown on fig. 5.35 the different heat transfer rates resulted in different biomass degradation rates which tend to converge towards the end of the simulation. However, the final product yields seem to be similar in this case, since the smaller particle was not quickly entrained due to its movement close to the wall. It is obvious though that the degradation of the smaller particle started faster and its rate was reduced towards the end of the simulation due to the low unreacted biomass content left on the particle. A that point the larger particle was reacting faster and the final yields are almost identical. Another factor that influences the product yields is the small size of the biomass particles, resulting in a relatively uniform temperature distribution inside the particles. Thus there is not a thick moving layer of char formed at the surface of the particle that would significantly affect the secondary reactions. Therefore, the products for both particles are expected to be identical at the complete degradation of the particle. In this case, the pyrolysis of both particles resulted to approximately $\approx 5\%$ of wood left, $\approx 61\%$ of vapours, $\approx 21\%$ char and $\approx 13\%$ of gas.

5.4.4 Particle dynamics

The velocity of the particles is calculated by integrating in time the equation of motion for discrete particles (eqs. 3.76 and 3.77), and their new position is illustrated by the red and blue spheres inside the reactor (fig. 5.31). The position of the particles in the reactor is a result of the heat transfer and phase change due to reaction effects. Different heat transfer rates will result in different biomass degradation rates and consequently different particle properties in time. The density drop of the particle will differ and the drag and virtual mass forces exerted on the particle will significantly change. The model can predict the particle position inside the reactor, as it is subjected to pyrolysis, taking all of these effects into account.

Figure 5.36 illustrates the velocity components of the particles as they move inside the reactor. In section 3.4, the various parameters that affect the motion of the discrete particles were discussed and it is really obvious that the most important physical ones are the diameter of the particles and their density, since they highly define the drag, virtual mass, gravitational and buoyant forces. Fig. 5.36 shows that the velocities of the two particles are almost identical most of the simulation time

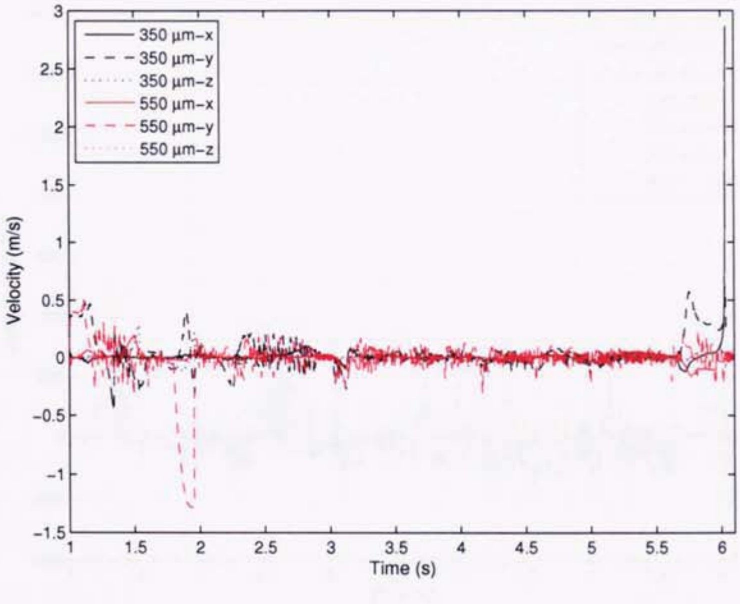

Figure 5.36: Velocity components of the particles

except in two cases. Close to 1.8 seconds of simulation there is a sudden negative y-velocity increase for the larger particle due to a large amount of drag force shown on fig. 5.37. This is possibly due to the bubble eruption shown on fig. 5.31 at 1.5 seconds, which created a downward flow of solids that tried to sink the large particle into the bed. The high volume fraction of sand created this big amount of drag force to the particle. Also, at the end of the simulation the smaller particle appears to have an increase on its x and y velocity components as it is being ejected from the bed and accelerates towards the outlet of the reactor. This is caused due to its large density drop and its small diameter which made the particle easy to be entrained from the fluidising gas even from a region close to the wall, where nitrogen velocities tend to be lower.

Figures 5.37 and 5.38 show the drag and virtual mass force exerted on each particle at different times. As we can see the drag force is the dominant momentum transport mechanism, where its values are far more increased than those of the virtual mass. The virtual mass force plays a relatively insignificant role and it can be considered significant only when the particles are carried by the sand due to high density differences between them and especially when they find themselves in the unstable splash zone, where high fluid velocity gradients occur due to bubble

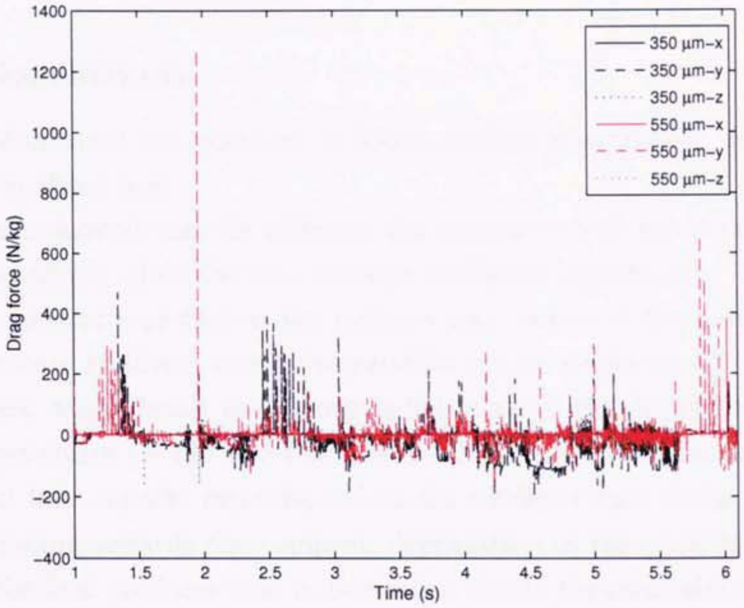

Figure 5.37: Drag force per unit mass

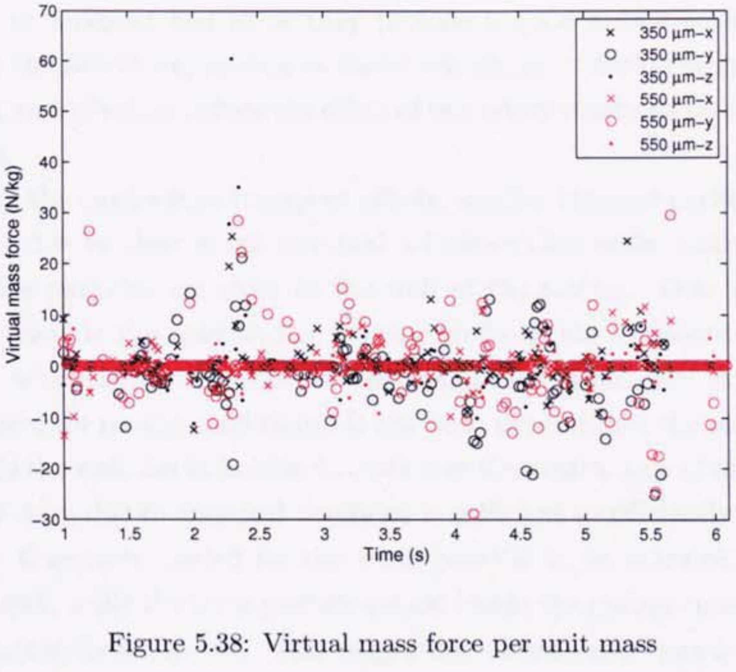

Figure 5.38: Virtual mass force per unit mass

eruption which cause intense sand recirculation.

5.4.5 Conclusions

The effect of different size particles on bed-to-surface heat transfer was modelled in a bubbling fluidised bed.

The results showed that the different size particles which result in different heat transfer mechanism affect the heat transfer coefficient significantly. This results in different temperature profiles at the surfaces and centres of the biomass particles. The temperature gradients inside the particles can be neglected due to their small Biot numbers, which result to uniform radial product distribution at elevated pyrolysis temperatures ($> 400^oC$). The final product yields for different size particles and different heat transfer rates depend on the residence time of the particle in the reactor. Tending towards the complete degradation of the particles, as pyrolysis continues, the final products tend to be similar, due to the small size of the particles and the limited catalytic action of the char layer, due to insignificant temperature gradients. If the particles were entrained close to 2 seconds of pyrolysis (3 seconds of simulation) then a considerable difference of about 4% vapours would be noticeable. According to the study smaller particles would be preferred for fast pyrolysis applications in fluidised bed since they provide a good heat transfer mechanism according to the literature, as well as easier entrainment during their degradation. Also, smaller particle sizes reduce the effect of secondary reactions resulting in higher bio-oil yields.

Regarding the momentum transport effects, smaller biomass particle sizes would be preferable due to their small terminal velocities that make entrainment easier even when the particles are close to the wall of the reactor. Due to the laminar nature of the flow in the reactor, the velocity profile in the freeboard of the reactor is parabolic, which means that the velocity magnitude of nitrogen close to the wall approaches zero for no-slip conditions. It has been noticed that the particles tend to move towards the wall due to bubble formation at the central axis of the reactor until their density drop due to chemical reactions is sufficient to efficiently entrain them. In this case, 6 seconds needed for the small particle to be entrained while it was close to the wall, while the large particle stayed inside the reactor incapable of being efficiently ejected from the bed. This magnitude of residence time is inappropriate for fast pyrolysis since the presence of char particles inside the bed for so long, greatly affects the bio-oil conversion since it contributes to the extra-particle catalysis of pyrolysis vapours and favours further formation of noncondensable gases.

In this study, the model was executed until at least one of the particles is properly entrained from the reactor no matter the computational time needed to achieve that. Important conclusions were derived about the optimum particle sizes regarding both heat and momentum transport. It was shown that CFD can give a very good insight of the process, highly predicting the correct biomass conversion since the results highly agree with many single particle models and experimental data that can be found on the international literature.

Chapter 6

Conclusions

6.1 Research summary & conclusions

The thesis presented the development and application of a computational model for fast pyrolysis in bubbling fluidised bed reactors. The simulation framework used was the commercial finite volume code FLUENT and the model was implemented in the form of a user defined function to account for the heat, mass and momentum transport phenomena occurring in fast pyrolysis. The main idea behind the code development was the creation of a revised momentum transport suitable for simulating the forces acting on discrete particles that are a part of a gas/liquid/solid mixture, since the granular nature of the sand was treated as a continuum. The second part of the computational code, involved the heat transferred from the bubbling bed to the surface of the discrete particles taking into account the presence of the bubbles formed inside it by modifying the mixture viscosity, density, specific heat capacity and thermal conductivity, according to the local mass fraction of the phases as the penetration theory of Mickley and Fairbanks suggests [78]. When the particle was carried only by nitrogen in the freeboard of the reactor the heat transfer coefficient was calculated by the well known Ranz-Marshal correlation [195, 196]. The implementation of the code involved the solution of the heat diffusion equation inside a spherical particle taking into account the enthalpy of reaction of the reacting biomass and the radial distribution of temperature and pyrolysis products was predicted. The model also associated the chemical kinetics of biomass with discrete particles that freely move inside the computational domain of the reactor. The produced vapours were released as mass sources inside the computational domain in order to visualise their interaction with the bubbling bed as well as their residence time.

The innovation of the model basically stands for the first implementation of a computational model that combines fluidised bed hydrodynamics with injection of reacting discrete particles with simultaneous tracking and vapour evolution. All the three phase models that can be found in the literature, as it is mentioned in section 3.5, make certain approximations in the treatment of either the two continuous phases or one continuous and one discrete phase using either the Eulerian-Eulerian approach or the Eulerian-Lagrangian method. In other words, in every simulation two of the phases are combined in a single average phase via interaction terms and then the combined phase interacts with the third phase. In the current model each of the phases is modelled separately using interaction terms to account for interphase interaction and their involvement in the heat and momentum transport is defined according to the local volume fraction of the specific phase. The fact that the discrete phase is able to react and release a third continuous phase inside the domain that is able to interact with the other phases makes the model even more innovative. The complexity of a process such as fast pyrolysis makes the absolute control over every single phase of the reactor a necessity for the development of reliable computational models.

The study showed in section 4.1, that in order to account for the momentum transport phenomena inside the bubbling bed of the reactor, the collisions of the sand grains with the discrete particles have to be replaced with fluid-particle interaction forces such as drag, buoyancy and virtual mass, since the Eulerian approach adopted in the thesis treats the granular phase as a continuum. The study showed that the drag force is the dominant momentum transport parameter with the virtual mass force to play a relatively important role only when the particle was found in side the bubbling bed and especially when the particle was floating in the unstable splash zone of the reactor due to high sand velocity fluctuations because of the bubble eruption. It was also shown that the geometrical approach of the problem resulted in different results. The dominance of 2-D simulations in the literature is in no doubt, however a major defect can be noticed when a third discrete phase is injected in the reactor. Despite the fact that the hydrodynamics of the bed remain almost similar in the 2-D and 3-D cases in the analysis of section 4.1, the loss of hydrodynamic symmetry in the 3-D case, due to sand expansion in the third dimension, resulted in different discrete particle motion inside the reactor, by actually moving it to the exact opposite side of the reactor. This would have a significant effect in reactor design since the bed hydrodynamic similarity between 2-D and 3-D is not the only parameter that defines the efficient operation of the reactor. The study suggests that when a complete process is modelled the 3-D representation and simulations become important and the engineer cannot be totally based on 2-D configurations.

In section 4.2 the actual biomass degradation and heat transfer characteristics were modelled. The simulated particle was chosen to be $500\mu m$ in diameter and totally spherical, something that actually makes it larger than the actual particle size $350\mu m$ used in the reactor. The simulation was left at the 2-D representation to avoid extreme computational delays that would occur by the release of the tiny amount of vapours at the early stages of the biomass pyrolysis. It was found that the temperature gradient inside the particle can be considered insignificant for this particle size even when the Biot number of the particle is higher than 0.1. This is caused by the reaction temperature when it is close to 400^oC and at the instant any temperature difference between the surface and the centre of the particle was smoothed out and thus the radial product distribution becomes uniform. Despite the fact that the application of the model used the complete form of the heat diffusion equation one could easily make the assumption that the particle maintains a uniform temperature and calculate the product yields using an average particle temperature neglecting the heat of reaction and using only the sensible heat of the system. It was also shown that the residence time of the particle exceeds the normal 2 seconds needed for fast pyrolysis and that further degradation is necessary to achieve entrainment. The residence time of the produced vapours comes close to 2 second something that it is desirable for the fast pyrolysis process.

The Gidaspow model was used during the development of the complete fast pyrolysis model to simulate the interaction between sand and nitrogen in the fluidised bed reactor resulting to specific bubble formation and consequently specific momentum and heat transfer characteristics. The models of Syamlal and O'Brien [64] and Wen and Yu [65] were not used, however previous CFD investigations performed at Aston University [62] showed that minor hydrodynamic differences occur with the use of these models. It has to be noted though that their application is simple and does not at all affect the development of the computational model since these models are already defined in the main code of FLUENT and can be easily examined and tested.

The developed model was applied in four different case studies which can be of great help to the chemical engineer in the design and optimisation of fluidised bed reactors for fast pyrolysis. The studies were focused on the effect of particle size on char entrainment, the effects of particle sphericity, the effect of biomass shrinkage as well as the effect of particle size on the bed-to-surface heat transfer coefficient. As a synopsis of all these case studies it can be stated simply stated that small particles are better but not that small. Smaller particles are easier to entrain and they present uniform temperature distribution and they are not affected by the shrinking conditions. However, smaller particles need higher amount of grinding something that increases the cost of the process. By performing simple case studies we can have a look inside the limitations of the process as well as to define the limits of process efficiency.

The case study on the effect of particle size, discussed in section 5.1, just showed the logical outcome. The smaller particles will be entrained easier significantly reducing the residence time of the char particles which highly influence the final bio-oil yield by their catalytic effect on pyrolysis vapours. However, small particle sizes which are easy to entrain may result in poor biomass degradation since their residence time is significantly reduced.

The case study on the sphericity effects, discussed in section 5.2, showed a very interesting result. The particles that may present larger effective diameter and thus higher projected hydrodynamic volume may be easier to entrain depending at the point of injection. Lower volume particles may remain inside the reactor and increase their residence time simply by being pushed towards the walls of the reactor. The low nitrogen velocities that appear close to the wall make entrainment difficult when the particle is ejected from the bed, while bubble formation at the central axis of the bubbling bed do not allow the particle to actually be ejected in the freeboard. However, sometimes nonspherical particles can present good momentum transport behaviour but the heat transferred to them can be peculiar and sometimes inefficient as well as difficult to model. Also, particle shape is difficult and expensive to control at sub-millimeter particle scales.

The biomass shrinkage was discussed in section 5.3. The case was modelled using two different shrinking conditions showing that biomass shrinkage has minor effects on momentum transport, not including the case that biomass shrinkage comes close to total degradation, when it is modelled on such small particle sizes. Even in the case that the particle volume was reduced to almost half of its original volume the particle behaviour did not alter significantly. Also, the effect on heat transfer and product yields was minor since the small size of the particle resulted in almost uniform temperature distribution without an active char layer formed at the surface of the particles. The results would be expected to be different for large particle sizes and the engineer can test the transition cases where shrinkage actually benefits the process by reducing the particle size to a level that the char layer becomes insignificant.

The final case study performed concerned the effect of particle size on the bed-to-surface coefficient (section 5.4). Studies have shown that particle sizes have a great effect on the dominant heat transfer mechanism inside a bubbling bed. The relative diameter of the biomass particle size and the sand particle size also defines the heat transfer coefficient. The study was performed assuming that conductive heat transfer is dominant when the biomass particle size is greater than the sand particle size, while convection was assumed to play a most important role when the opposite was happening. The results showed that the fast pyrolysis process would be benefited from particles with particles smaller in diameter that the bed material since they present better heat transfer characteristics. It was also shown that when spherical particles are considered the whole fast pyrolysis process can last up to 5 seconds where the char particle is entrained. At that time the product yields of the different size char particles do not greatly differ, however at the earlier stages of the process a higher vapour production for the smaller particle can be easily noticed.

As a general conclusion, it can be stated that biomass particles that are smaller than the bed material particles are preferable. As the case studies have shown, this results to a more efficient operation of such kind of reactor. There are many parameters that affect the process of fast pyrolysis and probably the most important one are the actual reactivity of biomass and feedstock properties as well as the way of transferring the heat inside the reactor and consequently to biomass particles. Different kinds of biomass will result in different degradation rates, thus a general conclusion and suggestion is difficult to make. The importance of the model is that it can at least provide a very good insight at the selected process and point out the major limitations and possible design defects for process optimisation as extensively discussed in chapters 4 and 5. Immediate consequences of the application of the model concern the geometrical modification of the reactor as well as the use of smaller biomass particle sizes, something that would certainly have an impact at the cost of the process. CFD tests can also be run to test the limits of fluidisation of the reactor and point out the fluidising velocities at which slugging occurs due to the large size of the bubbles as well as the limits of sand bed expansion. Each optimisation operation will have a certain impact at the cost and applicability of the process, so a carefull treatment of the physical phenomena becomes necessary. CFD models have become a necessary tool in the development chemical plant equipment and as their reliability and applicability grow, the optimisation and efficiency of chemical processes will respond accordingly.

6.2 Recommendations for future work

The current study was focused on the development of a computational model to simulate the fast pyrolysis process in bubbling fluidised beds. Due to computational needs of the study, a great amount of time was lost in the development and application of the model. Several studies could be performed regarding the geometrical modifications of the reactor for process optimisation as well as the application of the model in different kinds of biomass feedstocks. Of course, such an attempt would demand the complete reforming of the code regarding its computational matrices. However, this would be a relatively easy task to fulfil due to the nature of the structure of the code.

As a basic future development regarding fast pyrolysis one could recommend the application of the model in geometrical modifications of the reactors for better heat transfer and momentum transport control as well as the application of such model to examine the scaling effects. It is intelligible that great computational power is necessary for this kind of simulations and the researcher might have to be completely focused on this aspect.

Also, the generalisation of the code to include various reaction kinetics schemes in order to easily simulate and examine different kinds of feedstocks as well as the effect of secondary reactions on final bio-oil yields would be of great importance. The difficulty of such a task is that usually advanced programming abilities are required by the researcher and the cooperation with computer science students may be a necessity. FLUENT could also consider the case of developing a sub-model for their basic simulation platform by taking these factors into account and also to aid the user in the development of even more advanced models with his own user defined functions.

Finally, the restrictions of the application of such model only in pyrolysis can be eliminated by simple modifications on the code structure. Combustion and gasification in fluidised beds can be relatively easily resolved by replacing the computational matrices of the pyrolysis reaction mechanism with the stoichiometric reactions that govern these processes. Again the inclusion of such cases as a sub-model to a unified CFD code would ease the user in the development of even more advanced CFD models and would eliminate the need of high external memory allocations, which have a significant effect on the computational time and needs of such an attempt.

CFD is becoming even more reliable tool as the years of research go by and even in the cases that the process cannot be easily modelled or questions are raised about the modelling reliability, certainly the basic physics and chemistry is there and on can have a very good idea of what is actually happening in the process. Knowledge and experience is always going to be the most important factor in the development and optimisation of every single process and CFD can give the extra information needed or raise the questions for even greater advances in science and technology.

Appendix A

Computational grid generation

Fig. A.1 illustrates the isometric and bottom view of the meshed geometry of the reactor. The grid was used in all the 3-D cases through the model development and all the case studies. The 2-D grid was created in a similar approach as the 3-D one with similar dimensions. Several mesh configurations had been tried and tested

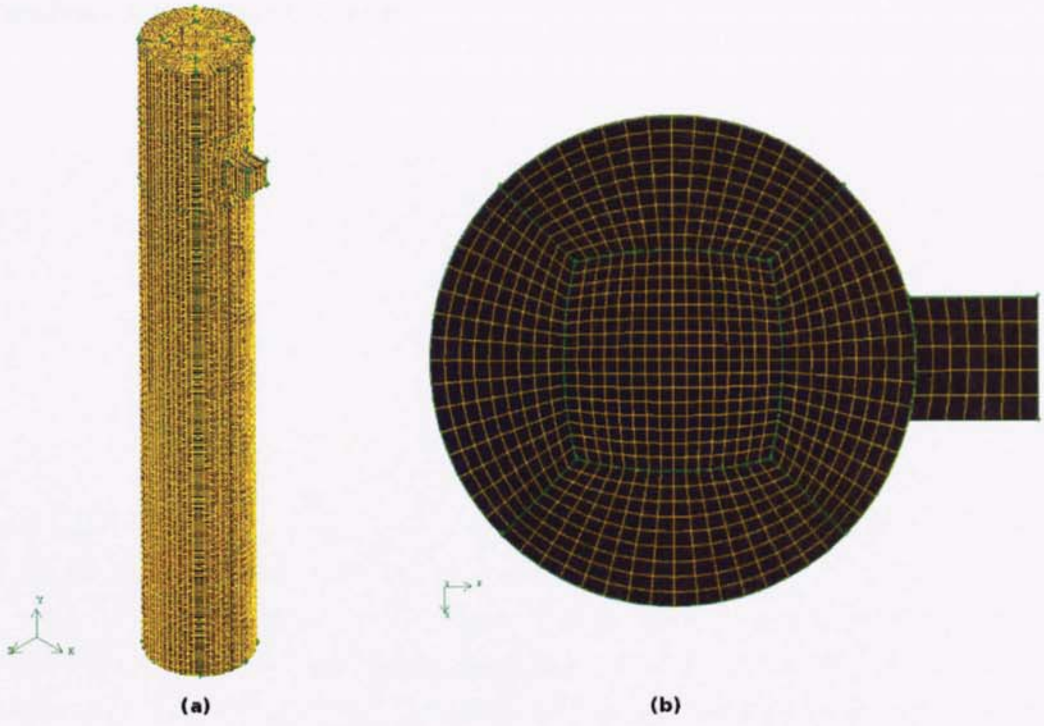

Figure A.1: (a) Isometric & (b) bottom view of the meshed geometry of the reactor before the final choice was made. The grid dependency of the simulation results was not of significant importance, however the computational times differed significantly. The final mesh dimensions were selected after critical comparisons were made.

The geometry has been splitted in three main areas for meshing convenience as well as to achieve as structural grid as possible. The average side length of the computational cells is about $1mm$ resulting to a total number of 216,635 cells for the 3-Dimensional case with minimum cell volume of $9.25 \times 10^{-10} m^3$, maximum cell volume of $3.3 \times 10^{-9} m^3$, and an equisize skewness of the worst element of 0.35. To retain a structured grid at the area close to the outlet of the reactor the outlet pipe was designed to be cubical whereas in reality is cylindrical. Such modification was done only for meshing purposes, since the outlet region does not affect the main operation or the hydrodynamic characteristics of the reactor.

The designed mesh was found to be suitable for this kind of simulation and convergence was easily achieved even from the first 10 time-steps. This fact reduced the simulation time significantly, whereas in cases that a more badly designed grid was used, the algorithm needed more iterations to achieve convergence, increasing significantly the simulation time.

Appendix B

Computational model development

The chapter presents the sequence of development of the computational code in C, which will be externally compiled as a User Defined Function (UDF) into FLUENT to simulate fast pyrolysis. The basic CFD principles are presented together with a discussion on the limitations of FLUENT on the discrete phase model and its interaction with the multiphase flow models. The weaknesses are identified and the proposed solutions are thoroughly explained.

B.1 CFD principles

Computational fluid dynamics (CFD) is the analysis of systems that involve fluid flow, heat transfer, chemical reaction etc. by means of computer based simulations. A CFD code is based on the development of numerical algorithms that can approximate the solutions of the partial differential conservation equations using numerical analysis. CFD is gradually accepted as a reliable tool for the development and optimisation of industrial equipment with the vast increase of the computational power in recent years to be its most important ally.

Behind every CFD code lies the numerical algorithm and especially the method of discretisation of the differential or integro-differential governing equations. The most widely used numerical schemes used by engineers and scientists are the Finite Difference Method (FDM), the Finite Volume Method (FVM) and the Finite Element Method (FEM). A brief description of the numerical schemes according to Ferziger and Peric [204] is the following.

- *Finite Difference Method (FDM)*: The starting point for the FDM is the conservation equation in differential form. The solution domain is covered by a grid. At each grid point, the differential equation is approximated by replacing the partial derivatives by approximations in terms of the nodal values of the functions. The result is one algebraic equation per grid node, in which the variable value at that and a certain number of neighbour nodes appear as unknowns.

- *Finite Volume Method (FVM)*: The FVM uses the integral form of the conservation equations as its starting point. The solution domain is subdivided into a finite number of contiguous control volumes (CVs), and the conservation equations are applied to each CV. At the centroid of each CV lies a computational node at which the variable values are to be calculated. Interpolation is used to express variable values at the CV surface in terms of the nodal (CV-centre) values. Surface and volume integrals are approximated using suitable quadrature formulae. As a result, one obtains an algebraic equation for each CV, in which a number of neighbour nodal values appear. The FVM is also used by the commercial code FLUENT, which is the basic computational platform of the current study.

- *Finite Element Method (FEM)*: In the FEM the domain is broken into a set of discrete volumes or finite elements that are generally unstructured; in 2D, they are usually triangles or quadrilaterals, while in 3D tetrahedra or hexahedra are most often used. The distinguishing feature of FEM is that the equations are multiplied by a weight function before they are integrated over the entire domain. In the simplest FEMs, the solution is approximated by a linear shape function within each element in a way that guarantees continuity of the solution across element boundaries. Such a function can be constructed from its values at the corners of the elements. The weight function is usually of the same form. This approximation is then substituted into the weighted integral of the conservation law and the equations to be solved are derived by requiring the derivative of the integral with respect to each nodal value to be zero (minimum residual). The result is a set of non-linear algebraic equations.

An analytical description and derivation of the numerical schemes used in CFD can be found in many textbooks [153, 204–207]. In the current study the FDM and FVM are the methods that were used in the development of the code for fast pyrolysis. Examples are going to be given on how the heat diffusion equation was discretised and how it was incorporated in the user defined function for fast pyrolysis.

B.1.1 The finite volume method

For text shortening due to mathematical overloading of the thesis, it will be shown how the FVM was applied to the heat diffusion equation (eq. 3.95), which was one of the most important equations that was incorporated in the user defined function for the fast pyrolysis model. The reader is referred to the bibliography on CFD for analytical derivations of difference equations and various boundary conditions for fluid flow problems.

Numerical discretisation of internal points

In its simplest form eq. 3.95 without taking into account chemical reactions can be written as

$$\rho C_p \frac{\partial T}{\partial t} = \frac{k}{r^2}\frac{\partial}{\partial r}\left(r^2 \frac{\partial T}{\partial r}\right). \tag{B.1}$$

After manipulation of the derivatives, eq. B.1 is written as

$$\rho C_p \frac{\partial T}{\partial t} = k\left(\frac{2}{r}\frac{\partial T}{\partial r} + \frac{\partial^2 T}{\partial r^2}\right). \tag{B.2}$$

With respect to fig. B.1 the particle is splitted in control volumes (CVs) and different nodal points are identified. Taking nodal point i and the nodal value T to represent the average value for the CV for $\frac{\partial T}{\partial t}$, the discretised form of eq. B.2 can be derived by integrating over the whole control volume using a forward difference in time

$$\rho C_p \int_{i-1/2}^{i+1/2}\int_{t}^{t+\delta t} \frac{\partial T}{\partial t} A dr dt = \int_{i-1/2}^{i+1/2}\int_{t}^{t+\delta t} k\left(\frac{2}{r}\frac{\partial T}{\partial r} + \frac{\partial^2 T}{\partial r^2}\right) A dr dt, \tag{B.3}$$

where A is the area of the CV perpendicular to the radius of the particle, the subscripts $i+1/2$ and $i-1/2$ are the values of T at the faces of the control volumes, and n represents the time level for evaluation of the heat flow into the control volume. Then, the left hand side of eq. B.3 results to

$$\rho C_p \int_{i-1/2}^{i+1/2}\int_{t}^{t+\delta t} \frac{\partial T}{\partial t} A dr dt = \rho C_p (T_i^{n+1} - T_i^{n}) A \delta r. \tag{B.4}$$

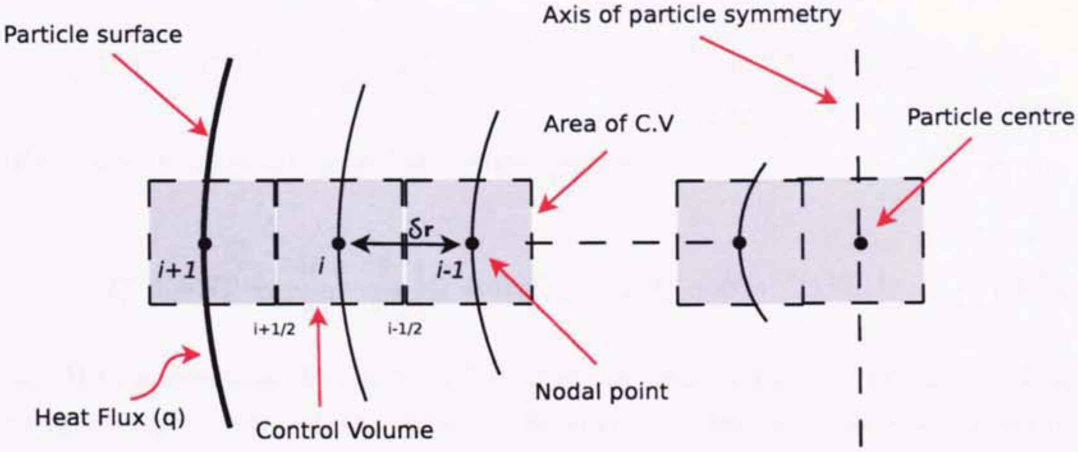

Figure B.1: Particle discretisation with control volumes

At the right hand side of eq. B.3 we apply a central difference scheme (CDS) for the derivatives at the faces of the CVs and so the FV difference equation for all the internal points of the particle is derived. In this case, the first order derivatives are calculated in the following manner

$$\frac{\partial T}{\partial r} = \frac{T^n_{i+1/2} - T^n_{i-1/2}}{\delta r}. \tag{B.5}$$

In the same way the second order derivatives are calculated as

$$\frac{\partial^2 T}{\partial r^2} = \frac{\left.\frac{\partial T}{\partial r}\right|^n_{i+1/2} - \left.\frac{\partial T}{\partial r}\right|^n_{i-1/2}}{\delta r}, \tag{B.6}$$

where the linear interpolation at the faces of the volumes using a CDS is as follows

$$T^n_{i+1/2} = \frac{T^n_{i+1} + T^n_i}{2} \tag{B.7}$$

and

$$T^n_{i-1/2} = \frac{T^n_{i-1} + T^n_i}{2}. \tag{B.8}$$

The discretised form of eq. B.2 is therefore given by

$$\rho C_p(T_i^{n+1} - T_i^n)A\delta r = \int_t^{t+\delta t} k\Big(\frac{2(T_{i+1/2}^n - T_{i-1/2}^n)}{r\delta r} + \frac{T_{i+1}^n - 2T_i + 2T_{i-1}^n}{\delta r^2}\Big)A\delta r dt, \tag{B.9}$$

where after manipulations and simplifications results to

$$T_i^{n+1} = T_i^n + \frac{\delta t}{r\delta r^2}\cdot\frac{k}{\rho C_p}\Big[(r+\delta r)T_{i+1}^n - 2rT_i^n + (r-\delta r)T_{i-1}^n\Big]. \tag{B.10}$$

Eq. B.10 respresents the discretised form of the heat diffusion equation (eq. B.2) using an explicit scheme (the values of the next time-step are based only on values of the previous time-step) and it is valid for all the internal nodal points of the particle.

Numerical discretisation at boundaries

However, the heat fluxes at the boundary points (surface, centre) have to be calculated as well. Applying the FV approach to eqs. 3.96 and 3.97 which represent the boundary conditions, the values of T at the surface and at the centre of the particle can be computed.

The numerical expression for the surface temperature according to fig. B.1 is given by

$$T_{i+1}^{n+1} = T_{i+1}^n + \Big(\frac{2k}{\rho C_p}\cdot\frac{T_{i+1}^n - T_i^n}{\delta r^2} + \frac{2h}{\rho C_p}\frac{T_\infty - T_{i+1}^n}{\delta r}\Big)\delta t, \tag{B.11}$$

where T_{i+1} is the nodal point at the boundary surface. The discretisation of the heat equation at the centre of the particle though is peculiar. By examining eq. B.2 one can immediately see that at the centre of the particle the term $\frac{2}{r}$ will tend to infinity simply because the limit of r at the centre is zero, hence $\lim_{r\to 0}\frac{2}{r}\frac{\partial T}{\partial r} = [\frac{0}{0}]$. Applying *L' Hospital's rule* to the centre condition one can easily overcome this problem. The rule de L' Hospital states that

If

$$\lim_{x\to 0}\Big[\frac{f(x)}{g(x)}\Big] = \text{Indeterminate form}\Big[\frac{0}{0}\Big], \Big[\frac{\infty}{\infty}\Big], \text{etc},$$

and

$$\lim_{x\to 0}\Big[\frac{f'(x)}{g'(x)}\Big] = \xi,$$

then

$$\lim_{x \to 0}\left[\frac{f(x)}{g(x)}\right] = \xi.$$

Applying the same rule to the centre point condition of eq. B.2 we get

$$\lim_{r \to 0}\left[\frac{\partial T}{r \partial r}\right] = \lim_{r \to 0}\left[\frac{\frac{\partial}{\partial r}\partial T}{\frac{\partial}{\partial r} r \partial r}\right] = \lim_{r \to 0}\left[\frac{\frac{\partial^2 T}{\partial r}}{\frac{\partial r^2}{\partial r} + \cancelto{0}{r\frac{\partial^2 r}{\partial r}}}\right] = \frac{\partial^2 T}{\partial r^2}.$$

Therefore, eq. B.2 can be written at the centre point $r = 0$ as

$$\rho C_p \frac{\partial T}{\partial t} = 3k\left(\frac{\partial^2 T}{\partial r^2}\right). \tag{B.12}$$

The discretised form of equation B.12 taking into account the symmetry of the particle at the centre results to

$$T_i^{n+1} = T_i^n + \left(\frac{6k}{\rho C_p}\right)\left(\frac{\delta t}{\delta r^2}\right)(T_{i+1}^n - T_i^n). \tag{B.13}$$

where in this case the nodal point T_i represents the nodal point at the centre of the particle.

Density calculation

In the case of fast pyrolysis where chemical reactions occur, the effective thermal conductivity and effective specific heat capacity are calculated from eq. 3.98 and 3.99 respectively. The rate of change the density of the particle that appears in eq. 3.95 is calculated as the particle density difference in two succeeding time-steps due to devolatilisation of the biomass particle in time.

The instantaneous density of the particle is calculated as the sum of all the discrete densities that have been produced from the discretisation of the particle as it is illustrated in fig. B.2. The radius of the particle is discretised to N number of grid points numbered from $k = 0$ to $k = N$, where 0 is the centre of the particle, generating N discrete volumes. The density distribution along the radius of the particle is calculated according to the discrete masses of the solid phases (wood and char) that correspond to the specific discrete volume. The discrete masses of the solid phases are calculated using a linear approximation between two neighbouring points that form a discrete volume, according to the mass fraction in time of the specific phase.

The discrete volumes are given by

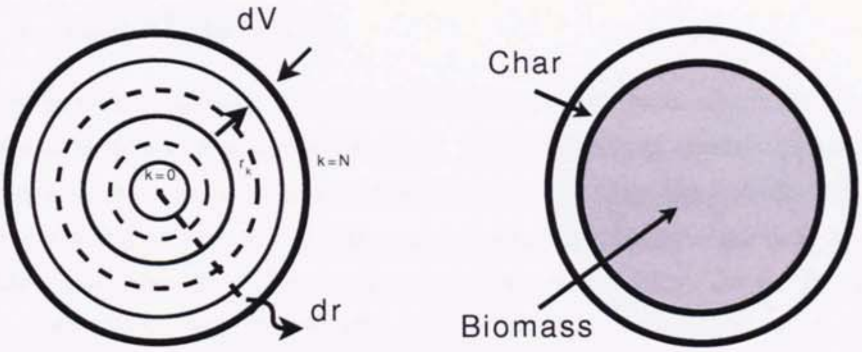

Figure B.2: Left: Particle discretisation and discrete volume generation, Right: Char formation during pyrolysis

$$dV_k = \frac{4}{3}\pi(r_k^3 - r_{k-1}^3) \qquad for \quad k = 1 \dots N \tag{B.14}$$

where

$$r_{k-1} = r_k - dr. \tag{B.15}$$

The discrete mass dm_k is calculated by

$$dm_k = \frac{(\psi_{kW} + \psi_{k-1W}) + (\psi_{kC} + \psi_{k-1C})}{2}\frac{m_d}{N} \qquad for \quad k = 1 \dots N, \tag{B.16}$$

where the terms ψ_{kW} and ψ_{kC} represent the local mass fractions of wood and char respectively. Therefore, the discrete particle densities $d\rho_{d_k}$ along its radius are given by

$$d\rho_{d_k} = \frac{dm_k}{dV_k} \tag{B.17}$$

and the total average particle density is

$$\rho_{d_{av}} = \frac{1}{N}\sum_{k=1}^{N} d\rho_{d_k}. \tag{B.18}$$

The rate of change of density is multiplied by the heat of reaction ΔH to account for the heat addition due to phase transition phenomena.

B.2 Code structure

Before anything was actually written in C language, the basic needs for the simulation of fast pyrolysis had to be determined. The progammer needs to know what he wants to model and how he is going to achieve it. The basic limitations of FLUENT in the cooperation of the multiphase models and the discrete particle model had to identified and the basic flow of the code had to be determined. In summary, the basic simulation needs of the fast pyrolysis process are focused on the following sectors:

- Fluidised bed hydrodynamics.
- Momentum transported from the bubbling bed to the discrete biomass particles injected into it.
- Identification of regime of interest (dense packed, dilute, freeboard) for correct drag and virtual mass force calculations.
- Heat transfer from the bubbling bed to the surface of the particle.
- Heat conduction along the radius of the reacting particles.
- Chemical kinetics associated with the freely moving reacting biomass particles.
- Evolution of vapours inside the reactor and determination of residence time.
- Determination of residence time of biomass particles while they are converted to char.

FLUENT has extreme capabilities in particle tracking with simultaneous particle heating using different heating laws as well as in modelling the hydrodynamics of fluidised beds with interphase heat and mass transfer. However, there are some important limitations related to the particle tracking when combined with a multiphase model (in this case the Eulerian model). The particle tracking interacts only with the primary phase, which in this case is the nitrogen. Thus, the heat and momentum transported from the secondary phase (sand) to the particles is totally lost, something which cannot be ignored since sand hydrodynamics is the most important factor for the determination of the particle motion and temperature in the reactor, which in turn affects its chemical kinetics. Such a simplification for a fast pyrolysis simulation would unacceptable.

Another significant limitation concerns the discrete phase and is that the discrete phase is sufficiently dilute and that particle-particle interactions and the effects of the particle volume fraction on the gas phase are negligible. However, due to the small size of biomass particles used as well as the low number of particles injected and studied in each simulation make this assumption valid.

FLUENT provides to the user the capability of developing user defined functions (UDFs) to overcome such problems together with the access to flow variables using the so-called "DEFINE" macros. The access to simulation variables is not limited only to fluid variables but also to the discrete particle variables. A detailed user defined function for fast pyrolysis should incorporate to FLUENT's main code not only the chemical kinetics of biomass but also the way to define the correct momentum and heat transfer according to present state of the particle. The pyrolysis products should be radially predicted and the mass sources for the evolution of vapours be calculated. In other words, the whole momentum and heat transfer model have to be revised and re-written in the form of UDF to take into account the complex interactive phenomena that occur in a fluidised bed reactor.

B.2.1 Scalar update

The way that was found to be more suitable to treat these problems, was to use the macro given by FLUENT and it is called DEFINE_DPM_SCALAR_UPDATE to update scalar quantities every time a particle position is updated. With this function particle-related variables are updated or integrated over the life of the particle. The

Argument type	**Description**
symbol name	UDF name
cell_t c	Index that identifies the cell that the particle is currently in
Thread *t	Pointer to the thread the particle is currently in
int initialise	Variable that has a value of 1 when the function is called at the start of the particle integration, and 0 thereafter
Tracked_Particle *p	Pointer to the Tracked_Particle data structure which contains data related to the particle being tracked

Table B.1: Arguments of the DEFINE_DPM_SCALAR_UPDATE function

DEFINE_DPM_SCALAR_UPDATE function contains five arguments given in table B.1.

The significant advantage of this function is that gives the opportunity to the user to define abstract function by including the necessary number of scalars and then correlate or equate the flow variables to the calculated values by the code. It also passes the continuous phase variable information at the cell and thread that the particle is currently in directly to the code, without having to define new cell and thread pointers on the main body of the function. One major disadvantage is that the scalar update function needs a significant amount of time to execute since it is called at every particle time-step and the demand of memory allocation can sometimes be very high.

B.2.2 Separation of computational domains

The most important part of a multiphase code is the correct identification of phase domains and threads, and the generanation of pointers that will be able to access the correct information from each computational cell as it is shown on fig. B.3. In order to integrate the equations of motion for the discrete particle, the code must be able to identify the regime that the particle is currently in as well as to extract the correct information of the flow variables of each of the continuous phases and use them in the equations of motion that were analytically described in chapter 3.

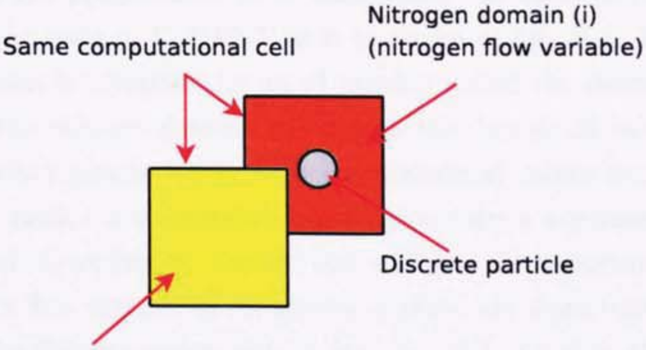

Figure B.3: Interpenetrating nitrogen and sand phases with discrete particle. All phases share the same computational cell. The code must be able to access the different flow variables of each phase.

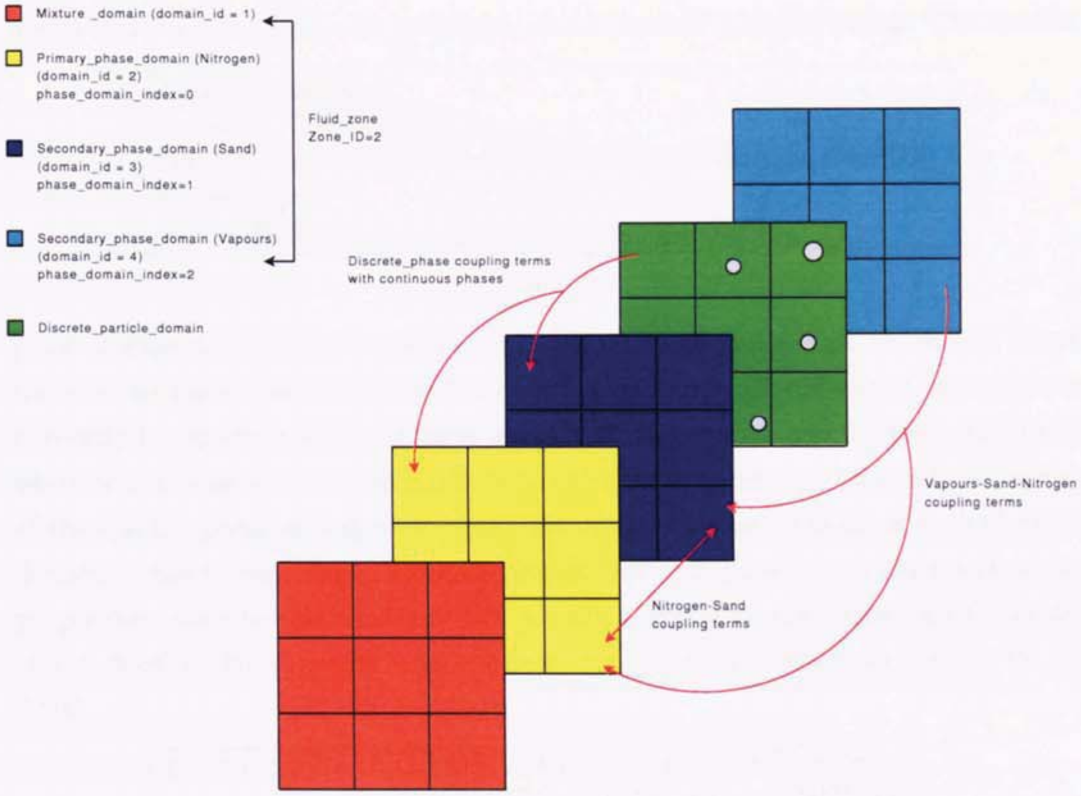

Figure B.4: Domain and thread structure hierarchy in user defined function

In doing this the programmer must understand the basic hierarchy of domains and threads of the code of FLUENT as it is shown of fig. B.4. Each of the computational domains is identified by an id number called the **domain_id**. The top level domain is the mixture domain and carries the domain_id value of 1. The primary and secondary phases follow with the domain_id values increasing by 1 in a logical manner. Each computational domain also carries a **phase_domain_index** which corresponds to an integer number that will give the opportunity to the user to access the correct flow variable of the specific continuous phase that shares a computational cell. The discrete phase domain was placed just before the computational domain of vapours because in the user defined function developed for fast pyrolysis the discrete biomass particles are the ones that interact with sand and nitrogen and the vapours are the outcome of this specific interaction. The discrete phase domain does not carry **domain_id** and **phase_domain_index** since the macros and variables used by FLUENT are completely different than the ones for the continuous phases. The piece of code in C language that will separate the computational domains and threads and create pointers to these threads is the following. The specific

```
Domain * domain;
domain = Get_Domain(1);
Thread *mixture_thread = Lookup_Thread(domain,zone_ID);
Thread **pt;
pt = THREAD_SUB_THREADS(mixture_thread);
```

piece of code declared above, will create the necessary pointer **pt** which will direct the code to the correct flow variable on the computational cell that the particle is currently in. In other words, it gives the opportunity to the user to define functions which will contain the instantaneous values of velocity, pressure, volume fraction etc. of the specific phase at a specific time. The computational domain of each phase is defined by the integer **phase_domain_index**, which is placed as an argument at the **pt** pointer. An example to clarify this situation would be the following calculation of the density times specific heat capacity $(\rho C_p)_m$ of a mixture as defined by eq. 3.103.

```
rho_CP_mix =   (C_VOF(c,pt[i])*C_R(c,pt[i])*CP_nitro) +
               (1 - C_VOF(c,pt[i]))*C_R(c,pt[j])*CP_sand;
```

In this case the variables **CP_nitro**, **CP_sand** are real values defined at the beginning of the code, representing the specific heat capacity of nitrogen and sand and can either be constants or derived by an expression. The values **C_VOF(c,pt[i])**, **C_R(c,pt[i])** and **C_R(c,pt[j])** represent the local flow variables of nitrogen volume fraction, nitrogen density and density of sand at the cell that the particle is currently in. The argument **c** inside the brackets represents the cell that the particle is inside, where the arguments **pt[i]** and **pt[j]** represent the thread pointers to the phase of nitrogen and sand respectively. The values **i** and **j** represent the phase_domain_index that corresponds to a specific phase. In this function the values of **i** and **j** have been declared at the beginning of the code as $i = 0$ and $j = 1$. In the same way if a variable of vapours during their evolution is needed the corresponding phase_domain_index **v** has been declared as $v = 2$.

One can notice that in the piece of code explained above, the value of (1 - C_VOF(c,pt[i])) is actually simply equal to C_VOF(c,pt[j]) if there is no presence of vapour in the computational cell, since according to mass balance the sum of volume fractions of all phases sharing a control volume must be equal to unity. Table B.2

shows the most important continuous phase flow variables that have been used in the implementation of the code.

Flow variable	Description
C_VOF(c,pt[i])	Volume fraction of phase i
C_VOLUME(c,pt[i])	Volume of computational cell that the particle is currently in
C_U(c,pt[i])	x-velocity component of phase i
C_V(c,pt[i])	y-velocity component of phase i
C_W(c,pt[i])	z-velocity component of phase i
C_U_M1(c,pt[i])	x-velocity component of phase i at previous time-step
C_V_M1(c,pt[i])	y-velocity component of phase i at previous time-step
C_W_M1(c,pt[i])	z-velocity component of phase i at previous time-step
C_R(c,pt[i])	Density of phase i
C_T(c,pt[i])	Temperature of phase i
C_MU_L(c,pt[i])	Laminar viscosity of phase i
CURRENT_TIME	Current flow time
CURRENT_TIMESTEP	Current flow time-step

Table B.2: Continuous phase flow variables, provided by the solver of FLUENT, used in the UDF of fast pyrolysis

B.2.3 Discrete phase variables

In the same way that the flow variables were defined for the continuous phases, FLUENT provides variables associated with the discrete particles. The combination of the two types of variables were used to implement the UDF for fast pyrolysis in FLUENT. Table B.3 shows the most significant discrete phase variables used in the implementation of the UDF. Since the properties of the biomass particles are properties of the discrete phase, then all the necessary calculation of heat transfer, chemical kinetics, particle velocities after the integration of the equations of motion are associated with the variables shown on table B.3.

The major disadvantage in writing a UDF for fast pyrolysis, is the progression in time of the heat transfer conditions as well as the reaction mechanism. That means that the code has to store the values of the previous time-step in order to progress in time. This fact makes the memory requirements even greater due to

Flow variable	Description
P_MASS(p)	Particle mass
P_RHO(p)	Particle density
P_DIAM(p)	Particle diameter
P_VEL(p)[0]	x-velocity component of particle
P_VEL(p)[1]	y-velocity component of particle
P_VEL(p)[2]	z-velocity component of particle
P_T(p)	Particle temperature
P_TIME(p)	Particle current time
P_DT(p)	Particle current time-step
P_USER_REAL(p,i)	Scalar associated with the particle

Table B.3: Discrete phase variables, provided by the solver of FLUENT, used in the UDF of fast pyrolysis

the fact that the UDF is called in every time-step and the values calculated by the variables defined by the user are re-initialised. Therefore, all the values that need to progress in time need to be specified as user defined scalars. In the case of a discrete phase UDF the scalars are defined as **P_USER_REAL(p,i)** values, where **p** is the pointer to the particle and **i** the identity number of the scalar. Thus, every loop counter or radial nodal points for heat transfer and reaction kinetics etc. must be defined as **P_USER_REAL(p,i)** values in order to progress in time using values from the previous time-steps. Sometimes this procedure may slow down the calculations significantly.

An example that makes use of the **P_USER_REAL(p,i)** scalars to progress in time is the piece of the code written to calculate the heat distribution for all the internal points of the particles.

```
for (grid_c = N+1; grid_c <= (2*N)-2 ; grid_c++)
{
R = (P_DIAM(p)/2) - (grid_c - N)*dx;

COURANT = CURRENT_TIMESTEP/(R*pow(dx,2));

P_USER_REAL(p,grid_c) = P_USER_REAL(p,grid_c) + D_M[(grid_c - N)]
*COURANT*(P_USER_REAL(p,grid_c-1)*(R+dx) - 2*R*P_USER_REAL(p,grid_c)
+ P_USER_REAL(p,grid_c+1)*(R-dx)) + Q;
}
```

Taking into account the chemical kinetics of biomass, which are expressed as mass balances that progress in time the amount of discrete phase scalars immediately becomes very large. The following piece of code shows exactly this situation.

```
for (matrix_c = 0; matrix_c <= N-1; matrix_c++)
{
/*Arrhenius constants matrices*/
K1_M[matrix_c] = A1*exp(-E1/(R_G*T[matrix_c]));
K2_M[matrix_c] = A2*exp(-E2/(R_G*T[matrix_c]));
K3_M[matrix_c] = A3*exp(-E3/(R_G*T[matrix_c]));
K4_M[matrix_c] = A4*exp(-E4/(R_G*T[matrix_c]));
K5_M[matrix_c] = A5*exp(-E5/(R_G*T[matrix_c]));
}
/*Mass fraction of the product yields*/
/*Wood mass fraction: P_USER_REAL values from 20 - 29*/
for (grid_c = 2*N; grid_c <= (3*N)-1 ; grid_c++)
{
P_USER_REAL(p,grid_c) = P_USER_REAL(p,grid_c) - (K1_M[grid_c - 2*N] + K2_M[grid_c - 2*N] + K3_M[grid_c
- 2*N])*P_USER_REAL(p,grid_c)*CURRENT_TIMESTEP; W[(grid_c - 2*N)] = P_USER_REAL(p,grid_c);
}
/*Char mass fraction: P_USER_REAL values from 30 - 39*/
for (grid_c = 3*N; grid_c <= (4*N)-1 ; grid_c++)
{
P_USER_REAL(p,grid_c) = P_USER_REAL(p,grid_c) + K3_M[grid_c - 3*N]*W[(grid_c - 3*N)]
*CURRENT_TIMESTEP; C[(grid_c - 3*N)] = P_USER_REAL(p,grid_c);
}
/*Tar mass fraction: P_USER_REAL values from 40 - 49*/
for (grid_c = 4*N; grid_c <= (5*N)-1 ; grid_c++)
{
dTAR[(grid_c - 4*N)] = (K2_M[grid_c - 4*N]*W[(grid_c - 4*N)])*CURRENT_TIMESTEP;
dTAR_sec[(grid_c - 4*N)] = (K4_M[(grid_c - 4*N)] + K5_M[(grid_c - 4*N)])*dTAR[(grid_c -
4*N)]*CURRENT_TIMESTEP;
P_USER_REAL(p,grid_c) = P_USER_REAL(p,grid_c) + dTAR[(grid_c - 4*N)] - dTAR_sec[(grid_c - 4*N)];
TAR[(grid_c - 4*N)] = P_USER_REAL(p,grid_c);
}
/*Primary Gas mass fraction: P_USER_REAL values from 50 - 59*/
for (grid_c = 5*N; grid_c <= (6*N)-1 ; grid_c++)
{
P_USER_REAL(p,grid_c) = P_USER_REAL(p,grid_c) + K1_M[(grid_c - 5*N)]*W[(grid_c -
5*N)]*CURRENT_TIMESTEP;
G[(grid_c - 5*N)] = P_USER_REAL(p,grid_c);
}
/*Secondary Char mass fraction: P_USER_REAL values from 60 - 69*/
for (grid_c = 6*N; grid_c <= (7*N)-1 ; grid_c++)
{
P_USER_REAL(p,grid_c) = P_USER_REAL(p,grid_c) + K5_M[grid_c - 6*N]*dTAR[(grid_c -
6*N)]*CURRENT_TIMESTEP;
C2[(grid_c - 6*N)] = P_USER_REAL(p,grid_c);
}
/*Secondary Gas mass fraction: P_USER_REAL values from 70 - 79*/
for (grid_c = 7*N; grid_c <= (8*N)-1 ; grid_c++)
{
P_USER_REAL(p,grid_c) = P_USER_REAL(p,grid_c) + K4_M[grid_c - 7*N]*dTAR[(grid_c -
7*N)]*CURRENT_TIMESTEP;
G2[(grid_c - 7*N)] = P_USER_REAL(p,grid_c);
}
/*Total gas and char formation*/
for (matrix_c = 0; matrix_c <=N-1; matrix_c++)
{
TG[matrix_c] = G[matrix_c] + G2[matrix_c];
TC[matrix_c] = C[matrix_c] + C2[matrix_c];
}
```

The user defined variable **grid_c** identifies the nodal points from the surface to the centre of the particle. In this piece of code one can easily see the great need for storage allocations since every discrete scalar must be unique for the variable that it expresses. In this case only 10 radially distributed nodal points are used so in order to calculate the radial distribution of temperature and product yields, which means that up to 80 different **P_USER_REAL(p,i)** storage values have to be defined. The counter **matrix_c** is the counter of the matrices used to temporarily store the values which are written on the output file for post processing. The matrices of the kinetic constants (**K1_M, K2_M, K3_M, K4_M, K5_M**) are being replaced by new values in each time-step that the UDF is called depending on the radial distribution of temperature that has been calculated in the previous one.

B.2.4 Definition of sources

The final step for the fast pyrolysis UDF would be the determination of the mass, momentum and energy sources for the produced vapours and gases. In order to avoid the programming overloading of the thesis only the determination of the mass source of vapours is shown as an example, since the rest sources are defined in a similar fashion. The following piece of code defines the mass source of the vapour released in the computational domain in each time-step. The definition of the mass source of vapour is made using the macro **DEFINE_SOURCE** provided by FLUENT. The definition of a variable **tar_mass_source** is necessary to return the value of vapour mass (kilogram per meter cubed per second, kg/m^3s) that has been calculated by the main body of the code and has been stored to a memory location (**C_UDMI(c,t,0)**). This value is then released in the computational domain as a mass source. The same procedure has to be done to define the momentum sources for the x,y,z components separately as well as the energy source for the amount of mass released.

```
DEFINE_SOURCE(tar_mass_source,c,t,dS,eqn)
{
real tar_mass_source;
tar_mass_source = C_UDMI(c,t,0);
return tar_mass_source;
C_UDMI(c,t,0) = 0;
}
```

Certainly, the amount of code that has been shown is not representative of the complete function that has been developed. For the definition of momentum and energy sources the particle velocities that are calculated by the integration of the equations of motion have to be defined as well as the average particle mass, density and temperature due to chemical reactions. The final size of the complete UDF had reached almost 650 lines without the additional extensions for biomass shrinkage and effect of particle size on the heat transfer coefficient. Specific parts of the code have been shown as representations of the procedure that had been followed.

B.2.5 Simulation sequence

Figure B.5 illustrates the flow-chart of the extension code for FLUENT and it is called at the end of each time-step. When the simulation reaches the injection time, the UDF initialises all the fields and matrices that are going to be used for the calculations that follow. When the injection time is exceeded (indicated by *"No"* in the flow-chart) then the discrete phase variables used by FLUENT in its macros are being replaced by the ones calculated by the code. The new values are calculated by defining scalar updates, since the cell and the thread pointers in the specific macro (**DEFINE_SCALAR_UPDATE**) correspond to the cell that the particle is currently in. Therefore, the local property values of the sand and nitrogen can be easily accessed by separating the solution domains for each phase in the UDF, as discussed in section B.2.2.

The UDF is splitted in multiple parts in order to achieve more efficient code structure as well as convenient future modifications . The first part calculates the properties of the particle (density, effective thermal conductivity, effective specific heat capacity etc.), since those are values that continuously change as the reaction progresses in time. Then, identifies the regime that the particle finds itself in (the particle can be either in the freeboard or inside a bubble or the sand bed) comparing the volume fractions of sand and nitrogen phases by using the relations described in section 3.5. The code then moves into the discretisation of the particle in a number of radially distributed nodal points defined by the user. The number of nodal points have to be carefully selected because instabilities on the numerical algorithm for the heat diffusion equation might occur, which will greatly affect the results and especially the expected product yields from the chemical reactions. The heat transfer section calculates the radially distributed heat transfer and product yield distribution during the pyrolysis of the particle, according to the two-stage semi-global mechanism described in section 2.5 and illustrated in fig. 2.8. At the

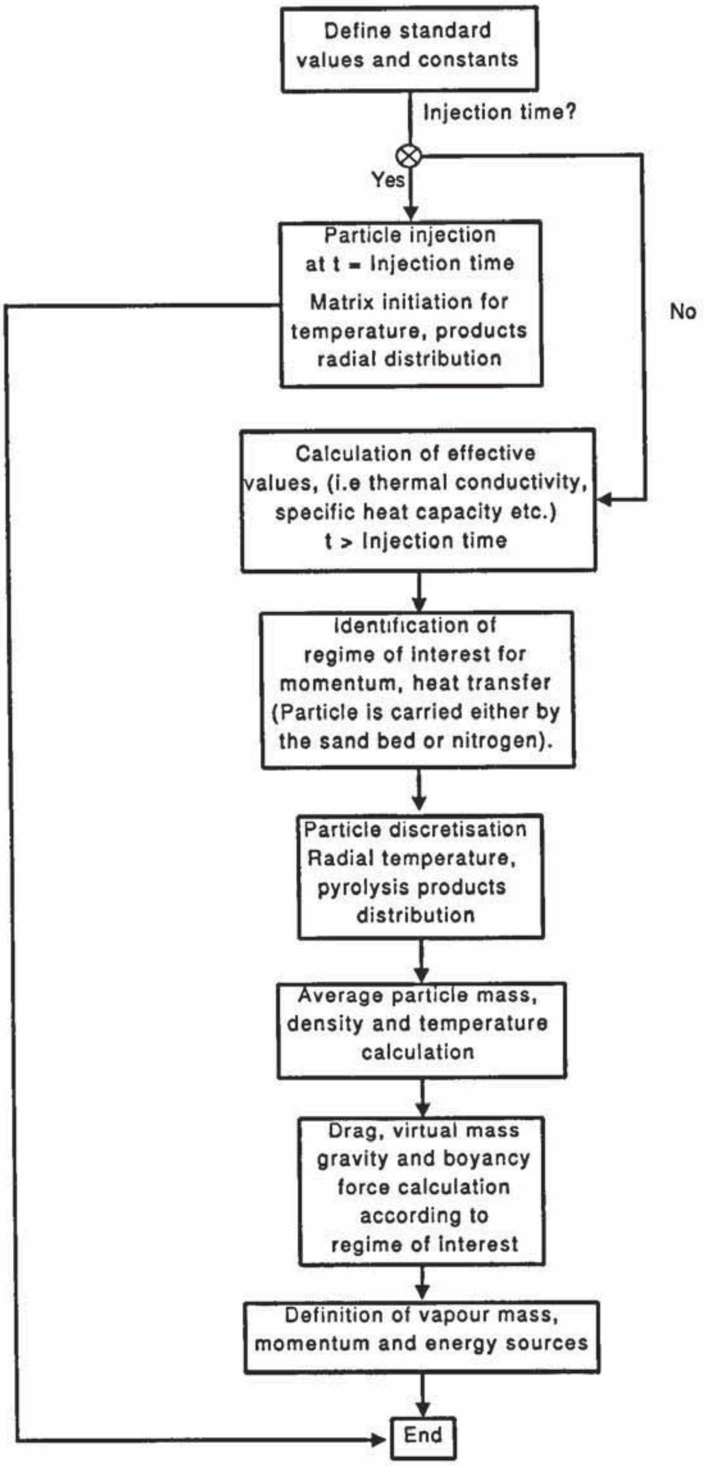

Figure B.5: Flow chart of the fast pyrolysis model end of the product yields calculations a small loop is used to average the properties of the reacted particle in its volume (mass, density, temperature), as well as to define the mass and energy sources of the produced gases and vapours. Finally, the forces (drag, gravity, buoyancy, virtual mass) exerted on the particle are calculated and its velocity is defined for the next time-step. After the calculation of the particle velocity the momentum sources of the produced gases and vapours are calculated as well. At the end of the code the definition of sources follows using the macro DEFINE_SOURCE, which are then released into the computational domain.

Appendix C

Reynolds transport theorem

The following proof of the Reynolds transport theorem is presented according to Gidaspow [53], and Aris [151]. Balances are made on some quantity $F(t)$ that can be counted and changes with time. In space we define a property per unit volume $\mathscr{J}(t, \mathbf{x})$, where t is time and $\mathbf{x}$ is the position vector, such that

$$F(t) = \iiint\limits_{V(t)} \mathscr{J}(t, \mathbf{x}) dV. \tag{C.1}$$

In the Lagrangian representation let three parameters $(x^0, y^0, z^0) = \mathbf{x}^0$ identify the individual particle of the continuum. Thus (x^0, y^0, z^0) are the coordinates of the particle at some given time t^0. Then the spatial coordinates of the particle at any time are given by functions of

$$\begin{aligned} x &= x(t, x^0, y^0, z^0), \\ y &= y(t, x^0, y^0, z^0), \\ z &= z(t, x^0, y^0, z^0), \end{aligned} \tag{C.2}$$

as shown in fig. C.1

The functions x, y, z are taken to be single valued and at least twice differentiable. The transformations are assumed to be one-to-one, so that the inverse transformations exist and are twice continuously differentiable. Hence,

$$\begin{aligned} x^0 &= x^0(t, x, y, z), \\ y^0 &= y^0(t, x, y, z), \\ z^0 &= z^0(t, x, y, z), \end{aligned} \tag{C.3}$$

The functions $\mathbf{x}$ and $\mathbf{x}^0$ are inverse. The flow velocities or "particle velocities" for

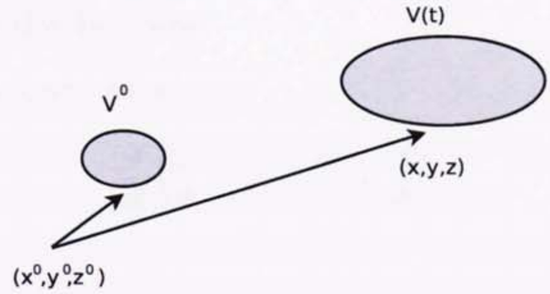

Figure C.1: Motion of a system of constant mass

the continuum are then defined as

$$\mathbf{v}(t,\mathbf{x}) = \frac{d\mathbf{x}}{dt} = \frac{\partial \mathbf{x}(t,\mathbf{x}^0)}{\partial t}. \tag{C.4}$$

Differentiation of eq. C.1 can be done by changing the region of integration from the arbitrary volume $V(t)$ in fig. C.1 to the fixed initial volume. To change the limits of integration one makes use of a formula from advanced calculus which can be found on Aris [151] and expresses a local relation between points in the configuration $V(t)$ and corresponding points in the configuration V^0. That is the Jacobian determinant J and results to

$$dV = JdV^0. \tag{C.5}$$

The differentiation of C.1 then gives

$$\frac{dF(t)}{dt} = \frac{d}{dt}\iiint\limits_{V(t)} \mathscr{J}(t,\mathbf{x})dV = \frac{d}{dt}\iiint\limits_{V^0} \mathscr{J}\Big[(t,\mathbf{x}(t,\mathbf{x}^0))\Big]JdV^0, \tag{C.6}$$

where

$$J = \begin{vmatrix} \frac{\partial x}{\partial x^0} & \frac{\partial y}{\partial x^0} & \frac{\partial z}{\partial x^0} \\ \frac{\partial x}{\partial y^0} & \frac{\partial y}{\partial y^0} & \frac{\partial z}{\partial y^0} \\ \frac{\partial x}{\partial z^0} & \frac{\partial y}{\partial z^0} & \frac{\partial z}{\partial z^0} \end{vmatrix} = \frac{\partial(x,y,z)}{\partial(x^0,y^0,z^0)}, \tag{C.7}$$

$$\frac{dF(t)}{dt} = \iiint\limits_{V^0} \Big(\frac{d\mathscr{J}}{dt}\cdot J + \mathscr{J}\cdot\frac{dJ}{dt}\Big)dV^0. \tag{C.8}$$

In eq. C.8 only the integrand was differentiated, since the limits are fixed.

Differentiation of the Jacobian

For the element of column one we have

$$\frac{d}{dt}\frac{\partial x}{\partial x^0} = \frac{\partial}{\partial x^0}\cdot\frac{dx}{dt} = \frac{\partial u}{\partial x^0}, \tag{C.9}$$

since

$$x = x(t, x^0, y^0, z^0) \text{ and } u = \frac{dx}{dt}. \tag{C.10}$$

To carry out $\frac{\partial v}{\partial x^0}$ note that

$$u = u\Big[t, x(t, x^0, y^0, z^0), y(t, x^0, y^0, z^0), z(t, x^0, y^0, z^0)\Big]. \tag{C.11}$$

Then

$$\frac{\partial u}{\partial x^0} = \frac{\partial u}{\partial x}\cdot\frac{\partial x}{\partial x^0} + \frac{\partial u}{\partial y}\cdot\frac{\partial y}{\partial x^0} + \frac{\partial u}{\partial z}\cdot\frac{\partial z}{\partial x^0}. \tag{C.12}$$

For $\frac{dJ}{dt}$ we obtain thesum of three determinants. The first is

$$\begin{aligned}
&\begin{vmatrix} \frac{\partial u}{\partial x^0} & \frac{\partial y}{\partial x^0} & \frac{\partial z}{\partial x^0} \\ \frac{\partial u}{\partial y^0} & \frac{\partial y}{\partial y^0} & \frac{\partial z}{\partial y^0} \\ \frac{\partial u}{\partial z^0} & \frac{\partial y}{\partial z^0} & \frac{\partial z}{\partial z^0} \end{vmatrix} = \begin{vmatrix} \frac{\partial u}{\partial x}\cdot\frac{\partial x}{\partial x^0} + \frac{\partial u}{\partial y}\cdot\frac{\partial y}{\partial x^0} + \frac{\partial u}{\partial z}\cdot\frac{\partial z}{\partial x^0} & \frac{\partial y}{\partial x^0} & \frac{\partial z}{\partial x^0} \\ \frac{\partial u}{\partial x}\cdot\frac{\partial x}{\partial y^0} + \frac{\partial u}{\partial y}\cdot\frac{\partial y}{\partial y^0} + \frac{\partial u}{\partial z}\cdot\frac{\partial z}{\partial y^0} & \frac{\partial y}{\partial y^0} & \frac{\partial z}{\partial y^0} \\ \frac{\partial u}{\partial x}\cdot\frac{\partial x}{\partial z^0} + \frac{\partial u}{\partial y}\cdot\frac{\partial y}{\partial z^0} + \frac{\partial u}{\partial z}\cdot\frac{\partial z}{\partial z^0} & \frac{\partial y}{\partial z^0} & \frac{\partial z}{\partial z^0} \end{vmatrix} \\
&= \frac{\partial u}{\partial x}\underbrace{\begin{vmatrix} \frac{\partial x}{\partial x^0} & \frac{\partial y}{\partial x^0} & \frac{\partial z}{\partial x^0} \\ \frac{\partial x}{\partial y^0} & \frac{\partial y}{\partial y^0} & \frac{\partial z}{\partial y^0} \\ \frac{\partial x}{\partial z^0} & \frac{\partial y}{\partial z^0} & \frac{\partial z}{\partial z^0} \end{vmatrix}}_{\text{J}} + \frac{\partial u}{\partial y}\underbrace{\begin{vmatrix} \frac{\partial y}{\partial x^0} & \frac{\partial y}{\partial x^0} & \frac{\partial z}{\partial x^0} \\ \frac{\partial y}{\partial y^0} & \frac{\partial y}{\partial y^0} & \frac{\partial z}{\partial y^0} \\ \frac{\partial y}{\partial z^0} & \frac{\partial y}{\partial z^0} & \frac{\partial z}{\partial z^0} \end{vmatrix}}_{\text{2 identical columns, hence zero}} + \frac{\partial u}{\partial z}\begin{vmatrix} \\ \\ \text{zero} \end{vmatrix}
\end{aligned} \tag{C.13}$$

Similarly, differentiating the second and the third columns we get

$$\frac{dJ}{dt} = \left(\frac{\partial u}{\partial x} + \frac{\partial v}{\partial y} + \frac{\partial w}{\partial z}\right)\cdot J, \tag{C.14}$$

$$\frac{\frac{dJ}{dt}}{J} = \nabla\cdot\mathbf{v}, \tag{C.15}$$

or the relative time rate of expansion which is independent of coordinate system. Thus, we obtain

$$\frac{dF}{dt} = \iiint\limits_{V^0}\left[\frac{d\mathscr{J}}{dt} + \mathscr{J}(\nabla\cdot\mathbf{v})\right]JdV^0 = \iiint\left(\frac{d\mathscr{J}}{dt} + \mathscr{J}\nabla\cdot\mathbf{v}\right)dV. \tag{C.16}$$

By chain rule,

$$\frac{d\mathscr{J}(t,x,y,z)}{dt} = \frac{\partial \mathscr{J}}{\partial t} + \frac{\partial \mathscr{J}}{\partial x}\cdot u + \frac{\partial \mathscr{J}}{\partial y}\cdot v + \frac{\partial \mathscr{J}}{\partial z}\cdot w = \frac{\partial \mathscr{J}}{\partial t} + \nabla \mathscr{J}\cdot \mathbf{v}, \quad \text{(C.17)}$$

where u, v, w are the x, y, z components of velocity. The derivative of eq. C.17 is sometimes called the substantial derivative and it is in general

$$\frac{d\mathscr{J}(t,\mathbf{x}(t))}{dt} = \frac{\partial \mathscr{J}}{\partial t} + \mathbf{v}\cdot\nabla\mathscr{J}. \quad \text{(C.18)}$$

Then, by using eqs. C.16 and C.18 the Reynolds transport theorem becomes

$$\frac{d}{dt}\iiint_{V(t)} \mathscr{J}(t,\mathbf{x})dV = \iiint_{V(t)} \left(\frac{\partial \mathscr{J}}{\partial t} + \nabla\cdot\mathscr{J}\mathbf{v}\right)dV. \quad \text{(C.19)}$$

List of Publications

1. Papadikis K, Gerhauser H, Bridgwater AV, Gu S. *CFD modelling of the fast pyrolysis of an in-flight cellulosic particle subjected to convective heat transfer.* Biomass and Bioenergy, 33 (2009) 97-107.
2. K. Papadikis, A.V. Bridgwater and S. Gu, *CFD modelling of the fast pyrolysis of biomass in fluidised bed reactors. Part A: Eulerian computation of momentum transport in bubbling fluidised beds*, Chemical Engineering Science, 63 (2008) 4218-4227.
3. K. Papadikis, S. Gu, A.V. Bridgwater, *CFD modelling of the fast pyrolysis of biomass in fluidised bed reactors. Part B: Heat, momentum and mass transport in bubbling fluidised beds*, Chemical Engineering Science, 64 (5), 2009, 1036-1045.
4. K. Papadikis, S. Gu, A.V. Bridgwater, *CFD modelling of the fast pyrolysis of biomass in fluidised bed reactors: Modelling the impact of biomass shrinkage*, Chemical Engineering Journal, 149 (1-3), 2009, 417-427.
5. K. Papadikis, S. Gu, A.V. Bridgwater, H. Gerhauser, *Application of CFD to model fast pyrolysis of biomass*, Fuel Processing Technology, 90 (4), 2009, 504-512.
6. K. Papadikis, A.V. Bridgwater and S. Gu, *A CFD approach on the effect of particle size on char entrainment in bubbling fluidised bed reactors.* (*Submitted*)
7. K. Papadikis, A.V. Bridgwater and S. Gu, *Computational modelling of the sphericity effects on char entrainment from bubbling fluidised beds.* (*Submitted*)

8. K. Papadikis, S. Gu, A.V. Bridgwater, *CFD modelling of the fast pyrolysis of biomass in fluidised bed reactors: Modelling the impact of biomass particle size on bed-to-surface heat transfer.* (*Submitted*)

Bibliography

[1] Kunii, D., Levenspiel, O., 1991. *Fluidization Engineering*, 2nd edition, Butterworth-Heinemann.

[2] Boterill, J. S. M., 1975. *Fluid-bed heat transfer*, Academic Press, New York.

[3] Americal Chemical Society (Webpage). *The fluid bed reactor.* (URL): http://portal.acs.org:80/portal/acs/corg/content?_nfpb=true&_page Label=PP_ARTICLEMAIN&node_id=924&content_id=WPCP_007606&use _sec=true&sec_url_var=region1&__uuid=. Accessed [05/01/2009]

[4] Czernik, S., Bridgwater, A. V., 2004. *Overview of Applications of Biomass Fast Pyrolysis Oil*, Energy & Fuels 2004, 18, 590-598.

[5] Bridgwater, A.V., 1999. *Principles and practice of biomass fast pyrolysis processes for liquids*, Journal of Analytical and Applied Pyrolysis 51, 3-22.

[6] Bridgwater, A.V., Meier, D., Radlein, D., 1999. *An overview of fast pyrolysis of biomass*, Organic Geochemistry, 30, (1999), 1479-1493.

[7] FLUENT Europe (Webpage). (URL): http://www.fluent.co.uk/.

[8] Kuipers, J.A.M., Hoomans, B.P.B. and van Swaaij, W.P.M. (1998), *Hydrodynamic models of gas fluidized beds and their role for design and operation of fluidized bed chemical reactors*, in Fluidization IX, Eds Fan, L.-S. and Knowlton, T.M., p. 15.

[9] Geldart, D., 1973. *Types of Gas Fluidization.* Powder Technology, 7 (1973) 285.

[10] Grace, J.R. (1992), *Characterization and interpretation of fluidization phenomena*, AIChE Symposium Series, no. 289, 88, 1-16.

[11] Ranade, V.V., 2002. *Computational flow modeling for chemical reactor engineering.* Academic Press.

[12] Grace, J.R. (1986), *Contacting modes and behavior classification of gas-solid and other two-phase suspensions*, Can. J. Chem. Eng., 64, 353363.

[13] Grace, J.R. (1982), *Fluidised bed hydrodynamics*, In: Handbook of Multiphase Systems, H. G. New York, McGraw-Hill.

[14] Wen, C.Y. and Yu, Y.H. (1966), *Mechanics of fluidization*, CEP Symposium Series, 62, 100-111.

[15] Richardson, J.F., 1971. *Incipient fluidization and particulate systems.* In: Davidson, J.F. and Harrison, D., Editors, 1971. Fluidization, Academic Press, London, pp. 25-64.

[16] Saxena and Vogel, 1977 S.C. Saxena and G.L. Vogel, *The measurement of incipient fluidization in a bed of coarse dolomite at temperature and pressure*, Transactions of the Institution of Chemical Engineers 55 (1977), p. 184.

[17] Babu, S. P., B. Shah and A. Talwalkar. 1978. *Fluidization correlations for coal gasification materials-minimum fluidization velocity and fluidized bed expansion.* AIChE Symposium Series, 74: 176-186.

[18] D.C. Chitester, R.M. Kornosky, L.S. Fan and J.P. Danko, *Characteristics of fluidization at high pressure*, Chem. Eng. Sci. 39 (1984), p. 253.

[19] Mori, S. and Wen, C.Y. (1975), *Estimation of bubble diameter in gaseous fluidized beds*, AIChE J., 21, 109-117.

[20] Darton, R.C., Lanauze, R.D., Davidson, J.F. and Harrison, D. (1977), *Bubble growth due to coalescence in fluidized beds*, Trans. Inst. Chem. Eng., 55, 274-280.

[21] Werther, J. (1978), *Effect of gas distributor on the hydrodynamics of gas fluidized beds*, Ger. Chem. Eng., 1, 166.

[22] Davidson, J.F. and Harrison, D. (1963), *Fluidized Particles*, Cambridge University Press.

[23] Werther, J. (1983), in "Fluidization IV", Eds Kunii, D. and Toei, R., Engineering Foundation, New York, p. 93.

[24] Cundall, P.A., Strack, O.D.L., 1979. *A discrete numerical model for granular assemblies.* Geotechnique 29 (1), 47-65.

[25] Tsuji, Y., Kawaguchi, T., Tanaka, T., 1993. *Discrete particle simulation of two-dimensional fluidized bed.* Powder Technology 77 (1), 79-87.

[26] Hoomans, B.P.B., Kuipers, J.A.M., Briels, W.J., Van Swaaij, W.P.M., 1996. *Discrete particle simulation of bubble and slug formation in a two-dimensional gas-fluidised bed: a hard-sphere approach.* Chemical Engineering Science 51 (1), 99-118.

[27] Deen, N.G., Van Sint Annaland, M., Van der Hoef, M.A., Kuipers, J.A.M., 2007. *Review of discrete particle modeling of fluidized beds.* Chemical Engineering Science 62 (2007), 28-44.

[28] Tsuji, T., Chiba, T., Shibata, T., Uemaki, O., Itoh, H., 1999. *Flow regime map for two dimensional spouted bed and comparison with simulation by discrete element method.* Kagaku Kogaku Ronbunshu 25,1037-1039.

[29] Tanaka, T., Kawaguchi, T., Tsuji, Y., 1993. *Discrete particle simulation of flow patterns in 2-dimensional gas-fluidized beds.* International Journal of Modern Physics B 7, 1889-1898.

[30] Xu, B.H., Yu, A.B., 1997. *Numerical simulation of the gas-solid flow in a fluidized bed by combining discrete particle method with computational fluid dynamics.* Chemical Engineering Science 52, 2785-2809.

[31] Xu, B.H., Yu, A.B., 2002. *A new stability criterion for bed expansion of gas fluidization.* In: 4th World Congress on Particle Technology, Sydney, Australia, paper no.189.

[32] Kawaguchi, T., Tanaka, T., Tsuji, Y., 1998. *Numerical simulation of two-dimensional fluidized beds using the discrete element method (comparison between the two- and three-dimensional models).* Powder Technology 96 (2), 129-138.

[33] Lu, W.M., Ju, S.P., Tung, K.L., Lu,Y.C., 1999. *Stability analysis of perforated plate type single stage suspension fluidized bed without downcomer.* Korean Journal of Chemical Engineering 16, 810-817.

[34] Lu, H., Wang, S., Zhao, Y., Yang, L., Gidaspow, D., Ding, J., 2005. *Prediction of particle motion in a two-dimensional bubbling fluidized bed using discrete hard-sphere model.* Chemical Engineering Science 60 (13), 3217-3231.

[35] Apte, S.V., Mahesh, K., Lundgren, T., 2003. *A Eulerian-Lagrangian model to simulate two-phase/particulate flows*, Centre for Turbulence Research, Annual Research Briefs 2003.

[36] Kafui, K.D., Thornton, C., Adams, M. J., 2002. *Discrete particle-continuum fluid modelling of gas-solid fluidised beds.* Chemical Engineering Science 57, 2395-2410.

[37] Feng, Y.Q., Xu, B.H., Zhang, S.J., Yu, A.B., Zulli, P., 2004. *Discrete particle simulation of gas fluidization of particle mixtures.* A.I.Ch.E. Journal 50 (8), 1713-1728.

[38] Hoomans, B.P.B., Kuipers, J.A.M., Mohd Salleh, M.A., Stein, M., Seville, J.P.K., 2001. *Experimental validation of granular dynamics simulations of gas-fluidised beds with homogenous in-flow conditions using positron emission particle tracking.* Powder Technology 116 (2-3), 166-177.

[39] Seville, J.P.K., Martin, T.W., Parker, D.J., 1995. *Hopper discharge using positron emission particle tracking.* In: Proceeding of the Third European Symposium on Storage and Flow of Particulate Solids, Nurnberg Messe, Nurnberg, pp. 271-280.

[40] Yuu, S., Kohno, H., Umekage, T., 2001a. *Effect of particle existence on high Reynolds number slit nozzle gas-particle two-phase jet.* JSME International Journal Series B-Fluids and Thermal Engineering 44, 204-212.

[41] Yuu, S., Umekage, T., Kawakami, S., Johno, Y., 2001b. *Computation of air and particle motions in bubbling fluidized bed using distinct element method.* Kagaku Kogaku Ronbunshu 27,560-565.

[42] Yuu, S., Umekage, T., Matsumoto, K., 2005. *Numerical simulation of flow fields in two-dimensional bubbling fluidized bed using smoothed particle hydrodynamics based on stress strain relations obtained by distinct element method calculation and finite difference methods, and experimental verification.* Kagaku Kogaku Ronbunshu 31,92-101.

[43] Ouyang, J., Li, J.H., 2001. *Simulation of dynamic behavior in bubbling fluidization.* Progress in Natural Science 11, 772-778.

[44] Annaland, M.V., Dijkhuizen, W., Deen, N.G., Kuipers, J.A.M., 2006. *Numerical simulation of behavior of gas bubbles using a 3-D front-tracking method.* A.I.Ch.E. Journal 52,99-110.

[45] Zhu, H.P., Zhou, Z.Y., Yang, R.Y., Yu, A.B., 2007. *Discrete particle simulation of particulate systems: A review of major applications and findings.* Chemical Engineering Science 63 (2008), 5728-5770.

[46] Jackson,R. (1963). *The mechanics of fluidized beds.Part I.The stability of the state of uniform fluidization.* Trans. Inst. Chem. Eng. 41, 13- 28.

[47] Murray, J.D., (1965), *On the mathematics of fluidization.* I, J. Fluid Mech. 21, 465-493.

[48] Pigford, R.L., Baron, T., (1965), *Hydrodynamic stability of a fluidized bed,* I&EC Fundamentals 4, pp. 81-87.

[49] Kuipers, J.A.M., Prins, W. and van Swaaij, W.P.M. (1991), *Theoretical and experimental bubble formation at a single orifice in a two-dimensional gas-fluidized bed,* Chem. Eng. Sci., 1991 46, 2881-2894.

[50] Rivard, W.C., Torrey, M.D., (1977), *K-FIX: A Computer Program for Transient, Two- Dimensional, Two-Fluid Flow.* LA-NUREG-6623, NRC-4.

[51] Tsuo, Y. P., Gidaspow, D., (1990), *Computation of Flow Patterns in Circulating Fluidized Beds.* AIChE J. 1990, 36, 885.

[52] Clift, R. (1993), *An Occamist review of fluidized bed modeling,* AIChE Symposium Series, No. 296, 89, 1-17.

[53] Gidaspow, D., 1994. *Multiphase Flow and Fluidization: Continuum and Kinetic Theory Descriptions.* Academic Press, New York.

[54] Nieuwland, J.J., Sint Annaland van, M., Kuipers, J.A.M. and van Swaaij, W.P.M. (1996), *Hydrodynamic modeling of gas-particle flows in riser reactors,* AIChE J., 42, 1569-1582.

[55] Enwald, H., Peirano, E., Almstedt, A.E., and Leckner, B. (1999), *Simulation of the fluid dynamics of a bubbling fluidized bed. Experimental validation of the two-fluid model and evaluation of a parallel multiblock solver,* Chem. Eng. Sci., 54, 311-328.

[56] Glasser, B.J., Kevrekidis, I.G. and Sundaresan, S. (1996), *One- and two-dimensional traveling wave solutions in gas-fluidized beds*, J. Fluid Mech., 306, 183-221.

[57] Bokkers, G.A., 2005. *Multi-level modeling of the hydrodynamics in gas phase polymerisation reactors.* Ph.D. Thesis, University of Twente, Enschede.

[58] Balzer, G., A. Boelle, and O. Simonin, *Eulerian Gas-Solid Flow Modeling of Dense Fluidized Beds*, Electricite de France, Rpt. no. HE-44/95/026/A, 1995.

[59] Syamlal, M. (1998), *Higher order discretization methods for the numerical simulation of fluidized beds*, AIChE Symposium Series, No. 318, 94, 53-57.

[60] van Wachem, B.G.M., Schouten, J.C., Krishna, R. and van den Bleek, C.M. (1998), *Eulerian simulations of bubbling behavior in gas-solid fluidized beds*, Comput. Chem. Eng., 22, s299-s306.

[61] van Wachem, B.G.M., Schouten, J.C., Krishna, R. and van den Bleek, C.M. (1999), *Validation of the Eulerian simulated dynamic behavior of gas-solid fluidized beds*, Chem. Eng. Sci., 54, 2141-2149.

[62] Gerhauser, H., 2003. *CFD applied to the fast pyrolysis of biomass in fluidised beds.* PhD Thesis, Bioenergy Research Group, Aston University.

[63] Junwu Wang, M.A. van der Hoef, J.A.M. Kuipers, *Why the two-fluid model fails to predict the bed expansion characteristics of Geldart A particles in gas-fluidized beds: A tentative answer*, Chemical Engineering Science, 64 3 2009, 622-625

[64] Syamlal, M., OBrien, T.J., 1989. *Computer simulation of bubbles in a fluidized bed.* A.I.Ch.E. Symposium Series 85, 22-31.

[65] Wen, C.-Y., Yu, Y.H., 1966. *Mechanics of fluidization.* Chemical Engineering Progress Symposium Series 62, 100-111.

[66] Taghipour, F., Ellis, N., Wong, C. 2005. *Experimental and computational study of gas-solid fluidized bed hydrodynamics.* Chemical Engineering Science 60 (2005) 6857-6867.

[67] Crowe, C.T., Sommerfeld, M., Tsuji, Y., 1998. *Multiphase Flows with Droplets and Particles.* CRC Press LLC.

[68] D. Gera, M. Gautam, Y. Tsuji, T. Gawaguchi, T. Tanaka, *Computer simulation of bubbles in large-particle fluidized beds*, Powder Technol. 98 (1998) 38-47.

[69] D. Gidaspow, *Hydrodynamics of fluidization and heat transfer: super computer modeling*, Appl. Mech. Rev. 39 (1986) 1-23.

[70] J.A.M. Kuipers, K.J. Van Duin, F.P.H. Van Beckum, W.P.M. Van Swaaij, *A numerical model of gas-fluidized beds*, Chem. Eng. Sci. 47 (1992) 1913-1924.

[71] I. Christie, G.H. Ganser, J.W. Wilder, *Numerical solution of a two dimensional fluidized bed model*, Int. J. Numer. Methods Fluids 28 (1998) 381-394.

[72] Oliver, E. D., Juveland, A. C., Dougherty, J. E., Deinken, H. P., 1966. *Particle-to-Gas Heat Transfer in Fluidized Beds.* Ind. Eng. Chem. Fundamen. , 1966, 5 (3), p 439.

[73] Prins, W. (1987). *Fluidised bed combustion of a single carbon particle.* Ph.D. thesis, Twente, University, The Netherlands.

[74] Parmar, M.S., Hayhurst, A.N., 2002. *The heat transfer coefficient for a freely moving sphere in a bubbling fluidised bed.* Chemical Engineering Science 57, 3485-3494.

[75] Andeen, B. R., Glicksman L. R., 1976. *Heat Transfer to Horizontal Tubes in Shallow Fluidized Beds.* ASMEpaper 76-HT-67.

[76] Yates, J. G. 1983. *Fundamentals of fluidised-bed chemical processes.* London: Butterworths.

[77] Agarwal, P.K., 1991. *Transport phenomena in multi-particle systems-IV. Heat transfer to a large freely moving particle in gas fluidized bed of smaller particles,* Chemical Engineering Science 46, 1115-1127.

[78] Mickley, H. S., D. F. Fairbanks, 1955. *Mechanism of heat transfer to fluidized beds.* American Institute of Chemical Engineers Journal, 1(3), 374, 1955.

[79] Baskakov, A.P., Berg, B.V., Vit, O.K., Filipovsky, N.F., Krakosyan, V.A., Goldobin, J.M., Maskaev, V.K., 1973. *Heat transfer to objects immersed in fluidized beds.* Powder Technology 8, 273-282.

[80] Yoshida, K., Kunii, D., Levenspiel, O. 1969. *Heat transfer mechanisms between wall surface and fluidized bed.* International Journal of Heat Mass Transfer 12, 529-536.

[81] Collier A.P., Hayhurst A.N., Richardson J.L., Scott S.A., 2004. *The heat transfer coefficient between a particle and a bed (packed or fluidised) of much larger particles.* Chemical Engineering Science 59 (2004) 4613-4620.

[82] Scott, A. S., Davidson, F. J., Dennis, S. J., Hayhurst N. A., 2004. *Heat Transfer to a Single Sphere Immersed in Beds of Particles Supplied by Gas at Rates above and below Minimum Fluidization.* Ind. Eng. Chem. Res. 2004, 43, 5632-5644.

[83] Di Natale, F., Lancia, A., Nigro, R., 2008. *A single particle model for surface-to-bed heat transfer in fluidized beds.* Powder Technology 187 (2008) 68-78.

[84] S. Karimipour, R. Zarghami, N. Mostoufi, R. Sotudeh-Gharebagh, *Evaluation of heat transfer coefficient in gassolid fluidized beds using cluster-based approach,* Powder Technol. 172 (1) (2007) 19-26.

[85] Di Natale, F., Lancia, A., Nigro, R., 2007.*Surface-to-bed heat transfer in fluidised beds: Effect of surface shape.* Powder Technology, 174 (3), 2007, 75-81.

[86] Kuipers, J. A. M., Prins, W., Van Swaaij, W. P. M. 1992. *Numerical calculation of wall-to-bed heat-transfer coefficients in gas-fluidized beds.* American Institute of Chemical Engineers Journal, 38, 1079-1091.

[87] Schmidt A., Renz U., 1999. *Eulerian computation of heat transfer in fluidized beds.* Chem. Eng. Sci. 54 (1999) 55155522.

[88] Schmidt A., Renz U., 2000. *Numerical prediction of heat transfer in fluidized beds by a kinetic theory of granular flows.* Int. J. Therm. Sci. (2000) 39, 871-885.

[89] Wang, L., Wu, P., Yang, J., Ni, X., 2007. *Modeling of heat transfer between a high-temperature fluidized bed and an immersed surface by a surface-particle-emulsion model.* Chemical Engineering Science 62 (2007) 503-512.

[90] Wang, L., Wu, P., Yang, J., Ni, X., 2005. *Surface-particle-emulsion model of heat transfer between a fluidized bed and an immersed surface.* Powder Technology 149, 127-138.

[91] J.C. Chen, Max Jakob award lecture, *Surface Contact-Its Significance for Multiphase Heat Transfer: Diverse Examples*, J. Heat Transfer 125 (2003), pp. 549-566.

[92] John C. Chen, John R. Grace, Mohammad R. Golriz, *Heat transfer in fluidized beds: design methods*, Powder Technology, 150 (2), 2005, 123-132.

[93] Di Blasi, C., 1996. *Heat, momentum and mass transport through a shrinking biomass particle exposed to thermal radiation.* Chemical Engineering Science 51, 1121-1132.

[94] Di Blasi, C., 2000. *Modelling the fast pyrolysis of cellulosic particles in fluid-bed reactors.* Chemical Engineering Science 55, 5999-6013.

[95] Di Blasi, C., 1994. *Numerical simulation of cellulose pyrolysis.* Biomass and Bioenergy 7, 87-98.

[96] Di Blasi, C., 1996b. *Kinetic and heat transfer control in the slow and flash pyrolysis of solids.* Industrial and Engineering Chemistry Research 35, 37-46.

[97] Melaaen, M.C., Gronli, M.G., 1997. *Modeling and simulation of moist wood drying and pyrolysis.* In: Bridgwater, A.V., Boocock, D.B.G. (Eds.), Developments in Thermochemical Biomass Conversion. Blackie, London, pp. 132-146.

[98] Saastamoinen, J.J., 1993. *Model for drying and pyrolysis in an updraft gasifier.* In: Bridgwater, A.V. (Ed.), Advances in Thermochemical Biomass Conversion. Blackie, London; pp. 186-200.

[99] Saastamoinen J, Richard J-R. *Simultaneous drying and pyrolysis of solid fuel particles.* Combust Flame 1996;106:288-300.

[100] Saastamoinen JJ, Hamalainen JP, Kilpinen P. *Release of nitrogen compounds from wood particles during pyrolysis.* Environ. Combust. Technol. 2000;1:289-316.

[101] Babu, B.V., Chaurasia, A.S., 2002a. *Modeling and simulation of pyrolysis: influence of particle size and temperature.* Proceedings of International Conference on Multimedia and Design, Vol. 4, Mumbai, India, pp. 103-128.

[102] Babu, B.V., Chaurasia, A.S., 2002b. *Modeling and simulation of pyrolysis: effect of convective heat transfer and orders of reactions.* Proceedings of International Symposium and 55th Annual Session of IIChE (CHEMCON-2002), OU, Hyderabad, India, pp. 105-106.

[103] Babu, B.V., Chaurasia, A.S., 2003a. *Modeling for pyrolysis of solid particle: kinetics and heat transfer effects.* Energy Conversion and Management 44, 2251-2275.

[104] Babu, B.V., Chaurasia, A.S., 2003b. *Modeling, simulation, and estimation of optimum parameters in pyrolysis of biomass.* Energy Conversion and Management 44, 2135-2158.

[105] Babu, B.V., Chaurasia, A.S., 2003c. *Modeling and simulation of pyrolysis of biomass: effect of heat of reaction.* Proceedings of International Symposium on Process Systems Engineering and Control (ISPSEC 03)for Productivity Enhancement Through Design andOptimization, IIT-Bombay, Mumbai, India, pp. 181-186.

[106] Babu, B.V., Chaurasia, A.S., 2004c. *Pyrolysis of biomass: improved models for simultaneous kinetics and transport of heat, mass, and momentum.* Energy Conversion and Management 45, 1297-1327.

[107] Liang, X.H., Kozinski, J.A., *Numerical modeling of combustion and pyrolysis of cellulosic biomass in thermogravimetric systems.* Fuel, 79 12, 2000, 1477-1486.

[108] A. M. C. Janse, R. W. J. Westerhout, W. Prins, *Modelling of flash pyrolysis of a single wood particle*, Chemical Engineering and Processing, 39 3, 2000, 239-252.

[109] Peters, B., Bruch, C., *Drying and pyrolysis of wood particles: experiments and simulation.* Journal of Analytical and Applied Pyrolysis, 70 2, 2003, 233-250.

[110] J. Larfeldt, B. Leckner, M. C. Melaaen, *Modelling and measurements of the pyrolysis of large wood particles.* Fuel, 79 13, 2000, 1637-1643.

[111] Bryden, K.M., Ragland, K.W., Rutland C.J., *Modeling thermally thick pyrolysis of wood.* Biomass and Bioenergy, 22 1, 2002, 41-53.

[112] Saastamoinen, J.J., 2006. *Simplified model for calculation of devolatilization in fluidized beds.* Fuel 85 (2006) 2388-2395.

[113] Rostami AA, Hajaligol MR, Wrenn SE. *A biomass pyrolysis submodel for CFD applications.* Fuel 2004;83:1519-23.

[114] Chen Y, Charpenay S, Jensen A, Wojtowicz MA, Serio MA. *Modeling of biomass pyrolysis kinetics.* Proc Combust Inst 1998; 27:1327-34.

[115] Niksa S, Fifth International Conference on Technologies and Combustion for Clean Environment, Lisbon, Portugal, vol. II.; 1999. p. 709-15.

[116] Di Blasi, C., *Modeling chemical and physical processes of wood and biomass pyrolysis.* Progress in Energy and Combustion Science, 34 1, 2008, 47-90.

[117] M.J. Antal and G. Varhegyi, *Cellulose pyrolysis kinetics: the current state of knowledge*, Ind Eng Chem Res 34 (1995), pp. 703-717.

[118] D.L. Pyle and C.A. Zaror, *Heat transfer and kinetics in the low temperature pyrolysis of solids*, Chem Eng Sci 19 (1984), pp. 147-158.

[119] F. Shafizadeh, *Pyrolytic reactions and products of biomass.* In: R.P. Overend, T.A. Milne and L.K. Mudge, Editors, Fundamentals of biomass thermochemical conversion, Elsevier, London (1985), pp. 183-217.

[120] S.M. Ward and J. Braslaw, *Experimental weight loss kinetics of wood pyrolysis under vacuum*, Combust Flame 61 (1985), pp. 261-269.

[121] C.A. Koufopanos, G. Maschio and A. Lucchesi, *Kinetic modeling of the pyrolysis of biomass and biomass components*, Can J Chem Eng 67 (1989), pp. 75-84.

[122] P.T. Williams and S. Besler, *The pyrolysis of rice husks in a thermogravimetric analyzer and static batch reactor*, Fuel 72 (1993), pp. 151-159.

[123] J.A. Caballero, R. Font and A. Marcilla, *Comparative study of the pyrolysis of almond shells and their fractions, holocellulose and lignin. Product yields and kinetics*, Thermochim Acta 276 (1996), pp. 57-77.

[124] R.J. Evans and T.A. Milne, *Molecular characterization of the pyrolysis of biomass.* 1, Fundamentals. Energy Fuels 1 (1987), pp. 123-137.

[125] M.J. Antal, *Effects of reactor severity on the gas-phase pyrolysis of cellulose- and kraft lignin-derived volatile matter*, Ind Eng Prod Res Dev 22 (1983), pp. 366-375.

[126] M.J. Antal, *A review of the vapor phase pyrolysis of biomass derived volatile matter.* In: R.P. Overend, T.A. Milne and L.K. Mudge, Editors, Fundamentals of biomass thermochemical conversion, Elsevier, London (1985), pp. 511-537.

[127] Di Blasi, C., 1993a. *Analysis of convection and secondary reaction effect effects within porous solid fuels undergoing pyrolysis.* Combustion Science Technology 90, 315-339.

[128] Moghtaderi, B., *The state-of-the-art in pyrolysis modelling of lignocellulosic solid fuels,* Fire and Materials, 2006; 30:1-34.

[129] Kung H.C., *A mathematical model of wood pyrolysis.* Combustion and Flames 1972; 18:185-195.

[130] Kansa E., Perlee H., Chaiken R., *Mathematical model of wood pyrolysis including internal forced convection.* Combustion and Flames 1977; 29: 311-324.

[131] White R.H., Schaffer E.L., *Application of CMA program to wood charring.* Fire Technology 1978; 14(4): 279-290.

[132] Miller C.A., Ramohalli K.N.R., *A theoretical heterogeneous model of wood pyrolysis.* Combustion Science and Technology 1986, 46, 249-265.

[133] Sibulkin M., *Heat of gasification for pyrolysis of charring materials.* Fire Safety Science Proceedings of the 1st International Symposium. IAFSS: MA, USA, 1986; 391-400.

[134] Peters B., Bruch C., *A Flexible and stable numerical method for simulating the thermal decomposition of wood particles.* Chemosphere 2001; 42:481-490.

[135] Hastaoglu M.A., Hassam M.S., *Application of a general gas-solid reaction model to flash pyrolysis of wood in a circulating fluidized bed.* Fuel 1995; 74(5):697-703.

[136] Wojtowicz M.A., Bassilakis R., Smith W.W., Chen Y., Carangelo R.M., *Modeling the evolution of volatile species during tobacco pyrolysis.* Journal of Analytical and Applied Pyrolysis 2003; 66: 235-261.

[137] Jones J.M., Pourkashanian M., Williams A., Hainsworth D., *A comprehensive biomass combustion model.* Renewable Energy 2000; 19: 229-234.

[138] Di Blasi, C., 1998. *Comparison of semi-global mechanisms for primary pyrolysis of lignocellulosic fuels.* Journal of Analytical and Applied Pyrolysis 47, 43-64.

[139] Hagge M., Bryden K.M., *Modeling the impact of shrinkage on the pyrolysis of dry biomass.* Chemical Engineering Science 2002; 57: 2811-2823.

[140] A.G.W. Bradbury, Y. Sakai and F. Shafizadeh, *Kinetic model for prolysis of celulose*, J. Appl. Polym. Sci. 23 (1979), pp. 3271-3280.

[141] F. Shafizadeh and P.P.S. Chin, *Thermal deterioration of wood*, ACS Symp Ser 43 (1977), pp. 57-81.

[142] Koufopanos, C.A., Papayannakos, N., Maschio, G. and Lucchesi, A., 1991. *Modelling of the pyrolysis of biomass particles. Studies on kinetics, thermal and heat transfer effects.* The Canadian Journal of Chemical Engineering 69, pp. 907-915.

[143] Ergun S. (1952), *Fluid Flow through packed columns.* Chem. Eng. Prog., Volume 48, p. 89-94.

[144] Gibilaro L. G., 2001. *Fluidization Dynamics. The formulation and applications of a predictive theory for the fluidized state*, Butterworth-Heinemann.

[145] Rhodes, M., 1998. *Introduction to Particle Technology*, Wiley.

[146] J. Werther and O. Molerus, *The local structure of gas fluidized beds: I A statistically based measuring system*, International Journal of Multiphase Flow 1 (1973), pp. 103-122.

[147] J. Werther, *Bubbles in gas fluidized beds-Part I*, Transactions of the Institutions of Chemical Engineers 52 (1974), pp. 149-159.

[148] R. Toomey and H.P. Johnstone, *Gaseous fluidization of solid particles*, Chemical Engineering Progress 48 (1952), pp. 220-226.

[149] K. Hilligardt and J. Werther, *Local bubble gas hold-up and expansion of gas/solid fluidized beds*, German Chemical Engineering 9 (1986), pp. 215-221.

[150] K.S. Lim, V.S. Gururajan and P.K. Agrawal, *Mixing of homogeneous solid in bubbling fluidized beds: theoretical modeling and experimental investigation using digital image analysis*, Chemical Engineering Science 48 (1993), pp. 2251-2265.

[151] Aris, R., *Vectors, Tensors and the Basic Equations of Fluid Mechanics.* Dover Publ. Inc., New York, 1962.

[152] Stokes, G.G., *On the Theories of Internal Friction of Fluids in Motion.* Trans. Cambridge Phil. SOC., 8 (1845), pp. 287-305.

[153] Blazek, J., *Computational Fluid Dynamics: Principles and Applications.* ELSEVIER SCIENCE Ltd, 2001.

[154] Drew, D.A., Passman S.L, *Theory of multicomponent fluids.* Springer-Verlag, New York Inc., 1999.

[155] Albraten, P. (1982) *The dynamics of two phase flow.* Ph.D. thesis, Department of Energy Conversion, Chalmers University of Technology, Sweden.

[156] Andersson, S. (1991) *Dimensionless groups in the momentum equation of a bubbling fluidized bed.* Chalmers University of Technology, Sweden, Report A 91-188.

[157] Syamlal, M., Rogers, W. and O'Brien, T. J. (1993), *MFIX documentation, Theory Guide,* Technical Note DOE/METC-94/1004.

[158] Richarson, J. F. and Zaki, W. N. (1954) *Sedimentation and fluidisation: Part I.* Trans. Instn Chem. Engrs 32, 35-52.

[159] Dalla Valle, J. M. (1948), *Micromeritics.* Pitman, London.

[160] Garside, J. and A1-Dibouni, M. R. (1977), *Velocity-voidage relationship for fluidization and sedimentation.* I&EC Proc. Des. Dev., 16, 206-214.

[161] Ding, J. and Gidaspow, D. (1990), *A bubbling fluidization model using kinetic theory of granular flow.* AIChE Journal 36, 523-538.

[162] Lun, C. K. K., Savage, F. B., Jeffrey, D. J. and Chepurniy, N. (1984) Kinetic theories for granular flow: inelastic particles in couette flow and slightly inelastic particles in a general flowfield. J. Fluid Mech. 140, 223-256.

[163] Gidaspow, D., Bezburuah, R. and Ding, J. (1992), *Hydrodynamics of circulating fluidized beds; kinetic theory approach.* Fluidization VII, Proceedings of the 7th Engineering Foundation Conference on Fluidization, pp. 75-82.

[164] Gidaspow, D., Tsuo, Y. P. and Luo, K. M. (1989), *Computed and experimental cluster formation and velocity profiles in circulating ftuidized beds.* Fluidization VI, Proceedings of the 6th Engineering Foundation Conference on Fluidization.

[165] Chapman, S. and Cowling, T. G. (1970), *The Mathematical Theory of Non-uniform Gases*, 3rd edn. Cambridge University Press, Cambridge.

[166] Ogawa, S., Umemura, A. and Oshina, N. (1980), *On the equations of fully fluidized granular materials*, J. Angew. Math. Phys., 31, 483.

[167] Carnahan, N. F. and Starling, K. E. (1969), *Equations of state for non-attracting rigid spheres.* J. Chem. Phys. 51, 635-636.

[168] Lun, C. K. K. and Savage, F. B. (1986), *The effects of impact velocity dependant coefficient of restitution on stress developed by sheared granular materials.* Acta Mechanica 63, 15-44.

[169] Balzer, G. and Simonin, O. (1993), *Extension of Eulerian gas-solid flow modelling to dense fluidized bed.* Proc. 5th Int. Symp. on Refined Flow Modelling and Turbulence Measurements, ed. P. L. Viollet, pp. 417-424.

[170] Boemer, A., Qi, H., Renz, U., Vasquez, S. and Boysan, F. (1995), *Eulerian computation of fluidized bed hydrodynamics–a comparison of physical models.* Proceedings of the 13th Int. Con[. on FBC, Orlando, pp. 775-786.

[171] Boemer, A., Qi, H., Renz, U. (1997). *Eulerian simulation of bubble formation at a jet in a two-dimensional fluidized beds.* International Journal of Multiphase Flow, 23(5), 927-944.

[172] Schiller, L., Naumann, A., 1933. *Uber die grundlegenden Berechungen bei der Schwerkraftaufbereitung.* Ver. Deut. Ing., 77, 318.

[173] Clift, R. Gauvin, W.H.,1970. *The motion of particles in turbulent gas streams.* Proc. Chemeca '70, 1, 14.

[174] Clift, R., Weber, M.E., Grace, J.R., 1978. *Bubbles, Drops, and Particles.* Academic Press, New York.

[175] Bird, R.B., Stewart, W.E., Lightfoot, E.N., 2002. *Transport Phenomena.*second ed. Wiley, New York.

[176] Morsi, S.A., Alexander, A.J., 1972. *An investigation of particle trajectories in two-phase flow systems.* Journal of Fluid Mechanics 55, 193-208.

[177] R. Turton and O. Levenspiel, *A short note on the drag correlation for spheres,* Powder Technology 47 (1) (Jun 1986), pp. 83-86.

[178] Putnam, A., 1961.*Integrable form of droplet drag coefficient.* ARS JNl., 31, 1467.

[179] M.W. Reeks and S. McKee, *The dispersive effects of Basset history forces on particle motion in a turbulent flow*, Physics of Fluids 27 (1984), p. 1573.

[180] P.G. Saffman, *The lift on a small sphere in a slow shear flow*, Journal of Fluid Mechanics 22 (1965), pp. 385-400.

[181] Mei, R., *An approximate expression for the shear lift. force on a particle at a finite Reynolds number*, Int. J. Multiphase Flow, 18 (1992) 145-147.

[182] S. I. Rubinow and Joseph B. Keller, *The transverse force on a spinning sphere moving in a viscous fluid.* Journal of Fluid Mechanics (1961), 11 (3), 447-459.

[183] P.S. Epstein , *Zur Theorie des Radiometers.* Zcitschrift fuer Physik 537-563 (1929).

[184] Bahary, M., 1994. *Experimental and computational studies of hydrodynamics in three-phase and two-phase fluidised beds.* Ph.D. Thesis, Illinois Institute of Technology, Chicago.

[185] Grevskott, S., Sannæs, B.H., Dudukovic, M.P., Hjarbo, K.W., Svendsen, H.F., 1996. *Liquid circulation, bubble size distributions, and solids movementin two-and three-phase bubble columns.* Chemical Engineering Science 51, 1703-1713.

[186] Mitra-Majumdar, D., Farouk, B., Shah, Y.T., 1997. *Hydrodynamic modeling of three-phase flows through a vertical column.* Chemical Engineering Science 52, 4485-4497.

[187] Jianping, W., Shonglin, X., 1998. *Local hydrodynamics in a gas-liquid-solid three- phase bubble column reactor.* Chemical Engineering Journal 70, 81-84.

[188] Padial, N.T., Vander Heyden, W.B., Rauenzahn, R.M., Yarbro, S.L., 2000. *Three- dimensional simulation of a three-phase draft-tube bubble column.* Chemical Engineering Science 55, 3261-3273.

[189] Matonis, D., Gidaspow, D., Bahary, M., 2002. *CFD simulation of flow and turbulence in a slurry bubble column.* A.I.Ch.E. Journal 48, 1413-1429.

[190] Schallenberg, J., Enß, J.H., Hempel, D.C., 2005. *The important role of local dispersed phase hold-ups for the calculation of three-phase bubble columns.* Chemical Engineering Science 60, 6027-6033.

[191] Y. Li, J. Zhang and L.-S. Fan, *Numerical simulation of gas-liquid-solid fluidization systems using a combined CFD-VOF-DPM method: bubble wake behavior*, Chemical Engineering Science 54 (1999), pp. 5101-5107.

[192] X. Zhang and G. Ahmadi, *EulerianLagrangian simulations of liquid-gas-solid flows in three-phase slurry reactors*, Chemical Engineering Science 60 (2005), pp.] 50895104.

[193] Bourloutski, E., Sommerfeld, M., 2004. *Euler/Lagrange calculations of gas-liquid-solid flows in bubble columns with phase intaraction.* In: Bubbly flows: Analysis, Modelling and calculation, Springer 2004.

[194] Kolev, N.I., 2005. *Multiphase Flow Dynamics 2, Thermal and Mechanical Interactions.* 2nd edition, Springer.

[195] Ranz, W.E., Marshall, W.R., 1952a. *Evaporation from drops, Part I.* Chemical Engineering Progress 48, 141146.

[196] Ranz,W.E., Marshall,W.R., 1952b. *Evaporation from drops, Part II.* Chemical Engineering Progress 48, 173180.

[197] Gunn D.J. (1978), *Transfer of heat or mass to particles in fixed and fluidised beds.* Int. J. Heat and Mass Transfer, Volume 21, p. 467.

[198] Gelperin, N. I., Einstein, V. G., (1971). In J. F. Davidson, & D. Harrison, *Heat transfer in fluidized beds*, fluidization. London: Academic Press.

[199] Cybulski, A., van Dalen, M. J., Verkerk, J. W., & van den Berg, P. J. (1975). *Gas-particle heat transfer coeffcients in packed beds at low Reynolds numbers.* Chemical Engineering Science, 30, 1015-1018.

[200] Pfeffer, R. (1964). *Heat and mass transport in multiparticle systems.* Industrial and Engineering Chemistry Fundamentals, 3, 33.

[201] Nelson, P. A., Galloway, T. R. (1975). *Particle-to-fluid heat and mass transfer in dense systems of fine particles.* Chemical Engineering Science, 30, 1-6.

[202] Chan, W.R., Kelbon, M., Krieger, B.B., 1985. *Modelling and experimental verification of physical and chemical processes during pyrolysis of large biomass particle.* Fuel 64, 1505-1513.

[203] Liden, A.G., Berruti, F., Scott, D.S., 1988. *A kinetic model for the production of liquids from the flash pyrolysis of biomass.* Chemical Engineering Communications 65, 207-221.

[204] Ferziger H. J., Milovan P., *Computational Methods for Fluid Dynamics,* Springer-Verlag, 2002.

[205] Anderson D., J., *Computational Fluid Dynamics: The Basics with Applications.* McGraw-Hill, 1995.

[206] Versteeg, K., H., Malalasekera, W., *An Introduction to Computational Fluid Dynamics: The Finite Volume Method.* Pearson Education, 2007.

[207] Chung, J., T., *Computational Fluid Dynamics.* Cambridge University Press, 2002.

[208] Bridgwater, A.V., 1999. *Principles and practice of biomass fast pyrolysis processes for liquids.* Journal of Analytical and Applied Pyrolysis 51, 3-22.

[209] Basu, P., 2006. *Combustion and gasification in fluidized beds.* Taylor and Francis Group, LLC.